Title	Design of Organic-inorganic Nanohybrid Photocatalysts using Visible-light Responsive Metal Complexes
Author(s)	河嶋, 将慈
Citation	大阪大学, 2014, 博士論文
Version Type	VoR
URL	https://doi.org/10.18910/50509
rights	
Note	

博士学位論文

Design of Organic-inorganic Nanohybrid Photocatalysts using Visible-light Responsive Metal Complexes
可視光応答性金属錯体を利用した有機‐無機ナノハイブリッド光触媒の創製

河嶋 将慈

２０１４年６月

大阪大学大学院工学研究科
マテリアル生産科学専攻

Contents

Chapter I

General Introduction

1.1 Background

1.1.1 Energy Problems

Recently, the problems of energy supply are quite severe on a global scale. Energy sources keeping our life depend on fossil fuel, but sooner or later we expect drying up its resources. Keeping the use of fossil fuel will accelerate the progressions of global warming, sea level rise, acid rain, desertification, waste problem, and particulate matter 2.5 [1, 2]. We aspire to utilize renewable forms of energy, e.g., solar, water, wind and geothermal energy. In these low-impact energies, solar energy is especially affected on the properties of no generation of greenhouse effect gas, permanently usable resource, and available power anywhere at all over the world. Photocatalyst is attracted on the method of using solar energy and investigated to high quality applied to various fields eagerly.

1.1.2 Development of Titanium Dioxide Photocatalysts

Titanium dioxide (TiO_2) has been commercially used as photocatalyst since Honda and Fujishima et al. discovered water degradation to hydrogen and oxygen irradiating light to TiO_2 in 1972 [3]. TiO_2 photocatalyst possesses the abilities of pollutant degradation, water clarification, antibacterial, antifouling and hydrophilicity. By these photocatalytic properties, TiO_2 is applied to outer wall of buildings, inner packaging of rooms, coating on glasses, air purification system, and clothing. These performances can be represented to the other function with nanosized technology. The metal oxides of the tetrahedral coordination (titanium, vanadium, chromium, and molybdenum oxides) moieties can be injected and isolated in the silica based matrixes of microporous zeolite and mesoporous silica materials, and named as ‘single-site photocatalysts’ [4, 5]. The ability of single-site photocatalyst is different from bulk metal one in the valence of the exited state and the absorption peak to blue shift. Then, rare metal nanoparticles are usually immobilized on the mononuclear metal by the method of photo-assisted deposition [6] and microwave irradiation [7]. The aim of the single-site photocatalyst results in high dispersion at the atomic level, which lead to a protection an agglomeration of thermal action and low cost as a decrease of rare metal amount. Additionally TiO_2 thin films exhibit photoinduced superhydrophilicity which is defined that contact angle is lower than 5 degree irradiating ultra violet (UV) light. Ti-containing mesoporous silica thin films (Ti-MSTFs) with photoinduced superhydrophilicity have been successfully prepared on quartz substrates [8, 9]. TiO_2 photocatalysts have widely been used for organic reactions however UV region with high energy is necessary for activating the electrons of TiO_2 [10]. Because UV region is involved only 5% in solar light, other regions can be performed no beneficial use. The effective use of visible light is an important task thinking energy efficiency. Then metal complexes are attracted to absorption of wide wavelength involved in visible region. Moreover, metal complex catalysts enable selective organic transformations or oxidations owing to the proper redox activity. On the other hand, TiO_2-based photocatalysts decompose volatile organic compound (VOC) completely by strong redox ability. This ability of partial oxidation in metal complex widely contributes to a chemical synthesis of reactive intermediate in the industrial process.

1.2 Novel Metal Complex Photocatalysts

The performances of metal complexes responded to visible light are attracted a remarkable attention to the resolution of the exited state. The exited state is decided by the major factor about the energy, e.g., an electron distribution, an orbital phase, a spin multiplicity and lifetime. Molecular consists of highest occupied molecular orbital (HOMO) and lowest unoccupied molecular orbital (LUMO). Then many kinds of exited states with different energy and electronic distribution are caused by rising up electrons from HOMO to LUMO. The design of ligand enables to control the wavelength of absorption and results in the use of visible region widely. Absorption of visible light leads to a metal-to-ligand charge-transfer transition (^{1}MLCT), which corresponds to exited singlet state, and quickly this exited state is dropped to lowest singlet state by internal transduction accompanied with molecular vibration. Then this exited state is transferred with unit efficiency to a lowest triplet MLCT state (^{3}MLCT) by intersystem crossing [11]. The energy gap between the lowest singlet MLCT state and the exited triplet MLCT state is negligible with heavier metal complex. The exited electron is emitted by three modes of photoluminescence, i.e., fluorescence transferring from ^{1}MLCT state to ground state, phosphorescence dropping from ^{3}MLCT state to ground state, and no radiation transition without luminescence. ^{3}MLCT state usually has a long lifetime ($\tau \approx 10^{-6} \sim 10^{-1}$ s) due to forbidden transition and can be used for photosensitized function. In the absence of O_2, the lowest ^{3}MLCT exhibits a phosphorescence emission, whereas potentially active oxygen species such as singlet oxygen ($^1O_2$) and superoxide anion (O_2^{*-}) are generated by energy and/or electron transfer reactions from the lowest ^{3}MLCT to O_2. An oxidative reaction is carried out by these active oxygen species, and thus the efficiency of catalytic reaction can be often measured by quantum yield using the method of chemical actinometer.

Tris(2,2'-bipyridine)ruthenium(II) ($Ru(bpy)_3^{2+}$) complex represents an important class of compounds that possess a rich range of photophysical and spectroscopic properties [12]. Much of this behavior originates from the potential capacity of the complex as a photosensitizer in the conversion of solar to other beneficial forms of energy. The ground-state electronic configuration of $Ru(bpy)_3^{2+}$ is a singlet state with the six valence electrons in the t_2g (πM) orbitals. Thanks to the enhanced spin-orbit coupling induced by ruthenium complex, the conversion from ^{1}MLCT to ^{3}MLCT is rapid, $\tau \approx 100$ fs [13]. Much work has focused on investigating the nature of these states by spectroscopic examination of crystals, influence of solvents, and the choice of the ligands and/or substituents [12, 14].

Bis-(2-phenylpyridine)-(2,2'-bipyridine)iridium (III) ($[Ir(ppy)_2(bpy)]^+$) complex has been extensively studied for application in electrophosphorescent organic light-emitting diodes [15]; therefore, we postulate that Ir(III) complexes might be a photosensitizer that could successfully promote electron transfer from ^{3}MLCT state to water reduction catalysts. These complexes have high luminescence quantum yields (~1) originating from their high ligand field splitting [16]. The affinity with the water reduction catalyst is an important element to take advantage of the strong phosphorescence emission effectively. Tris(2,2'-bipyridine)rhodium(III) ($[Rh(bpy)_3]^{3+}$) is an ideal catalyst for proton reduction because it keeps two electrons at a suitable potential for H_2 production known to form hydrides [17]. The combination of Ir and Rh complexes could enable visible-light-driven H_2 production without an electron relay [18-20].

The system without an electron relay is available to bridge ligands that can link the components in an appropriate structure. Ruthenium(II) polypyridine complexes, which show favorable physical properties such as long exited-state lifetimes and high luminescent efficiencies, are often contained as photosensitized site. The lowest ^{3}MLCT exhibits a phosphorescence emission [14], while energy and/or electron transfer reactions to the adjacent accepters occur [21]. The multinuclear complexes are expected to facilitate energy and/or electron transfer from the sensitizer dye to the accepter as catalytic site. These multinuclear complex systems are tried to aspire for high efficiency in the photoinduced reactions, e.g., Ru-Pd and Ru-Pt binuclear complex [20, 21].

The other metal complexes also show physicochemical properties with the unexpected behavior responded to the surrounding environment. Tris(2,2'-bipyridine)iron(II) ($Fe(bpy)_3^{2+}$) complex is a respondent molecular to visible light and we examined the physicochemical properties of $Fe(bpy)_3^{2+}$ complexes included within the cavities of zeolite Y. Then $Fe(bpy)_3^{2+}$ encapsulated in zeolite Y catalyst enable to photo-assisted oxidation of styrene derivatives using O_2, while a homogeneous complex ($Fe(bpy)_3(ClO_4)_2$) was inactive under identical reaction conditions [23, 24].

Bis(diethylethylenediamine)copper(II) ($[Cu(dieten)_2](ClO_4)_2$) complex is one of the thermochromic molecule whose properties were reported in 1938 [25]. The low temperature phase consists of the planar ligand which color is red violet, while the high temperature phase is changed to the distorted structure slightly and dark purple. We reported that these thermochromic complexes immobilized on mesoporous silica represent the analogous structure to high temperature phase by restricted space even in the condition of mild temperature. This heterogeneous catalyst acted selective transformation of benzene to phenol in spite of no reactivity in homogeneous media [26].

Photochromic compounds have also attracted remarkable attention because of their potential for optical memory media and switching devices [27]. 1,2-bis(2-methyl-5-(4-pyridyl)-3-thienyl)-perfluorocyclopentene copper(II) is photochromic complex performing the conversion from the open-ring to the closed-ring isomers under UV light irradiation and the structural change under visible light reversibly [28].

Luminescent square-planar d8 Pt(II) complexes have received attention recently [29]. The photoluminescence from such Pt(II) complexes originates from some of the lowest triplet-excited states, including MLCT and metal-metal-to-ligand charge-transfer (MMLCT) excited states with short Pt-Pt separation (<3.5 Å) [30]. We have developed a number of new inorganic-organic hybrid photocatalysts by anchoring a chloro(2,2’:6’,2”-terpyridine)platinum(II) ($[Pt(tpy)Cl]^+$) complex to various mesoporous silica hosts. We reported that these Pt complex catalysts enable a selective photooxidation reaction with O_2 and H_2 production in aqueous media [31-35].

1.3 Micro Porous and Layered Materials

In the industrial chemical process, metal complex catalysts are frequently used in homogeneous field, however separating metal complexes from reactants and recycling catalysts repeatedly are quite difficult. As one of the method resolving the problem, an attempt which nanosized metal catalysts are immobilized on organic or inorganic supports is investigated hardly [36-41]. These heterogeneous catalysts on the metal oxide supports, e.g., titanium dioxide [42, 43] and alumina [44], enable to isolate and use repeatable keeping the original catalytic activity. The design of nano-controll catalysts with nanoparticles introducing into micro-meso porous material is also attracted an attention [45]. Various functional porous materials, for example, mesoporous silica [7-9, 31-33, 46-49], ion-exchanged resin [18, 50, 51], zeolite [14, 23, 24, 52, 53], layered niobate [19, 34, 54] and zirconium phosphate [20, 55] are researched to expect the effect of supports. These supports show the unique effect around the environment, i.e., large surface area, base-acid properties, adsorption, hydrophilic-hydrophobic properties, electrostatic fields and steric effects. Especially the porous materials with large surface area contribute to high dispersion, size control and protecting aggregation about metal nanoparticles, which result in improvement to high catalytic performances. Many researchers have reported these particular properties originating from porous matrices, and presented the novel behaviors affected from micro environment against the performances seen in the free metal catalyst [14, 23, 26, 36, 46-53, 56, 57].

Zeolites are attractive materials for encapsulation of metals, semiconductors, and organic and organometallic complexes [58-60]. Zeolite supercages are sources of various functions exemplified to molecular sieve depended on the pore size [61]. Both steric and electrostatic constraints can influence the structure and reactivity of the encapsulated species. These active species frequently result in lifetime enhancement of short-lived reaction intermediates, triplet states, free radicals, and carbocations. Zeolite is a kind of complex oxide constructed with silica and alumina, and therefore it is compensated charge by the aid of protons and/or alkali metal cations. Changing to heavier alkali metal cations in the supercage leads to the weaker fluorescence and the stronger phosphorescence, so called "heavy metal effect" [62, 63]. The materials based on zeolite are also important as industrial catalysts; this is exemplified by platinum clusters on zeolite LTL for naphtha dehydrocyclization and tetrahedrally coordinated titanium-oxide moieties implanted within microporous zeolites used for several oxidation process.

Among various inorganic host materials, zirconium phosphate ($Zr(HPO_4)_2 \cdot H_2O$, α-ZrP) has attracted many attentions because of its ability to serve as ion-exchanger, solid-state ion conductors, and catalysts [64, 65]. α-ZrP has a layered structure, in which zirconium atoms are bridged by phosphate groups and phosphate oxygens except bonded to each zirconium atom is linked to an exchangeable hydrogen atom. The distance between the layers in α-ZrP is 7.6 Å. The expanse of the layer distance by the use of presswelled α-ZrP succeeded in the intercalation of large molecules compared to interlayer of traditional α-ZrP. The expanded α-ZrP have been utilized as a host for luminescent complexes, such as $[Ir(ppy)_2(bpy)]^+$ [20], $[Ru(bpy)_3]^{2+}$ [66], $[Pt(tpy)Cl]^+$ [67], and $Re(phen)(CO)_3Cl$ [68], which have been reported for their unique physicochemical properties within the macroheterogeneous environments of α-ZrP.

The inorganic-organic hybrid materials often exhibit unanticipated physicochemical properties because of steric and electrostatic constraints within the confined interlayer spaces. Then, layered potassium niobate ($K_4Nb_6O_{17}$) possesses a unique layered structure with two different alternately stacked interlayers I and II [69]. The charge of the anionic sheet formed by octahedral NbO_6 units via bridging oxygen atoms for two dimensions is balanced by K^+ between the layers. Interlayers I enable to exchange K^+ ion to cation species, on the other hand interlayers II cannot enable to exchange cation but hydrate themselves in aqueous media [54, 70]. $K_4Nb_6O_{17}$ has a photoactive nature and an electrical conductivity; thus it is expected to facilitate photochemical reaction due to the properties of electron transfer through the host. Thus, it can be desired that intercalation of metal complexes in $K_4Nb_6O_{17}$ may have novel photofunctions because of electronic and energetic host-guest interactions. To date, synthesis of hybrid materials of layered $K_4Nb_6O_{17}$ with MV^{2+} [71], porphyrin [72], $[Pt(tpy)Cl]^+$ [34], and $[Ru(bpy)_3]Cl_2$ [73] have been successful, and these materials show interesting photochemical properties.

1.4 Photoinduced Catalytic Reactions under Visible Light Irradiation

Selective oxidation in liquid phase is an important process for controlling synthesis of organic intermediate. Semiconductor photocatalysts exemplified by TiO_2 decompose organic compound to CO_2 and H_2O perfectly [9, 10, 49, 53, 74], however organic dye and metal complex can oxidize chemical compound in the liquid phase partially [14, 16, 24, 26, 31]. Selective oxidation of hydrocarbons using molecular oxygen is interested in respect to both fundamental understanding of the process and potential practical utilization [75]. Selective oxidation using metal complex in the liquid phase is usually low activity and selectivity because of weaker oxidation capacity than bulk and nanoparticle catalyst. Thus, the research is continued for novel heterogeneous photocatalysts capable of oxidizing hydrocarbons with high selectivity as well as absorbing in the visible region.

Suzuki-Miyaura coupling reaction has been recently attracted remarkable attention since Suzuki and Negishi won the Nobel Prize in 2010. Suzuki-Miyaura cross-coupling reaction between aryl halide and aryl boronic acid performs to form new C-C bonds [76]. Many kinds of C-C cross coupling exemplified by Negishi, Mizorogi-Heck, Kumada-Tamao, Stille, and Sonogashira coupling have been investigated eagerly. For these coupling reactions usually using Pd complexes, catalytic cycles repeatedly revolve through three steps, i.e., oxidative addition, transmetalation, and reductive elimination [77]. The oxidative addition step, which aryl halide adds into Pd(0) complex in, is the rate determining step of the catalytic cycle in the most cases. Oxidative addition should be improved to realize high activity, and thus forming electron rich Pd species is effective with the efforts to the design of sterically-bulky ligand field [78, 79], the addition of phosphine as electron donor, and the assist of photo-chemical energy. Especially $Ru(bpy)_3^{2+}$ complex derivatives as photosensitizer are commonly utilized for electron and/or energy transfer to Pd catalytic site [22, 80, 81].

Hydrogen is one of the clean energies desired to assume an important roll in next generation because the byproduct of combustive reaction with oxygen is only water [82]. Very efficient energy conversion can be realized by combining with proton exchange membrane fuel cell (PEMFC) technology [83]. Since Honda and Fujishima discovered the photocatalytic activity of TiO_2 in 1972 [3], many branches of catalyst systems based on semiconducting metal oxides have been explored for water splitting into H_2 and O_2 [18-20, 32-34, 43, 56, 84-86]. On the other hand, the molecular based photocatalytic systems on water splitting generally involve multiple components including a photosensitizer, an electron relay, a water reduction catalyst, and sacrificial reagents [87-89]. For the realization for this system, a number of challenges about low conversion efficiency, use of harmful MV^{2+} as the electron relay, and the lack of chemical stabilization must be overcome. The widespread application of hydrogen as a transportation fuel is limited as the problems of flammable gas and delivery efficiency. Thus formic acid (HCOOH), which is a liquid at room temperature and contains 4.4 wt% hydrogen, is one of the major products formed during biomass processing and convenient hydrogen carrier for fuel cells [51, 90]. Ammonia borane (H_3NBH_3) is also desired to the clean material of hydrogen storage because photoenergy is converted into useful chemical energy for the decomposition of harmful chemical wastes [91-93].

1.5 Mechanism and Application of Localized Surface Plasmon Resonance

The phenomenon of localized surface plasmon resonance (LSPR) induced by Au, Ag and Cu nanoparticles (NPs) has attracted great potential from its considerable attention for developing sensors for molecular recognition and nanooptical devices [94, 95]. In the vicinity of the metal surface, the local electromagnetic field dramatically enhanced by LSPR results in Raman scattering and fluorescence processes of surface-anchored dye molecules [96, 97]. This fascinating phenomenon has also enabled to increase the absorption coefficient in dye-sensitized solar cells and to enhance photocurrent generation on polymer nanosheets incorporating dyes [98]. The precise architecture and tailor-made fabrication of assemblies of metal nanostructures and photoresponsive sites are important in these achievements primarily. The phenomenon of LSPR induces the stronger electrostatic field than the irradiation light, then it causes that electromagnetic field is enclosed in the metal surface sympathizing the irradiation light with vibrations of its metal free electrons. As mentioned above, the phenomenon of LSPR shows the feature to both the spatial localization onto adjacent metal surface and the enhanced optical-electronic field around metal NPs.

Enhancements of photoluminescence intensities from complex and dye molecules assisted by surface plasmon excitation from metal NPs have been reported in the past [98, 99]. For practical application of these fascinating effects, it is important to control the size of the metal NPs and the distance between the metal NPs and dye, because these factors are affected by the surface plasmon resonance sensitively [92, 93, 97-102]. Recently the techniques of controlling the nanoparticle size and shape have been developed to adequately enable to synthesis plasmonic materials. The control of the distances between metal NPs and dye molecule has also been attempted with techniques of core-shell coat and layer by layer [103]. An enhanced effect of electronic field exponentially increases with the shorter distances between NPs and dye. On the other hand, the nearer the distances for them are, the higher quench effects in which the exited potential transfers from dye to NPs reversibly are [101].

The history of applied to LSPR is so long from its roots in stained glass in church and table glassware in 17th century. Raman scattering of adsorption molecule was expeditiously attracted to utilize this enhanced electric-field in 1980s. Recently the enhanced phosphorescence of metal complexes (Ru, Eu, Cu, Ir etc.) and dye on surface plasmon field is reported by many efforts [104-107]. With the fact, a number of applications are objects for a molecular recognition sensor and a dye-sensitized solar cell.

For the first time Awazu et al. reported the development of plasmonic photocatalyst as an application to the catalyst field in 2008 [108]. In this research, they succeeded that the catalytic activity of TiO_2 with enhanced the optical electric-field was increased seven times as high as catalyst with no enhanced electrical field. Triggered by this report, researchers have attracted a considerable attention to plasmonic photocatalyst, however the most of the interests are the concerns with semiconductor catalysts [109]. Recently, the applications to metal NPs catalyst have been gradually investigated on the organic synthesis [110, 111]. Then the author demonstrated for the first time a new phenomenon in which the photocatalytic activity of metal complex was efficiently enhanced by the assist of LSPR due to Ag NPs [101].

1.6 Purpose of This Study

The synthesis of the heterogeneous photocatalysts containing the noble metal (Ru, Pd, Ir, and Rh) pyridine complexes were performed with the methods of ion-exchange, ship-in-a-bottle and organic modification. These metal complexes are activated by irradiating visible light which occupies half of solar energy. A diffusion of these catalysts responded to visible light can resolve the environment and energy problems such as global warming, air and water pollution, acid rain, and energy source depletion.

The main purposes of this thesis are the evaluation of performance of the metal complexes immobilized on functional materials and the enhancement of the metal complex photocatalysis. An exchange of alkali metal cation in zeolite and an enhancement of electromagnetic field by LSPR were attempted for the increase of selective oxidation activity. An intramolecular electron transfer in binuclear complex was desired to facilitate Suzuki-Miyaura coupling reaction. Moreover, intercalations into strong acidity supports ZrP and $K_4Nb_6O_{17}$ were challenged to high efficiency in water reduction. The optimum reaction conditions were explored by the control of steric, electromagnetic, acidic and polar effect in the reaction field. These approaches are expected to contribute to the expansion of economical and low-energy process in the industrial field.

1.7 Outline of This Thesis

This thesis deals with the design of the metal complex photocatalysts responded to visible light and their applications to chemical reactions such as selective oxidation, hydrogen production, and cross-coupling reaction. These techniques are expected to contribute to the alleviation of environmental problems associated with technological advances.

In Chapter II, the physicochemical properties of $Ru(bpy)_3^{2+}$ complexes incorporated within the cavities of zeolite Y by continuously changing the alkali metal cations (Li, Na, K, Rb, and Cs) were examined. Additionally, it is herein reported that the encapsulation of $Ru(bpy)_3^{2+}$ within zeolite Y cages enables selective photooxidation of styrene derivatives under irradiating visible light in the presence of molecular oxygen. Turnover number (TON) was found to increase as the size of the alkali metal cation decreased and the phosphorescence emission increased.

In Chapter III, for the first time the author demonstrated a new phenomenon in which the photoinduced oxidation activity of a dye in a selective liquid-phase reaction is efficiently enhanced by the aid of the LSPR for Ag NPs. $Ru(bpy)_3^{2+}$ was anchored onto the surface of Ag NPs coated with a sufficiently thin SiO_2 layer. It can be theoretically expected and is herein verified that the enhanced local electromagnetic field near the Ag NPs could boost the excitation rate and quantum efficiency of $Ru(bpy)_3^{2+}$. Thus, the dye exited by the assist of LSPR increased the energy and/or electron transfer to O_2, which ultimately enhances the photooxidation activity.

In Chapter IV, a new concept photoinduced Suzuki-Miyauira coupling reaction by bimetallic $[(bpy)_2Ru(bpm)PdCl_2](PF_6)_2$ (bpm: bipyrimidine) is described. It is expected that the excited ^{3}MLCT driven visible-light at $Ru(bpy)_2(bpm)$ and energy and/or electron transfer from the active Ru complex to the adjacent Pd occurs. It is verified that this active electron rich Pd(0) facilitates the rate-limiting oxidative addition step and ultimately enhances the photocatalytic activity in Suzuki-Miyaura coupling reaction.

In Chapter V, it was demonstrated that a new photocatalyst synthesis by intercalation of $[Ir(ppy)_2(bpy)]PF_6$ and $[Rh(bpy)_3](PF_6)_3$ complex into ZrP layered matrix with enlarged interlayer distances by a simple ion-exchange method. It is proven that the intercalation of both Ir and Rh complexes enable H_2 production in aqueous media without an electron mediator by visible-light photosensitization. To define the roll of the Ir-Rh combination within the macro cavities of ZrP, the relationship between the luminescence characteristics and photocatalytic activities was examined.

In Chapter VI, a new heterogeneous photocatalyst composed of two dimensional system was created with $[Ir(ppy)_2(bpy)]^+$ and $[Rh(bpy)_3]^{3+}$ by a simple ion exchange of $K_4Nb_6O_{17}$ possessing strongly acidity. Different support effects as space nature, acid-base and electron conductivity expressed for ZrP in Chapter V is expected. Ir-Rh/$K_4Nb_6O_{17}$ catalyst was a recyclable heterogeneous photocatalyst for H_2 evolution, suggesting direct electron transfer from Ir to Rh and bypassed electron transfer through $K_4Nb_6O_{17}$ occurred without electron mediator.

Finally, the overall conclusions of this thesis are stated in Chapter VII.

Constitution of this thesis

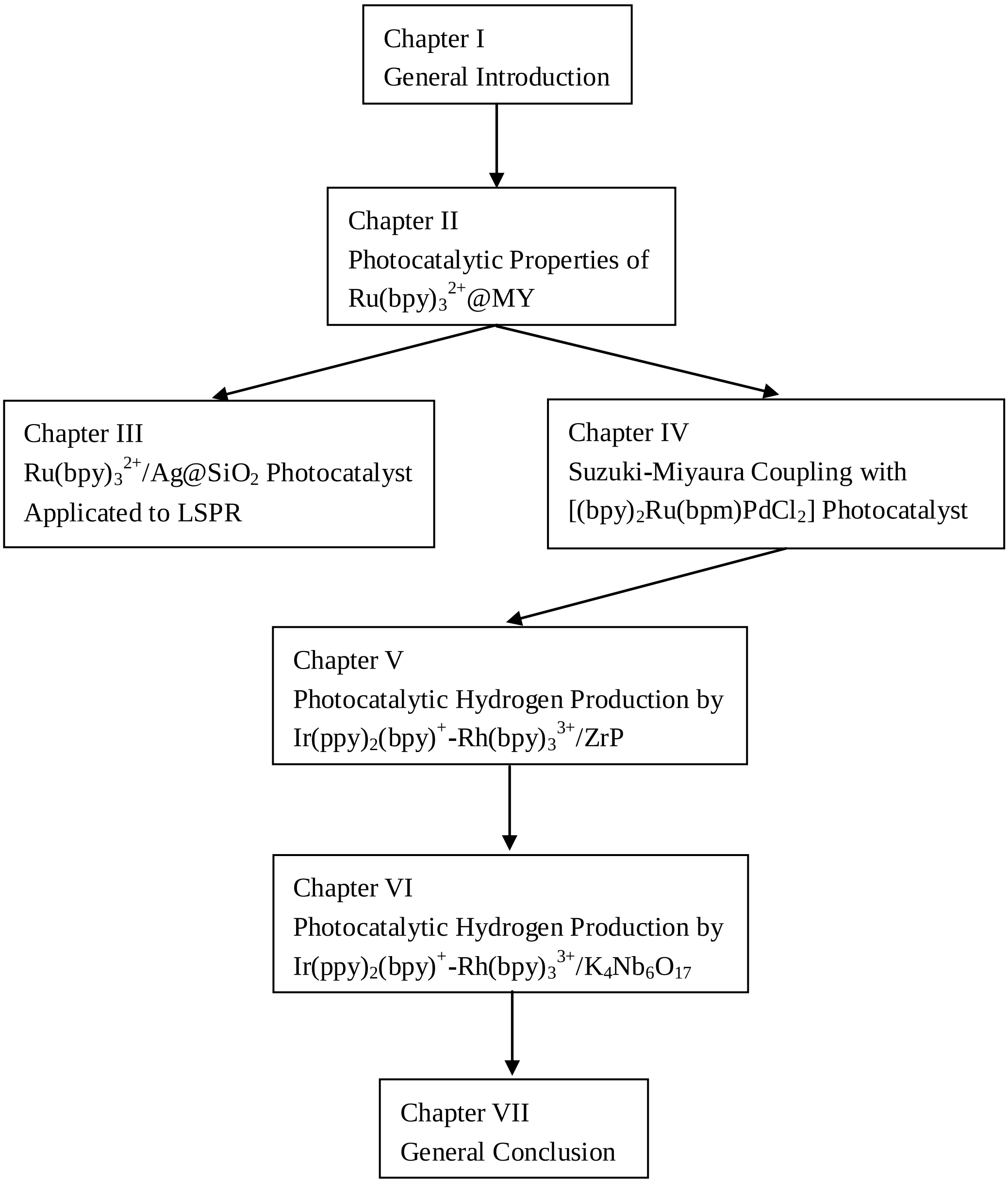

1.8 References

[1] N. Armaroli, V. Balzani, *Angew. Chem. Int. Ed.*, **2007**, 46, 52.

[2] M. R. Anisur, M. H. Mahfuz, M. A. Kibria, R. Saidur, I. H. S. C. Metselaar, T. M. I. Mahlia, *Renew. Sustain. Energy Rev.*, **2013**, 18, 23.

[3] A. Fujishima, K. Honda, *Nature*, **1972**, 238, 37.

[4] H. Yamashita, M. Anpo, *Cur. Opin. Solid State Mater. Sci.*, **2003**, 7, 471.

[5] H. Yamashita, K. Mori, *Chem. Lett.*, **2007**, 36, 348.

[6] K. Fuku, T. Sakano, T. Kamegawa, K. Mori, H. Yamashita, *J. Mater. Chem.*, **2012**, 22, 16243.

[7] S. Shironita, T. Takasaki, T. Kamegawa, K. Mori, H. Yamashita, *Catal. Lett.*, **2009**, 129, 404.

[8] Y. Horiuchi, H. Ura, T. Kamegawa, K. Mori, H. Yamashita, *Appl. Catal. A*, **2010**, 387, 95.

[9] Y. Horiuchi, H. Ura, T. Kamegawa, K. Mori, H. Yamashita, *J. Phys. Chem. C*, **2011**, 115, 15410.

[10] T. Kamegawa, Y. Shimizu, H. Yamashita, *Adv. Mater.*, **2012**, 24, 3697.

[11] G. D. Hager, G. A. Crosby, *J. Am. Chem. Soc.*, **1975**, 97, 7031.

[12] T. J. Meyer, *Pure and Appl. Chem.*, **1986**, 58, 1193.

[13] N. H. Damrauer, G. Cerullo, A. Yeh, T. R. Boussie, C. V. Shank, J. K. McCusker, *Science*, **1997**, 275, 54.

[14] K. Mori, M. Kawashima, K. Kagohara, H. Yamashita, *J. Phys. Chem. C*, **2008**, 112, 19449.

[15] C. Ulbricht, B. Beyer, C. Friebe, A. Winter, U. S. Schubert, *Adv. Mater.*, **2009**, 21, 4418.

[16] K. Mori, M. Tottori, K, Watanabe, M. Che, H. Yamashita, *J. Phys. Chem. C*, **2011**, 115, 21358.

[17] N. Sutin, C. Creutz, E. Fujita, *Comments Inorg. Chem.*, **1997**, 19, 67.

[18] K. Mori, Y. Kubota, H. Yamashita, *Chem. Asian J.*, **2013**, 8, 3207.

[19] M. Kawashima, K. Mori, J. Aoyama, H. Yamashita, *Bull. Chem. Soc. Jpn.*, in press.

[20] K. Mori, J. Aoyama, M. Kawashima, H. Yamashita, *Dalton Trans.*, **2014**, 43, 10541.

[21] A. Inagaki, M. Akita, *Coord. Chem. Rev*., **2010**, 254, 1220.

[22] H. Nitadori, T. Takahashi, A. Inagaki, M. Akita, *Inorg. Chem.*, **2012**, 51, 51.

[23] K. Mori, K. Kagohara, H. Yamashita, *J. Phys. Chem. C,* **2008**, 112, 2593.

[24] M. Martis, K. Mori, H. Yamashita, *Dalton Trans.*, **2014**, 43, 1132.

[25] P. Pfeiffer, H. Glaser, *J Prakt Chem*, **1938**, 134, 151.

[26] K. Mori, K. Kagohara, H. Yamashita, *Top Catal*, **2009**, 52, 586.

[27] M. Irie, T. Fukaminato, T. Sasaki, N. Tamai, T. Kawai, *Nature*, **2002**, 420, 759.

[28] K. Matsuda, K. Takayama, M. Irie, *Inorg. Chem.*, **2004**, 43, 482.

[29] A. Juris, V. Balzani, F. Barigelletti, S. Campagna, P. Belser, A. von Zelewsky, *Coord. Chem. Rev.*, **1988**, 84, 85.

[30] V. M. Miskowski, V. H. Houlding, *Inorg. Chem.*, **1989**, 28, 1529.

[31] K. Mori, K. Watanabe, M. Kawashima, M. Che, H. Yamashita, *J. Phys. Chem. C*, **2010**, 115, 1044.

[32] K. Mori, K. Watanabe, K. Fuku, H. Yamashita, *Chem. Eur. J.*, **2012**, 18, 415.

[33] K. Mori, K. Watanabe, Y. Terai, Y. Fujiwara, H. Yamashita, *Chem. Eur. J.*, **2012**, 18, 11371.

[34] K. Mori, S. Ogawa, M. Martis, H. Yamashita, *J. Phys. Chem. C*, **2012**, 116, 18873.

[35] K. Feng, R.-Y. Zhang, L.-Z. Wu, B. Tu, M.-L. Peng, L.-P. Zhang, D. Zhao, C.-H. Tung, *J. Am. Chem. Soc.*, **2006**, 128, 14685.

[36] K. Mori, H. Yamashita, *J. Japan Petrol. Ins.*, **2011**, 54, 1.

[37] M. Sohmiya, Y. Sugahara, M. Ogawa, *J. Phys. Chem. C*, **2007**, 111, 8836.

[38] Y. Horiuchi, T. Toyao, M. Saito, K. Mochizuki, M. Iwata, H. Higashimura, M. Anpo, M. Matsuoka, *J. Phys. Chem. C*, **2013**, 116, 20848.

[39] T. Kamegawa, M. Saito, T. Watanabe, K.Uchihara, M.Kondo, M. Matsuoka, M. Anpo, *J. Mater. Chem.*, **2011**, 21, 12228.

[40] N. Mizoshita, T. Tani, S. Inagaki, *Chem. Soc. Rev.*, **2011**, 40, 789.

[41] M. Waki, N. Mizoshita, T. Tani, S. Inagaki, *Angew. Chem. Int. Ed.*, **2011,** 50, 11667.

[42] K. Fuku, T. Kamegawa, K. Mori, H. Yamashita, *Chem. Asian J.*, **2012**, 7, 1366.

[43] T. Kamegawa, S. Matsuura, H. Seto, H. Yamashita, *Angew. Chem. Int. Ed.*, **2013**, 52, 916.

[44] K. Mori, A. Kumami, M. Tomonari, H. Yamashita, *J. Phys. Chem. C Lett.*, **2009**, 113, 16850.

[45] T. Kamegawa, N. Suzuki, M. Che, H. Yamashita, *Langmuir*, **2011**, 27, 2873.

[46] S. Okada, K. Mori, T. Kamegawa, M. Che, H. Yamashita, *Chem. Eur. J.*, **2011**, 17, 9047.

[47] S. Okada, S. Ikurumi, T. Kamegawa, K. Mori, H. Yamashita, *J. Phys. Chem. C*, **2012**, 116, 14360.

[48] Y. Kuwahara, K. Nishizawa, T. Nakajima, T. Kamegawa, K. Mori, H. Yamashita, *J. Am. Chem. Soc.*, **2011**, 133, 12462.

[49] Y. Kuwahara, K. Maki, Y. Matsumura, T. Kamegawa, K. Mori, H. Yamashita, *J. Phys. Chem. C*, **2009**, 113, 1552.

[50] K. Mori, A. Hanafusa, M. Che, H. Yamashita, *J. Phys. Chem. Lett.*, **2010**, 1, 1675.

[51] K. Mori, M. Dojo, H. Yamashita, *ACS Catal.*, **2013**, 3, 1114.

[52] K. Mori, Y. Miura, S. Shironita, H. Yamashita, *Langmuir*, **2009**, 25, 11180.

[53] Y. Kuwahara, J. Aoyama, K. Miyakubo, T. Eguchi, T. Kamegawa, K. Mori, H. Yamashita, *J. Catal.*, **2012**, 285, 223.

[54] R. Abe, M. Hara, J. N. Kondo, K. Domen, *Chem. Mater.*, **1998**, 10, 1647.

[55] A. Sinhamahapatra, N. Sutradhar, B. Roy, A. Tarafdar, H. C. Bajaj, A. B. Panda, *Appl. Catal. A*, **2010**, 385, 22.

[56] B. Xiao, X. Wang, H. Huang, M. Zhu, P. Yang, Y. Wang, Y. Du, *J. Phys. Chem. C*, **2013**, 117, 21303.

[57] T. Tanaka, Y. Ogiso, M. Ueda, J. Lee, *ISIJ Int.*, **2010**, 50, 1071.

[58] H. Yamashita, M. Matsuoka, K. Tsuji, Y. Shioya, M. Anpo, M. Che, *J. Phys. Chem.*, **1996**, 100, 397.

[59] H. Yamashita, Y. Ichihashi, M. Anpo, M. Hashimoto, C. Louis, M. Che, *J. Phys. Chem.*, **1996**, 100, 16041.

[60] W. -S. Ju, M. Matsuoka, K. Iino, H. Yamashita, M. Anpo, *J. Phys. Chem. B*, **2004**, 108, 2128.

[61] S. Inagaki, S. Guan, Y. Fukushima, T. Ohsuna, O. Terasaki, *J. Am. Chem. Soc.*, **1999**, 121, 9611.

[62] V. Ramamurthy, J. V. Caspar, D. R. Corbin, D. F. Eaton, *J. Photochem. Photobiol. A*, **1989**, 50, 157.

[63] H. Yamashita, *Zeolite News Letters*, **2004**, 21, 2.

[64] G. Alberti, *Acc. Chem. Res.*, **1978**, 11, 163.

[65] A. Clearfield, *Chem. Rev.*, **1988**, 88, 125.

[66] A. A. Martí, J. L. Colón, *Inorg. Chem.*, **2003**, 42, 2830.

[67] E. J. Rivera, C. Figueroa, J. L. Colón, L. Grove, W. B. Connick, *Inorg. Chem.*, **2007**, 46, 8569.

[68] A. A. Marti, N. Rivera, K. Soto, L. Maldonado, J. L. Colon, *Dalton Trans.*, **2007**, 1713.

[69] M. Gasperin, M.-T. le Bihan, *J. Solid State Chem.*, **1980**, 33, 83.

[70] K. Maeda, M. Eguchi, W. J. Youngblood, T. E. Mallouk, *Chem. Mater.*, **2008**, 20, 6770.

[71] T. Nakato, H. Edakubo, T. Shimomura, *Micropor. Mesopor. Mater.*, **2009**, 123, 280.

[72] J. Ma, J. Wu, J. Zheng, L. Liu, D. Zhang, X. Xu, X. Yang, Z. Tong, *Micropor. Mesopor. Mater.*, **2012**, 151, 325.

[73] T. Nakato, K. Kusunoki, K. Yoshizawa, K. Kuroda, M. Kaneko, *J. Phys. Chem.*, **1995**, 99, 17896.

[74] K. Mori, H. Yamashita, M. Anpo, *RSC Adv.*, **2012**, 2, 3165.

[75] K. Mori, K. Yamaguchi, T. Hara, T. Mizugaki, K. Ebitani, K. Kaneda, *J. Am. Chem. Soc*., **2002**, 124, 11572.

[76] A. Suzuki, *Angew. Chem., Int. Ed.*, **2011**, 50, 6722.

[77] N. Miyaura, A. Suzuki, *Chem. Rev.*, **1995**, 95, 2457

[78] D. Benito-Garagorri, K. Kirchner, *Acc. Chem. Res.*, **2008**, 41, 201.

[79] R. Martin, S. L. Buchwald, *Acc. Chem. Res.*, **2008**, 41, 1461.

[80] M. Osawa, H. Nagai, M. Akita, *Dalton Trans.*, **2007**, 827.

[81] K. Mori, M. Kawashima, H. Yamashita, *Chem. Commun*., in press.

[82] S. Park, J. M. Vohs, R. J. Gorte, *Nature*, **2000**, 404, 265.

[83] B. C. H. Steele, A. Heinzel, *Nature*, **2001**, 414, 345.

[84] M. Gratzel, *Nature*, **2001**, 414, 338.

[85] K. Maeda, K. Domen, *J. Phys. Chem. C*, **2007**, 111, 7851.

[86] A. Kudo, Y. Miseki, *Chem. Soc. Rev.*, **2009**, 38, 253.

[87] S. Min, G. Lu, *J. Hydrogen Energy*, **2012**, 37, 10564.

[88] W. Zhang, R. Xu, *J. Hydrogen Energy*, **2012**, 37, 17899.

[89] K. Okeyoshi, D. Suzuki, R. Yoshida, *Langmuir*, **2012**, 28, 1539.

[90] M. Grasemann, G. Laurenczy, *Energy Environ. Sci.*, **2012**, 5, 8171.

[91] A. Nozaki, T. Kamegawa, T. Ohmichi, H. Yamashita, *Chem Phys Chem*, **2013**, 14, 2534.

[92] K. Fuku, R. Hayashi, S. Takakura, K. Mori, H. Yamashita, *Angew. Chem. Int. Ed.*, **2013**, 52, 7446.

[93] H. Cheng, T. Kamegawa, K. Mori, H. Yamashita, *Angew. Chem. Int. Ed.*, **2014**, 53, 2910.

[94] A. J. Haes, R. P. Van Duyne, *J. Am. Chem. Soc.*, **2002**, 124, 10596.

[95] J. R. Lakowitcz, *Plasmonics*, **2006**, 1, 5.

[96] K. G. Thomas, P. V. Kamat, *Acc. Chem. Res*., **2003**, 36, 888.

[97] Y. Horiuchi, M. Shimada, T. Kamegawa, K. Mori, H. Yamashita, *J. Mater. Chem.*, **2009**, 19, 6745.

[98] N. Fukuda, M. Mitsuishi, A. Aoki, T. Miyashita, *J. Phys. Chem. B*, **2002**, 106, 7048.

[99] M. Mitsuishi, M. Ishifuji, H. Endo, H. Tanaka and T. Miyashita, *Polym. J.*, **2007**, 39, 411.

[100] K. Fuku, S.Takakura, T. Kamegawa, K. Mori, H. Yamashita, *Chem. Lett.*, **2012**, 41,614.

[101] K. Mori, M. Kawashima, M. Che, H. Yamashita, *Angew. Chem. Int. Ed.*, **2010**, 49, 8598.

[102] K. Ishikawa and T. Okubo, *J. Appl. Phys.*, **2005**, 98, 43502.

[103] K. Ray, R. Badugu, J. R. Lakowicz, *Chem. Mater.*, **2007**, 19, 5902.

[104] M. Ihara, K. Tanaka, K. Sakaki, I. Honma, K. Yamada, *J. Phys. Chem. B*, **1997**, 101, 5153.

[105] M. Jebb, P. K. Sudeep, P. Pramod, K. G. Thomas, P. V. Kamat, *J. Phys. Chem. C*, **2007**, 111, 6839.

[106] Y. Wang, X. Zhou, T, Wang, J. Zhou, *Mater. Lett.*, **2008**, 62, 3582.

[107] K. Sugawa, T. Kawahara, T. Akiyama, M. Kobayashi, A. Takahara, S. Yamada, *Chem. Lett.*, **2009**, 38, 326.

[108] K. Awazu, M. Fujimaki, C. Rockstuhl, J. Tominaga, H. Murakami, Y. Ohki, N. Yoshida, T. Watanabe, *J. Am. Chem. Soc.*, **2008**, 130, 1676.

[109] T. Torimoto, H. Horibe, T. Kameyama, K. Okazaki, S. Ikeda, M. Matsumura, A. Ishikawa, H.

Ishihara , *J. Phys. Chem. Lett.*, **2011**, 2, 2057.

[110] S. Sarina, H. Zhu, E. Jaatinen, Q. Xiao, H. Liu, J. Jia, C. Chen, J. Zhao, *J. Am. Chem. Soc.*, **2013**, 135, 5793.

[111] Y. Sugano, Y. Shiraishi, D. Tsukamoto, S. Ichikawa, *Angew. Chem. Int. Ed.*, **2013**, 52, 5295.

Chapter II

Photocatalytic Properties of Tris(2,2’-bipyridine)ruthenium(II) Complexes Encapsulated within Zeolite Y Supercages Exchanged Alkali Metal Cations

2.1 Introduction

The tris(2,2'-bipyridine)ruthenium(II) ($Ru(bpy)_3^{2+}$) complex represents an important class of compounds that possess a rich range of spectroscopic and photophysical properties [1-4]. Much of this interest originates from the potential capacity of the complex as a photosensitizer in the conversion of solar to other useful forms of energy. The ground state electronic configuration of $Ru(bpy)_3^{2+}$ is a singlet state with the six valence electrons in the t_{2g} (π_M) orbitals. Absorption of visible light leads to a metal-to-ligand charge-transfer transition (^{1}MLCT), which is then transferred with unit efficiency to a triplet MLCT state (^{3}MLCT) by intersystem crossing [5, 6]. Because of the enhanced spin-orbit coupling induced by ruthenium, the conversion from ^{1}MLCT to ^{3}MLCT is rapid, $\tau \approx 100$ fs [7]. Much work has focused on understanding the nature of these states by spectroscopic examination of crystals, influence of solvents, and the choice of the ligands and/or substituents [1-4].

Other efforts have been directed toward the investigation of this molecule on a variety of inorganic supports, including micelles, clays, and mesoporous materials [8-11]. Among them, there have been numerous reports dealing with the combination of $Ru(bpy)_3^{2+}$ and zeolites [12-16]. Zeolites are attractive materials for encapsulation of metals, semiconductors, and organic and organometallic complexes [17-22]. Both steric and electrostatic constraints can influence the structure and reactivity of the enclosed species, which frequently results in a lifetime enhancement of short-lived reaction intermediates, including triplet states [23], free radicals [24, 25], and carbocations [26, 27]. Lunsford and co-workers reported the synthesis and optical spectroscopic characterization of $Ru(bpy)_3^{2+}$ in zeolite cages [12]. Dutta et. al. reported the resonance Raman spectra of this complex in zeolite cages and the nature of photoproducts formed upon laser photolysis of a $Ru(bpy)_3^{2+}$-methylviologen-zeolite Y system [13]. This study involved the continuous examination of the structure of the ground and excited states of zeolite-encapsulated $Ru(bpy)_3^{2+}$ by steady-state and time-resolved optical measurements [14]. The choice of zeolite for the evaluation of host-guest interactions was motivated by the following factors. The estimated diameter of $Ru(bpy)_3^{2+}$ is ~ 1.2 nm, and therefore this complex would occupy most of the volume of the zeolite Y supercage (~ 1.3 nm). This occupancy would ensure close proximity of the periphery of the bipyridine ligands to the zeolite framework, the therefore permit a full investigation examining the effect of the interactions between the two species.

Partial substitution of trivalent aluminum ions for tetravalent silicon ions at the lattice positions of zeolites results in a network that bears a net negative charge. The negative charge is compensated by the presence of extra framework alkali metal cations (i.e. Li^+, Na^+, K^+, Rb^+, and Cs^+) without the destruction of the framework structure [28]. Physicochemical characteristics, such as electrostatic potential and electric field within the cage, spin-orbit coupling parameter, and space available for guest molecules within the supercage, are well known to be controlled by these exchangeable charge-compensating alkali metal cations [29, 30]. We have recently reported the $Fe(bpy)_3^{2+}$ complexes contained within alkali metal cation-exchanged zeolite Y [31]. Several parameters, such as the intensity of the MLCT band, the electron density of the Fe atoms, the average distances of the Fe-N bonds, and photooxidation abilities, were found to be systematically altered as the alkali metal cation was changed from Li^+ to Cs^+.

Along these lines, the physicochemical properties of $Ru(bpy)_3^{2+}$ complexes included within the cavities of zeolite Y by continuously varying the alkali metal cations were examined. Although the spectroscopic characteristics and reactivity of $Ru(bpy)_3^{2+}$ in the supercage of zeolite Y have been studied extensively [12-16], the detailed study of the effect of alkali metal cations is unexplored. Additionally, we herein report that the encapsulation of $Ru(bpy)_3^{2+}$ within zeolite Y cages enables selective photooxidation of styrene derivatives under visible-light irradiation in the presence of molecular oxygen (O_2). The catalytic activity was found to increase as the size of the alkali metal cation decreased. This observation can be explained by the alteration of the lowest triplet state of encapsulated $Ru(bpy)_3^{2+}$ with the help of light alkali metal cations. The exploitation of alkali metal cation-guest interactions within the restricted cavities of zeolites is expected to confer new and more effective types of reactivity on the encapsulated guest molecules.

2.2 Experimental

2.2.1 Materials

$Ru(NH_3)_6Cl_3$, alkali metal ion nitrates, and 2,2’-bipyridine (bpy) were purchased from Wako Pure Chemical Ind., Ltd. Solvents and all commercially available organic compounds for catalytic reactions were purified using standard procedures.

2.2.2 Synthesis of $Ru(bpy)_3^{2+}$-encapsulated Zeolite Y

Alkali metal cation-exchanged zeolites Y (Li^+-Y, K^+-Y, Rb^+-Y, and Cs^+-Y) were prepared from Na^+-Y (supplied by Union Syowa K.K., SiO_2/Al_2O_3 = 5, crystal size = 0.3 μm) by a standard ion-exchange procedure at 363 K using aqueous nitrate solutions of alkali metal cations. The obtained alkali metal cation-exchanged zeolite Y samples were calcined at 773 K for 9 h in air. To prepare ruthenium-exchanged zeolites, Na^+-Y (2.0 g) was suspended in an aqueous solution (100 mL) of $Ru(NH_3)_6Cl_3$ (3×10^{-3} $mol \cdot L^{-1}$) and stirred at room temperature for 24 h. During ion-exchange, it was important to maintain the pH at ~ 5 and exclude O_2 to prevent the formation of “ruthenium red” on the zeolite. The zeolite was filtered, washed extensively with deionized water, and dried at room temperature under vacuum. This gave ruthenium-exchanged Na^+-Y (Ru/Na^+-Y) as a white powder. Ru/Li^+-Y, Ru/K^+-Y, Ru/Rb^+-Y, and Ru/Cs^+-Y were prepared by the same method using Li^+-Y, K^+-Y, Rb^+-Y, and Cs^+-Y, respectively. The prepared Ru/Na^+-Y (2.0 g) was refluxed in an ethylene glycol solution (50 mL) of bpy (0.02 $mol \cdot L^{-1}$) for 3 h, followed by filtration, washing with water and ethanol, and drying at room temperature under vacuum to give a $Ru(bpy)_3^{2+}$-encapsulated Na^+-Y ($Ru(bpy)_3^{2+}$@Na^+-Y) as an orange powder. $Ru(bpy)_3^{2+}$@Li^+-Y, $Ru(bpy)_3^{2+}$@K^+-Y, $Ru(bpy)_3^{2+}$@Rb^+-Y, and $Ru(bpy)_3^{2+}$@Cs^+-Y were prepared by the same method using Ru/Li^+-Y, Ru/K^+-Y, Ru/Rb^+-Y, and Ru/Cs^+-Y, respectively. The elemental composition (Al, Si, alkali metal cation, and Ru) was determined by inductively coupled plasma (ICP) analysis.

2.2.3 Characterization

Brunauer-Emmett-Teller (BET) surface area measurements were performed using an ASAP 2010 system (Micromeritics) at 77 K. The sample was degassed under vacuum at 473 K prior to data collection. Powder X-ray diffraction patterns were recorded using a Rigaku RINT2500 diffractometer with Cu Kα radiation (λ = 1.5406 Å). Reflectance spectra of powdered zeolite samples were collected using a Shimadzu UV-2450 spectrophotometer. The reference was $BaSO_4$, and the absorption spectra were obtained by using the Kubelka-Munk function. Infrared spectra were obtained with a JASCO FTIR-6100. Samples were diluted with KBr and compressed into thin disk-shaped pellets. Inductively coupled plasma measurements were performed using a Nippon Jarrell-Ash ICAP-575 Mark II. Photoluminescence measurements were carried out on an F-4500 fluorescence spectrophotometer (Hitachi) at 77 K. Ru K-edge XAFS spectra were recorded using a fluorescence-yield collection technique at the beam line 01B1 station with an attached Si (311) monochromator at SPring-8, JASRI, Harima, Japan (prop. No. 2008A1457). The EXAFS data were normalized by fitting the background absorption coefficient, around the energy region higher than the edge of about 35-50 eV, with the smoothed absorption of an isolated atom. The EXAFS data were examined using the Rigaku EXAFS analysis program. Fourier transformation (FT) of k^3-weighted normalized EXAFS data was performed over the $3.5\ \text{Å} < k/\text{Å}^{-1} < 11\ \text{Å}$ range to obtain the radial structure function. CN (coordination number of scatters), R (distance between an absorbing atom and scatterer), and Debye-Waller factor were estimated by curve-fitting analysis with the inverse FT of the $0.8 < R/\text{Å} < 2.8$ range assuming single scattering.

2.2.4 Liquid-phase Photooxidation

The powdered $Ru(bpy)_3^{2+}$@Na^+-Y (0.02 g), α-methyl styrene (10.0 mmol), and acetonitrile (15 ml) were added to a quartz reaction vessel (30 cc) which was then sealed with a rubber septum. The resulting mixture was bubbled with oxygen for 30 min in dark conditions. Subsequently the sample was irradiated from a sideways direction using a Xe lamp (500 W; SAN-EI ERECTRIC CO., LTD. XEF-501S) through a glass filter (λ > 430 nm) for 24 h with magnetic stirring at ambient pressure and temperature. After the reaction, the resulting solution was recovered by filtration and analyzed by an internal standard technique using a Shimadzu GC-14B with a flame ionization detector equipped with TC-1 columns. The turnover number (TON) was determined by the following equation: TON = (acetophenone [mol])/(Ru atoms on catalyst [mol]).

2.3 Results and Discussion

2.3.1 Characterization of $Ru(bpy)_3^{2+}$-encapsulated Zeolite Y Materials

Zeolite Y belongs to the faujasite family and is composed of tetrahedral SiO_4 and AlO_4 building blocks that form six-membered rings. The combination of four- and six-membered rings results in the formation of large cavities, known as β-cages, with diameters of ~ 1.30 nm [32]. These supercages are connected to each other by tunnels or "windows" with the widest diameter of ~ 0.74 nm. The ratio of cavities to windows in the interior of zeolite Y is 1:3.

With the aim of modifying the electronic field and volume of space inside the zeolite hosts, a series of alkali metal cation-exchanged zeolites Y (Li^+-Y, K^+-Y, Rb^+-Y, and Cs^+-Y) were prepared from Na^+-Y (SiO_2/Al_2O_3 = 5) by standard ion-exchange procedures. The compositions and characteristics of zeolites Y containing alkali metal cations are shown in **Table 1** [29]. The ion-exchanged percentages of these cations exceeded 60%. The void space of the cavity and the BET surface area decreased as the size of the alkali metal cation increased. The Sanderson's electronegativity of each alkali metal cation-exchanged zeolite Y was calculated according to the equation $(S_M^p\, S_H^q\, S_{Al}^r\, S_{Si}^t\, S_O^u)^{1/(p+q+r+t+u)}$, where S_M, S_H, S_{Al}, S_{Si}, and S_O represent the Sanderson's electronegativities of the alkali metal, hydrogen, aluminum, silicon, and oxygen, respectively, and p, q, r, t, and u represent the number of the corresponding element in the unit cell [33]. Sanderson's electronegativity is recognized as a criterion of basicity for zeolites: the average negative charge increases with increasing Al content in the framework and with systematic variation of the alkali metal cations from Li^+ to Cs^+ [34].

Table 1. Compositions and characteristics of the zeolites Y including alkali metal cations.

Zeolite	Unit cell composition	Ionic radius of alkali cation / Å	Space volume of cavity / $Å^3$	Electrostatic field / $VÅ^{-1}$	Sanderson's Electro-negativity	S_{BET} / m^2g^{-1}
Li^+-Y	$Li_{18}Na_{37}Al_{55}Si_{137}O_{384}$	0.68	834	2.1	2.62	729
Na^+-Y	$Na_{55}Al_{55}Si_{137}O_{384}$	0.97	827	1.3	2.58	697
K^+-Y	$K_{46}Na_9Al_{55}Si_{137}O_{384}$	1.33	807	1.0	2.54	659
Rb^+-Y	$Rb_{35}Na_{20}Al_{55}Si_{137}O_{384}$	1.55	796	0.8	2.50	567
Cs^+-Y	$Cs_{35}Na_{20}Al_{55}Si_{137}O_{384}$	1.70	781	0.6	2.45	518

Since the estimated diameter of the $Ru(bpy)_3^{2+}$ complex was too large (~ 1.2 nm) for direct exchange through the zeolite lattice apertures, a procedure for in-situ synthesis of the complex was adopted. The supercages of the alkali metal cation-exchanged zeolite Y were doped with Ru ions and, subsequently, with the ligand bpy through the windows connected to the supercage. Ru loading was significantly less than the alkali metal cation concentration. Moreover, because of the shape of the bpy, this neutral ligand should diffuse to a sufficient extent to form cationic complexes which are homogeneously distributed across the zeolite crystals. The $Ru(bpy)_3^{2+}$ complex occupies most of the volume of the zeolite Y supercage, and the size of the complex ensures that once the molecules are synthesized in the cages, they cannot escape through the windows (**Fig. 1**). The ordered arrangement of supercages within the zeolite framework was anticipated to allow the examination of the physicochemical properties of the encapsulated $Ru(bpy)_3^{2+}$ as a function of the characteristics of the cavity. The characteristics of the cavities were controlled by exchanging alkali metal cations.

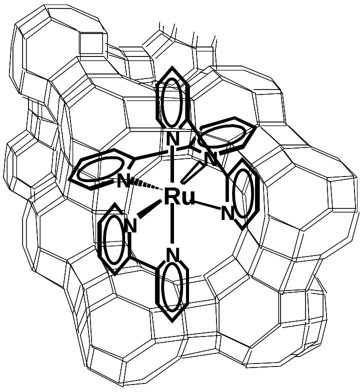

Figure 1. A schematic picture of $Ru(bpy)_3^{2+}$ complex inside the zeolite Y cavities.

As expected, remarkable decreases in BET surface area and BJH pore volume were also observed as the size of the alkali metal cations increased (**Table 2**). TG analysis of the $Ru(bpy)_3^{2+}$@Na^+-Y sample indicated that the ratio of Ru ions to the estimated number of bpy ligands was ca. 1 : 3. This suggests that no free uncomplexed Ru ions were present. Based on these results, along with elemental analysis, the average number of encapsulated $Ru(bpy)_3^{2+}$ complexes per supercage was determined to be 0.21 for $Ru(bpy)_3^{2+}$@Na^+-Y, suggesting that the intermolecular interactions between adjacent $Ru(bpy)_3^{2+}$ in neighboring cages rarely occur under this loading level.

Table 2. Ru loading, BET surface area, and BJH pore volume of the zeolites Y including alkali metal cations.

Zeolite	Ru loading / $\mathrm{mmol\,g^{-1}}$	S_{BET} / $\mathrm{m^2 g^{-1}}$	pore volume / $\mathrm{cm^3 g^{-1}}$
$Ru(bpy)_3^{2+}$@Li^+-Y	0.14	356	0.037
$Ru(bpy)_3^{2+}$@Na^+-Y	0.13	378	0.045
$Ru(bpy)_3^{2+}$@K^+-Y	0.16	340	0.040
$Ru(bpy)_3^{2+}$@Rb^+-Y	0.17	252	0.019
$Ru(bpy)_3^{2+}$@Cs^+-Y	0.16	240	0.019

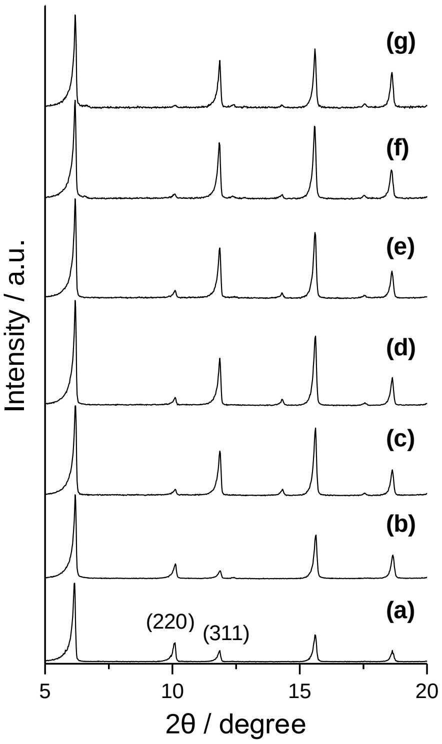

Figure 2. XRD patterns of (a) Na^+-Y zeolite, (b) Ru/Na^+-Y, (c) $Ru(bpy)_3^{2+}$@Li^+-Y, (d) $Ru(bpy)_3^{2+}$@Na^+-Y, (e) $Ru(bpy)_3^{2+}$@K^+-Y, (f) $Ru(bpy)_3^{2+}$@Rb^+-Y, and (g) $Ru(bpy)_3^{2+}$@Cs^+-Y.

An empirically derived relationship between the relative peak intensities of the 220 and 311 reflections in the XRD pattern confirms the formation of a large metal complex ion in the supercage of faujasite-type zeolites: $I_{220} > I_{311}$ for the original zeolite Y, but $I_{220} < I_{311}$ for the zeolite containing large complexes [35]. This change of relative intensity may be associated with the redistribution of randomly coordinated free cations in zeolite Y at sites II and I′. **Fig. 2** shows the XRD patterns of the parent Na^+-Y, Ru/Na^+-Y, and $Ru(bpy)_3^{2+}$-encapsulated zeolite Y containing alkali metal cations.

For zeolite Y and Ru/Na$^+$-Y, I_{220} at 2θ = 10º are greater than I_{311} at 12º, but I_{220} is lower than I_{311} for Ru(bpy)$_3^{2+}$@Na$^+$-Y (**Fig. 2a and b vs d**). Similar changes in the intensities of the 220 and 311 reflections were observed for all Ru(bpy)$_3^{2+}$-encapsulated zeolites Y. This is clear evidence for the formation of complex ions within the supercage. However, no change in relative intensities was observed for Ru(bpy)$_3^{2+}$ ions adsorbed on the external surface of zeolite Y (Ru(bpy)$_3^{2+}$/Na$^+$-Y), which was prepared by impregnation from an aqueous Ru(bpy)$_3$Cl$_2$ solution. For these samples, it can be concluded that the zeolite lattice retained its original random sodium ion distribution.

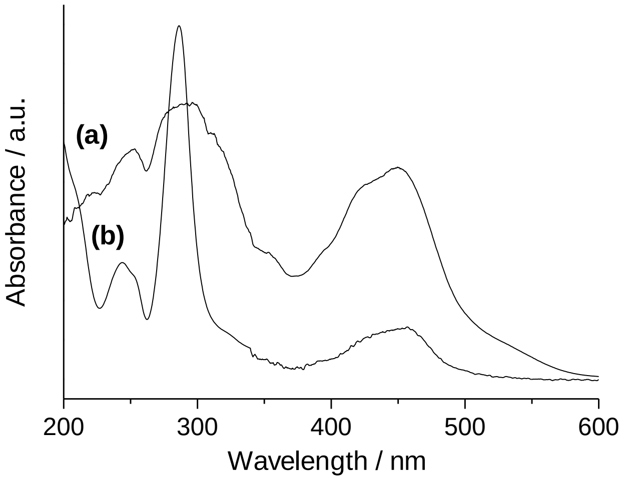

Figure 3. UV-vis spectra of (a) Ru(bpy)$_3^{2+}$@Na$^+$-Y and (b) Ru(bpy)$_3$Cl$_2$ in aqueous solution.

UV-vis diffuse reflectance spectra of Ru(bpy)$_3^{2+}$@Na$^+$-Y, and absorption spectra of Ru(bpy)$_3$Cl$_2$ in an aqueous solution, are shown in **Fig. 3**. No absorption was observed from the ultraviolet to visible region in the absence of metal complexes. The absorption spectrum of Ru(bpy)$_3$Cl$_2$ exhibits a metal-to-ligand (d-π*) charge-transfer (MLCT) band at 457 nm and a π-π* transition of the bpy ligand at around 286 nm [4]. In contrast, the spectrum for the Ru(bpy)$_3^{2+}$@Na$^+$-Y complex exhibits a slight blue shift of the MLCT band (450 nm) and significant broadening of the π-π* transition band. This significant alteration in the absorption spectra can be attributed to the interaction between Ru(bpy)$_3^{2+}$ and the zeolite framework. Possible explanations include: (i) the bpy ligands are distorted to some extent by steric constraints in the supercages, and (ii) that the ground and/or excited state of the MLCT is altered by encapsulation of Ru(bpy)$_3^{2+}$.

The IR spectrum was measured to obtain information about the structure of Ru(bpy)$_3^{2+}$ within the zeolite supercage. As shown in **Fig. 4**, the spectrum of $Ru(bpy)_3Cl_2$ gave bands at 732 and 778 cm^{-1} and these bands were assigned to the deformation of the pyridine ring in the ligand and the out-of-plane C-H bending around the pyridine ring [36], respectively. In the spectrum of $Ru(bpy)_3^{2+}@Na^+$-Y, these bands shifted to shorter wavenumbers, suggesting that the pyridine rings of $Ru(bpy)_3^{2+}$ in the supercage are located under different conditions.

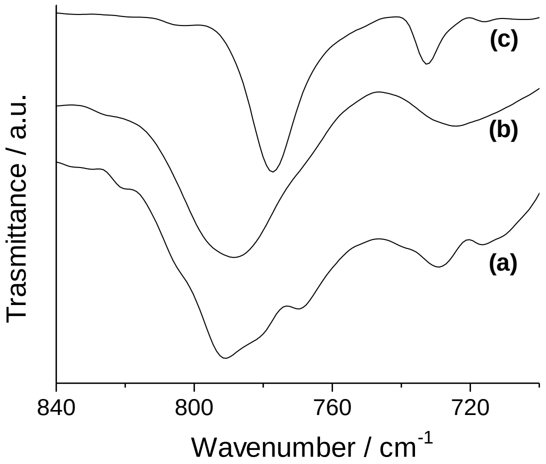

Figure 4. IR spectra of (a) $Ru(bpy)_3^{2+}@Na^+$-Y, (b) Na^+-Y, and (c) $Ru(bpy)_3Cl_2$.

XAFS measurement is an ideal technique to explore the chemical and structural environment of the investigated atoms. **Fig. 5** shows the Ru K-edge X-ray absorption near-edge structure (XANES) spectra of the complexes $Ru(bpy)_3^{2+}$@M-Y and $Ru(bpy)_3Cl_2$ as well as reference Ru compounds. The edge position (measured at the half-height of the edge jump) depends on the electronic charge of the ruthenium ion, and the energies increased in the order: Ru foil (22117.0 eV) < $Ru(bpy)_3Cl_2$ (22122.7 eV) < $Ru(bpy)_3^{2+}$@M-Y (22124.1-22125.0 eV) < RuO_2 (22132.0 eV). Thus, the oxidation state of the $Ru(bpy)_3^{2+}$ complexes are situated between 0 to +4 and the encapsulated Ru ions within zeolite supercages appear to be in an electron-deficient state when compared to free $Ru(bpy)_3Cl_2$. A similar phenomenon was previously observed for a $Fe(bpy)_3^{2+}$ complex encapsulated within zeolite Y [31]. Additionally, the electron density of the Ru atoms slightly increased as the ionic radius of the alkali metal cations increased. *Vide supra*, the basicity of the zeolites, as represented by Sanderson's electronegativity, increases in the order $Li^+ < Na^+ < K^+ < Rb^+ < Cs^+$. This phenomenon significantly influence on the guest molecular, such as organometallic complexes and metal clusters [37]. In a

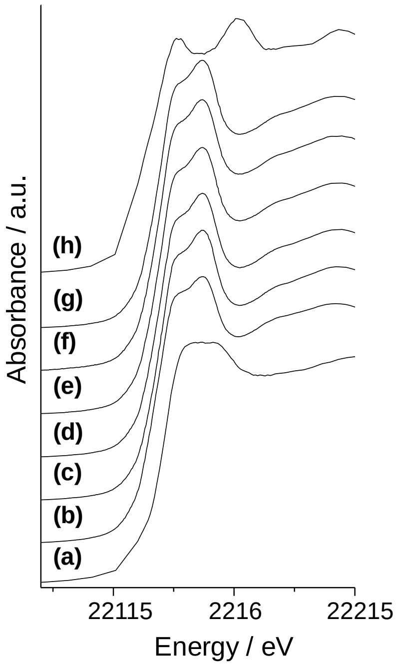

Figure 5. Ru K-edge XANES spectra of (a) RuO_2, (b) $Ru(bpy)_3Cl_2$, (c) $Ru(bpy)_3^{2+}@Li^+$-Y, (d) $Ru(bpy)_3^{2+}@Na^+$-Y, (e) $Ru(bpy)_3^{2+}@K^+$-Y, (f) $Ru(bpy)_3^{2+}@Rb^+$-Y, (g) $Ru(bpy)_3^{2+}@Cs^+$-Y, and (h) Ru foil.

previous study, it was reported that direct electronic charge transfer from the basic zeolite to Pt_5 clusters encapsulated within the cavities rendered them electron-rich, and the charge density on the Pt_5 cluster increased when the alkali metal cations were changed from Li^+ to Cs^+ [38-41]. Analogously, the electron density of the Ru atoms becomes more negative as the cations are varied from Li^+ to Cs^+ in the present $Ru(bpy)_3^{2+}$ complexes contained in zeolite cavities. This behavior can be taken as evidence of strong interactions between the $Ru(bpy)_3^{2+}$ complexes and the host zeolite framework.

The Fourier transforms (FT) of Ru K-edge X-ray absorption fine structure (EXAFS) data for the complexes $Ru(bpy)_3^{2+}$@M-Y and $Ru(bpy)_3Cl_2$ are depicted in **Fig. 6**. All spectra showed a strong peak at around 1.5 Å attributable to a Ru-N bond and a small second shell at ~2.5 Å which is assigned to neighboring carbon atoms. This corroborates a bidentate binding structure. Compared to $Ru(bpy)_3Cl_2$, the first peaks of $Ru(bpy)_3^{2+}$@M-Y are slightly shifted toward shorter interatomic distances. To obtain quantitative information about Ru atom coordination, the first peak was fitted using the Ru-N shell parameter in $Ru(bpy)_3Cl_2$ as standard (CN = 6.0 and R = 2.06 Å, respectively).

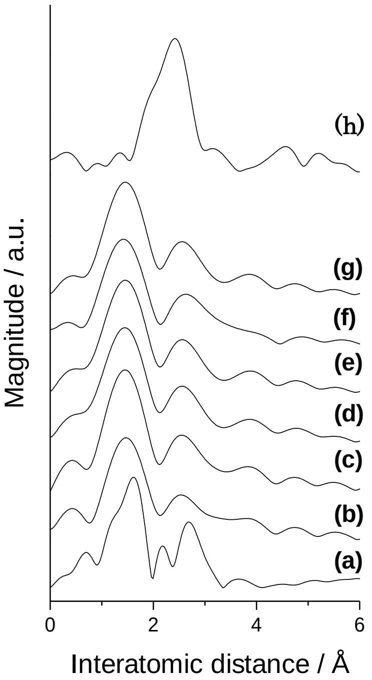

Figure 6. Fourier transforms of k^3-weighted Ru K-edge EXAFS spectra of (a) RuO_2, (b) $Ru(bpy)_3Cl_2$, (c) $Ru(bpy)_3^{2+}$@Li^+-Y, (d) $Ru(bpy)_3^{2+}$@Na^+-Y, (e) $Ru(bpy)_3^{2+}$@K^+-Y, (f) $Ru(bpy)_3^{2+}$@Rb^+-Y, (g) $Ru(bpy)_3^{2+}$@Cs^+-Y, and (h) Ru foil.

Table 3. Edge position and the results of curve-fitting analysis.

Sample	Edge position / eV	*C.N* Ru–N	*R*/Å	$\Delta\sigma^2$/Å^2
$Ru(bpy)_3^{2+}$	22122.7	6.0	2.06	0
$Ru(bpy)_3^{2+}$@Li^+-Y	22125.0	6.4	2.04	0.006
$Ru(bpy)_3^{2+}$@Na^+-Y	22124.6	6.1	2.04	0.007
$Ru(bpy)_3^{2+}$@K^+-Y	22124.6	6.5	2.03	0.003
$Ru(bpy)_3^{2+}$@Rb^+-Y	22124.3	6.3	2.02	0.003
$Ru(bpy)_3^{2+}$@Cs^+-Y	22124.1	6.1	2.02	0.004

As summarized in **Table 3**, curve-fitting analysis of $Ru(bpy)_3^{2+}$@M-Y showed average distances of 2.02-2.04 Å with coordination numbers of 6.1-6.5. Although it is not possible to rule out the involvement of a variety of different Ru species in the zeolite cavity, the Ru complex mainly exists in a monomeric form surrounded by six nitrogen atoms. The average Ru-N distances decreased as the size of the alkali metal cations increased. This observation suggests that the encapsulated $Ru(bpy)_3^{2+}$ complexes may undergo strong shrinking and distortion within the zeolite cavity because of the steric constraints imposed by the limited void space.

The lowest excited state of $Ru(bpy)_3^{2+}$ is ^{3}MLCT which undergoes relatively slow radiation-less transitions and thus exhibits a long lifetime and intense luminescence emission. **Fig. 7** shows the luminescence spectra of $Ru(bpy)_3^{2+}$@M-Y at 77 K. Interestingly, the intensity of the emission increased as the size of the alkali metal cations decreased. The energy positions of the ^{3}MLCT excited state depends on the ligand field strength, the redox properties of the metal and the ligands, and the intrinsic properties of the ligands [42]. Thus, the change in the surrounding media of the $Ru(bpy)_3^{2+}$ significantly influenced the orbital nature of the lowest ^{3}MLCT excited state. Additionally, luminescence maxima were slightly blue shifted in the order: free $Ru(bpy)_3^{2+}$ in an aqueous solution (599 nm) > $Ru(bpy)_3^{2+}$@Na^+-Y (585 nm) > $Ru(bpy)_3^{2+}$@Cs^+-Y (579 nm). Wheeler and Thomas observed a luminescence blue shift upon the adsorption of $Ru(bpy)_3^{2+}$ on colloidal silica [43]. Similar phenomena have also been observed in silica and aluminosilica gels through sol-to-gel conversion and gel aging and drying [10]. Numerous papers are available that deal with the mechanism of the so-called "rigidchromism" that was originally termed by Wringhton and Morse [44-46]. Here, it was hypothesized that a reduction in relaxation as a result of a more rigid state caused the spectral blue shifts. The $Ru(bpy)_3^{2+}$@Cs^+-Y emitted light of shorter wavelength compared to the $Ru(bpy)_3^{2+}$@Na^+-Y complex and this reveals that the Cs^+-Y zeolite provides a less flexible microenvironment because of the larger ionic radius. Add to this blue shift, photoluminescence intensity was also affected in heavier alkali metal cations zeolite because of decrease in quantum yield with the distorted structure discussed by XAFS data mentioned above.

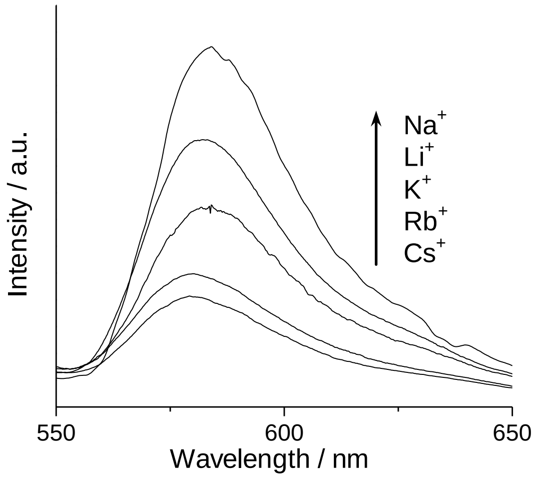

Figure 7. Photoluminescence spectra of $Ru(bpy)_3^{2+}$@M-Y. The data was normalized based on the Ru amount.

2.3.2 Photooxidation by $Ru(bpy)_3^{2+}$-encapsulated Zeolite Y

Selective oxidation of olefins was conducted to investigate the potential catalytic ability of $Ru(bpy)_3^{2+}$-encapsulated zeolite Y and also the influence of the exchanged alkali metal cations on the complexes photocatalytic activities. In contrast to the large number of publications dealing with the photocatalytic decomposition of organic compounds under aerobic conditions [47-49], the number of examples reporting the use of photocatalysis to synthesize a desirable product is sparse [50]. Photocatalysis enabling selective organic transformations may have advantages over conventional thermal reactions because photocatalysis can be performed at room temperature and avoids the use of acid, bases, and other toxic reagents. Organic dyes and homogeneous complexes also exhibit photocatalytic activity towards selective oxidation in the liquid phase. However, while the initial activity of organic-based photocatalysts can be high, the main drawbacks of these compounds are the poor photostability and the difficulty in separating the catalyst from the reaction mixture.

We found that the encapsulation of $Ru(bpy)_3^{2+}$ within zeolite Y cages creates a catalyst which allows highly selective transformation of α-methylstyrene to acetophenone under visible-light irradiation ($\lambda > 430$ nm) and in the presence of molecular oxygen (O_2) at room temperature. No significant reaction was observed either in dark conditions in the presence of $Ru(bpy)_3^{2+}$@M-Y, without O_2 under visible light irradiation, or in the control experiment (i.e. no $Ru(bpy)_3^{2+}$@M-Y) under visible light. Furthermore, photooxidation did not occur to a significant extent in the presence of Na^+-Y or Ru/Na^+-Y under identical reaction conditions. The material balance between α-methylstyrene and the products after the reaction were in reasonable agreement. This showed that undesirable mineralization was avoided. The comparisons of TON based on Ru content are presented in **Fig. 8**. Interestingly, photocatalytic activity varied according to the types of exchanged alkali metal cations present. The total TON increased as the size of the alkali metal cations, viz. $Li^+ > Na^+ > K^+ > Rb^+ > Cs^+$, decreased. This tendency is corroborated with increasing intensity of the luminescence emission of the lowest ^{3}MLCT state. In this case, the major product obtained was acetophenone (> 90 % selectivity) *via* C=C bond cleavage. The formation of the corresponding epoxide and dimers was avoided. This highly selective photooxidation of α-methylstyrene is in marked contrast to the reaction using a homogeneous $Ru(bpy)_3^{2+}$ complex, in which acetophenone, epoxide, and ene products were formed in 49, 29, and 22 % selectivity, respectively. Moreover, dissociated bpy ligands and/or the oxidized bpy species were detected in the homogeneous solution after the reaction. Such photodegradation was insignificant when the $Ru(bpy)_3^{2+}$ complex was contained within the rigid zeolite cavities. XAFS analysis also revealed that no structural changes around the Ru center were observed after the oxidation. These results indicate that the zeolite not only acts as a support but provides a promising microenvironment which allows strict steric control of the reaction intermediate.

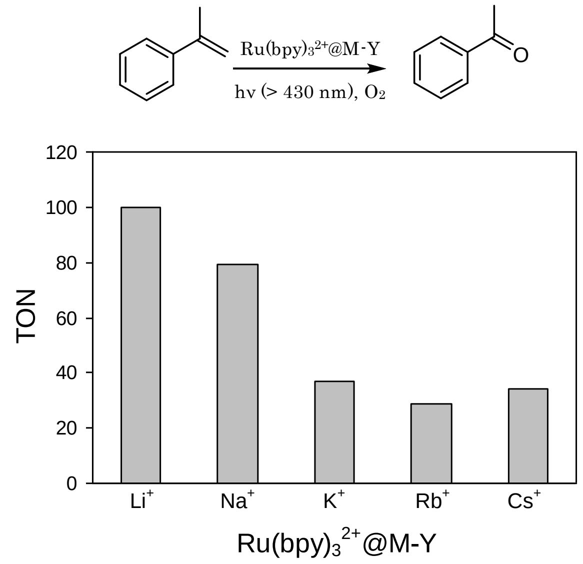

Figure 8. TON for the photocatalytic oxidation of α-methyl styrene using $Ru(bpy)_3^{2+}$@M-Y. Reaction conditions: $Ru(bpy)_3^{2+}$@M-Y (0.02 g), CH_3CN (15 mL), α-methyl styrene (10 mmol), O_2 (1 atm), photo irradiation (24 h, > 430 nm).

A similar phenomenon was observed in the photocatalytic oxidation of styrene to generate benzaldehyde and styrene oxide. Here, zeolite Y with lighter alkali metal cations acted as a more efficient host to accelerate photooxidation compared with those containing heavier alkali metal cations (**Fig. 9**). However Li^+ species were lower catalytic activity than Na^+ cations against the order of periodic table. As this reversal factor, the author proposed a restricted expression of “heavy metal effect” in $Ru(bpy)_3^{2+}$ complex keeping the original structure, decreasing reactivity with organic compound by specific hydration energy and comparative agglomeration of the photosensitizer caused by smaller surface area. As expected, benzaldehyde selectivity increased in the presence of heavier alkali metal cations, which corresponds to a decrease in the volume of the zeolite cavities. $Ru(bpy)_3^{2+}$@Cs^+-Y gave a high product ratio of 8.6 for benzaldehyde to styrene oxide, which significantly exceeded 5.1 and 3.4 observed with $Ru(bpy)_3^{2+}$@Li^+-Y and homogeneous $Ru(bpy)_3^{2+}$, respectively. The predominant formation of acetophenone and the increased selectivity toward benzaldehyde with increasing alkali metal cation size can be attributed to the limited volume of the zeolite cavity. This limited volume interrupts the pathway leading to the slightly larger epoxides. Moreover, it was found that $Ru(bpy)_3^{2+}$@Na^+-Y does not oxidize bulky 1,1-diphenylethylene under identical conditions. This lack of reactivity confirms that steric hindrance is imposed by the zeolite framework, and that the active $Ru(bpy)_3^{2+}$ complexes are located predominantly within the zeolite cavity. The quantum yield of styrene oxidation by $Ru(bpy)_3^{2+}$@Na^+-Y was measured to 14%, which is good agreement with literature.

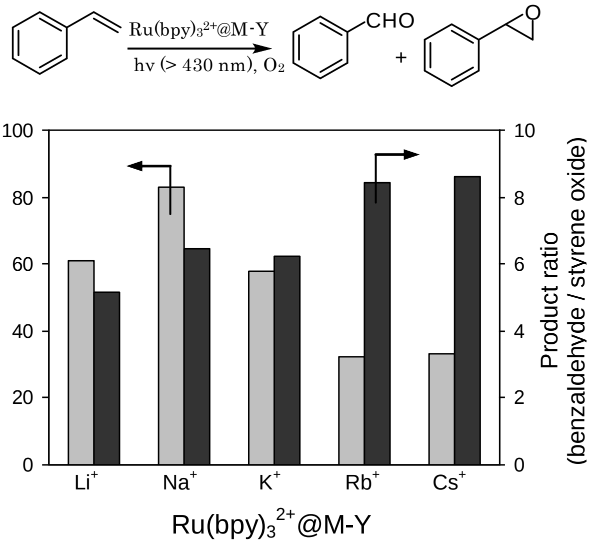

Figure 9. TON and selectivity for the photocatalytic oxidation of styrene using $Ru(bpy)_3^{2+}$@M-Y. Reaction conditions: $Ru(bpy)_3^{2+}$@M-Y (0.02 g), CH_3CN (15 mL), styrene (10 mmol), O_2 (1 atm), photo irradiation (24 h, > 430 nm).

The mechanisms of the photooxidation reaction have been the subject of intense research, since many reactive oxygen species are involved and their roles vary and are dependent on the photocatalytic systems [50-54]. The O_2 molecules can be efficiently activated by the excited ^{3}MLCT state of a photosensitizer, as exemplified by Rose Bengal (RB), Methylene Blue (MB), metal porphyrins, and $Ru(bpy)_3^{2+}$, through an energy-transfer process that generates singlet oxygen ($^1O_2$). Alternatively, electron transfer reaction from the excited triplet of such photosensitizer is possible and leads to the formation of the superoxide anion (O_2*^-). Preliminary studies were performed to help elucidate the reactive oxygen species present in the reaction. The addition of the effective $^1O_2$ scavenger thiourea had little influence on the oxidation rate [55]. The progress of the reaction was extremely slow in a non-polar solvent, such as toluene and hexane. This strong solvent dependence is not compatible with $^1O_2$ oxidation [56, 57]. It has also been reported that the α-methylstyrene is almost inert to photochemically generated singlet oxygen [58]. We also employed isopropanol as the •OH radical quencher, and observed no apparent change in the photoreaction. On the other hand, the addition of superoxide dismutase (SOD), a known scavenger of O_2*^-, significantly inhibited photooxidation [59]. Consequently, it was determined that the present catalytic system does not contain $^1O_2$ and •OH radical species, and the O_2*^- generated by the electron transfer reactions from the excited ^{3}MLCT with O_2 must be the main active species. Photo-induced electron transfer oxidation of α-methylstyrene with O_2 sensitized by dimethoxybenzene has previously been reported, in which a non-singlet-oxygen mechanism is also proposed [58].

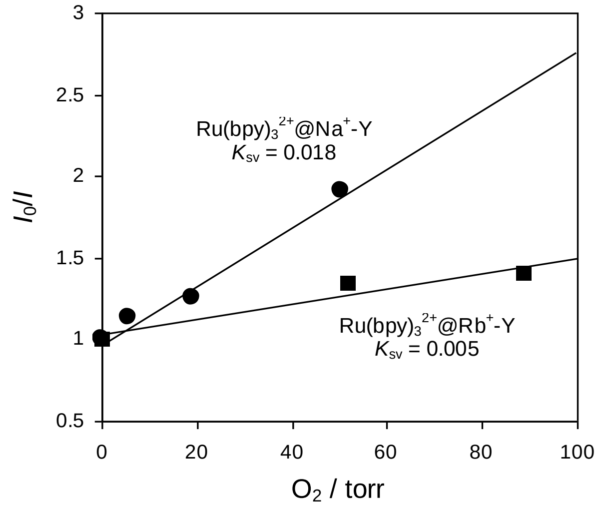

Figure 10. Stern-Volmer plot of the I_0/I values for the yields of the photoluminescence vs. pressure of O_2.

The efficient quenching of the photoluminescence by the addition of O_2 indicates that the $Ru(bpy)_3^{2+}$ complex encapsulated within zeolite cavity easily interacts with O_2 in its ^{3}MLCT state.

The degassing of the O_2 after the quenching of the photoluminescence led to the recovery of the original photoluminescence yield. The Stern-Volmer equation can be obtained for the quenching of the photoluminescence with O_2, as follows

$$I_0/I = 1+K_{sv}[Q]$$

where I_0 and I represent the intensities of photoluminescence in both the absence and presence of O_2, respectively. K_{sv} and [Q] are the quenching rate constant and the concentration of O_2, respectively. As expected, $Ru(bpy)_3^{2+}$@Na^+-Y gave a quenching rate constant of 0.018, which is larger than 0.005 observed with $Ru(bpy)_3^{2+}$@Rb^+-Y (**Fig. 10**). This result corresponds to an increase in photooxidation ability as well as photoluminescence intensity. Conclusively, this study unambiguously demonstrated that zeolites provide a method for controlling photocatalytic activities associated with the electronic configuration of the lowest triplet state of $Ru(bpy)_3^{2+}$ by varying the exchangeable alkali metal cations.

2.4 Conclusion

A series of photocatalysts containing $Ru(bpy)_3^{2+}$ complexes inside zeolite Y cages possessing various extra framework alkali metal cations (Li^+, Na^+, K^+, Rb^+, and Cs^+) have been synthesized via a “ship-in-a-bottle” method. The influence of the alkali metal cations on the spectroscopic properties and photooxidation abilities of the guest $Ru(bpy)_3^{2+}$ complexes in the restricted void space were investigated. Space volume of the cavity, luminescence intensity of the ^{3}MLCT, and the average distances of the Ru-N bonds, were systematically altered by employing a series of exchangeable alkali metal cations. Varying the alkali metal cations from Cs^+ to Li^+ resulted in the enhancement of the photocatalytic ability for oxidation of styrene derivatives using O_2. The presence of lighter alkali metal cations had a positive influence on the electronic configuration of the excited ^{3}MLCT state of $Ru(bpy)_3^{2+}$ complexes within the supercage. The preliminary studies indicate that the catalytic system does not contain $^1O_2$ and •OH radical species, and the $O_2{*}^-$ generated by the electron transfer reactions from the excited ^{3}MLCT state of $Ru(bpy)_3^{2+}$ with O_2 is the primary active species.

2.5 References

[1] T. J. Meyer, *Pure and Appl. Chem.*, **1986**, 58, 1193.

[2] A. Juris, V. Balzani, F. Barigelletti, S. Campangna, P. Belser, V. Zelewsky, *A. Coord. Chem. Rev.*, **1988**, 84, 85.

[3] M. K. De Armond, M. L. Myrick, *Acc. Chem. Res*., **1989**, 22, 364.

[4] K. Kalyanasundarm, *Photochemistry of Polypyridine and Porphyrin Complexes*; Academic Press: London, 1992.

[5] G. D. Hager, G. A. Crosby, *J. Am. Chem. Soc.*, **1975**, 97, 7031.

[6] E. M. Kober, T. J. Meyer, *Inorg. Chem.*, **1984**, 23, 3877.

[7] N. H. Damrauer, G. Cerullo, A. Yeh, T. R. Boussie, C. V. Shank, J. K. McCusker, *Science*, **1997**, 275, 54.

[8] J. K. Thomas, *Acc. Chem. Res*., **1988**, 21, 275.

[9] M. Ogawa, K. Kuroda, *Chem. Rev*., **1995**, 95, 399.

[10] P. Innocenzi, H. Kozuka, T. Yoko, *J. Phys. Chem. B*, **1997**, 101, 2285.

[11] M. Ogawa, M. Tsujimura, K. Kuroda, *Langmuir* **2000**, 16, 4202.

[12] W. DeWllde, G. Peerers, J. H. Lunsford, *J. Phys. Chem.*, **1980**, 84, 2306.

[13] P. K. Dutta, J. A. Invcavo, *J. Phys. Chem.*, **1987**, 91, 4443.

[14] J. A. Invcavo, P. K. Dutta, *J. Phys. Chem.*, **1990**, 94, 3075.

[15] W. Turbevill, D. S. Robins, P. K. Dutta, *J. Phys. Chem.*, **1992**, 96, 5024.

[16] N. B. Castagnola, P. K. Dutta, *J. Phys. Chem. B*, **1998**, 102, 1696.

[17] H. Yamashita, M. Matsuoka, K. Tsuji, Y. Shioya, M. Anpo, M. Che, *J. Phys. Chem*., **1996**, 100, 397.

[18] H. Yamashita, Y. Ichihashi, M. Anpo, M. Hashimoto, C. Louis, M. Che, *J. Phys. Chem.*, **1996**, 100, 16041.

[19] C. Brémard, *Coord. Chem. Rev*., **1998**, 178-180, 1647.

[20] W. -S. Ju, M. Matsuoka, K. Iino, H. Yamashita, M. Anpo, *J. Phys. Chem. B*, **2004**, 108, 2128.

[21] A. Corma, H. Garcia, *Chem. Commun*., **2004**, 13, 1443.

[22] J. C. Fierro-Gonzalez, S. Kuba, Y. Hao, B. C. Gates, *J. Phys. Chem. B*, **2006**, 110, 13326.

[23] H. L. Casal, J. C. Scaiano, *Can. J. Chem.*, **1985**, 63, 1308.

[24] N. J. Turro, A. McDermott, X. Lei, W. Li, L. Abrams, M. F. Ottaviani, H. S. Beard, K. N. Houk, B. R. Beno, P. S. Lee, *Chem. Commun.*, **1998**, 6, 697.

[25] T. Hirano, W. Li, L. Abrams, P. J. Krusic, M. F. Ottaviano, N. J. Turro, *J. Org. Chem.*, **2000**, 65, 1319.

[26] J. C. Scaiano, H. García, *Acc. Chem. Res.*, **1999**, 32, 783.

[27] M. L. Cano, M. N. Chrétien, H. García, J. C. Scaiano, *Chem. Phys. Lett.* **2001**, 345, 409.

[28] D. W. Breck, *Molecular Sieves*; Krieger: FL, **1984**.

[29] V. Ramamurthy, D. F. Eaton, J. V. Caspar, *Acc. Chem. Res*., **1992**, 25, 299.

[30] V. Ramamurthy, J. Shailaja, L. S. Kaanumalle, R. B. Sunoj, J. Chandrasekhar, *Chem. Commun.*, **2003**, 16, 1987.

[31] K. Mori, K. Kagohara, H. Yamashita, *J. Phys. Chem. C*, **2008**, 112, 2593.

[32] S. L. Suib, *Chem. Rev*., **1993**, 93, 803.

[33] J. E. Huheey, E. A. Keiter, R. L. Keiter, *Inorganic Chemistry*, Harper Collins College Publications: New York, 4th edn, **1993**.

[34] R. Heidler, G. O. A. Janssens, W. J. Mortier, R. A. Schoonheydt, *J. Phys. Chem.*, **1996**, 100, 19728.

[35] W. H. Quayle, J. H. Lunsford, *Inorg. Chem.*, **1982**, 21, 97.

[36] Y. Umemura, Y. Minai, T. Tominaga, *J. Phys. Chem. B*, **1999**, 103, 647.

[37] N. Taira, M. Saitoh, S. Hashimoto, H. R. Moon, K. B. Yoon, *Photochem. Photobiol. Sci.*, **2006**, 5, 822.

[38] C. Besoukhanova, J. Guidot, D. Barthomeuf, M. Breysse, J. R. Bernard, *J. Chem. Soc., Faraday Trans. 1*, **1981**, 77, 1595.

[39] T. K. Das, A. J. Chandwadkar, S. Sivasanker, *Stud. Surf. Sci. Catal*., **1998**, 113, 445.

[40] F. J. Maldonado, T. Becue, J. M. Silva, M. F. Riberio, P. Massiani, M. Kermarec, *J. Catal*., **2000**, 195, 342.

[41] S. B. Waghmode, R. Vetrivel, C. S. Gopinath, S. Sivasanker, *J. Phys. Chem. B*, **2004**, 108, 11541.

[42] S. I. Gorelsky, E. S. Dodsworth, A. B. P. Leve, A. A. Vlcek, *Coord. Chem. Rev.*, **1998**, 174, 469.

[43] J. Wheeler, J. K. Thomas, *J. Phys. Chem.*, **1982**, 86, 4540.

[44] M. Wrighton, D. L. Morse, *J. Am. Chem. Soc.*, **1974**, 96, 998.

[45] P. J. Giordano, M. S. Wrighton, *J. Am. Chem. Soc.*, **1979**, 101, 2888.

[46] J. McKiernan, J. C. Pouxviel, B. Dunn, J. I. Zink, *J. Phys. Chem.* **1989**, 93, 2129.

[47] E. Pelizzetti, C. Minero, *Electrochim. Acta*, **1993**, 38, 47.

[48] J. -M. Herrmann, *Catal. Today*, **1999**, 53, 115.

[49] J. Zhao, C. Chen, W. Ma, *Top. Catal.*, **2005**, 35, 269.

[50] A. Maldotti, A. Molinari, R. Amadelli, *Chem. Rev.*, **2002**, 102, 3811.

[51] E. A. Lissi, M. V.Encinas, E. Lemp, M. A. Rubio, *Chem. Rev*., **1993**, 93, 699.

[52] W. Adam, M. Prein, *Acc. Chem. Res*., **1996**, 29, 275.

[53] R. P. Hickerson, F. Prat, J. G. Muller, C. S. Foote, C. J. Burrows, *J. Am. Chem. Soc.*, **1999**, 121, 9423.

[54] J. A. Rengifo-Herrera, J. Sanabria, F. Machuca, C. F. Dierolf, C. Pulgarin, G. Orellana, *J. Sol. Energy Eng.*, **2007**, 129, 135.

[55] G. Crank, A. Mursyidi, *J. Photochem. Photobiol. A: Chem.*, **1992**, 64, 263.

[56] X. Xue, Y. Xu, *J. Mol. Catal. A: Chem*., **2007**, 276, 80.

[57] E. L. Clennan, *Tetrahedron*, **2000**, 56, 9151.

[58] T. Mori, M. Takamoto, Y. Tate, J. Shinkuma, T. Wada, Y. Inoue, *Tetrahedron Lett.*, **2001**, 42, 2505.

[59] J. Li, W. Ma, Y. Huang, M. Chng, J. Zhao, J. C. Yu, *Chem. Commun.*, **2003**, 17, 2214.

Chapter III

Design of Ruthenium(II) Complex Photocatalysts Anchored onto Silver Nanoparticles Coated Silica by the Assist of Localized Surface Plasmon Resonance

3.1 Introduction

Visible-light responsive photocatalysts enabling selective oxidation with molecular oxygen (O_2) is an ongoing challenge as a potential alternative to conventional thermal catalysis. Photochemical excitation can be performed under mild conditions and avoids the use of noxious reagents, which minimizes undesirable side reactions. However, photocatalysis to date has predominantly focused on the degradation of organic pollutants using TiO_2-based materials under UV light irradiation [1-3]; practical examples of positive photocatalysis being applied to the synthesis of specialty chemicals under visible light irradiation are sparse due to the lack of satisfactory activity in many cases [4, 5].

The phenomenon of localized surface plasmon resonance (LSPR) induced by Ag and Au nanoparticles (NPs) has attracted considerable attention because of the great potential to develop sensors for molecular recognition and nano-optical devices [6-9]. In the vicinity of the metal surface, the local electromagnetic field is dramatically enhanced, as are Raman scattering and fluorescence processes of surface-anchored dye molecules [10-12]. This fascinating phenomenon has also made it possible to enhance photocurrent generation on polymer nanosheets incorporating dyes and to increase the absorption coefficient in dye-sensitized solar cells [13, 14]. The primary importance of these achievements lies in the precise architecture and tailor-made fabrication of assemblies of metal nanostructures and photoresponsive sites.

In this Chapter, we demonstrate for the first time a new phenomenon in which the photoinduced oxidation activity of a dye in a selective liquid-phase reaction is efficiently enhanced by the assist of the LSPR of Ag NPs [15-17]. The dye, tris(2,2’-bipyridine)ruthenium(II) complex ($Ru(bpy)_3^{2+}$), was anchored onto the surface of Ag NPs coated with a sufficiently thin SiO_2 layer. In this $Ru(bpy)_3^{2+}$, the absorption of visible light is known to lead to an excited singlet metal-to-ligand charge-transfer (^{1}MLCT), which is then transferred with unit efficiency to a triplet MLCT (^{3}MLCT) by intersystem crossing [18, 19]. In the absence of oxygen, the excited ^{3}MLCT exhibits a phosphorescence emission, on the other hand potentially active oxygen species such as singlet oxygen ($^1O_2$) and superoxide anion (O_2^{*-}) are generated by energy and/or electron transfer reactions from the excited ^{3}MLCT to O_2 [20]. It can be theoretically expected and is herein verified that the enhanced local electromagnetic field near the Ag NPs could boost the excitation rate and quantum efficiency of $Ru(bpy)_3^{2+}$, thus increasing the energy and/or electron transfer to O_2, which ultimately enhances the photooxidation activity.

3.2 Experimental

3.2.1 Materials

$AgNO_3$, $HAuCl_4$, sodium silicate, and tetraethyl orthosilicate were purchased from Wako Pure Chemical Ind., Ltd. Tri-sodium citrate dehydrate was obtained from Nakalai Tesque. Aminopropyl trimethoxysilane and $Ru(bpy)_3Cl_2$ were supplied from Sigma-Aldrich Co. Inc. 3-(Triethoxysilyl)-propylsuccinic acid (TESP-SA) anhydride was purchased from Gelest Inc. Solvents and all commercially available organic compounds for catalytic reactions were purified using standard procedures.

3.2.2 Synthesis of Ag@SiO_2

At first, a colloidal dispersion of Ag NPs was prepared by dropwise 16 mL of degassed aqueous solution of sodium citrate (0.54 mmol) into 400 mL of boiling aqueous solution containing $AgNO_3$ (0.82 mmol) under vigorous stirring. After the reflux for 1 h under an Ar atmosphere, the reaction solution cooled to room temperature. The as-prepared Ag NPs solution was centrifuged and washed with distillated water several times. Next, a 6.0 ml of ethanol solution containing aminopropyl trimethoxysilane (0.042 mmol) was added to the 1.8 L aqueous solution of as-synthesized Ag NPs (0.46 mM). The mixture was stirred for 30 min at room temperature, and finally a 200 mL of aqueous solution containing sodium silicate (0.07 g) was added to allow the sol-gel condensation. After stirring for 24 h, the encapsulated particles were repeatedly centrifuged and washed using excess distillated water, giving an Ag@SiO_2.

3.2.3 Synthesis of $Ru(bpy)_3^{2+}$/Ag@SiO_2

At first, the modification of Ag@SiO_2 was performed by the treatment with TESP-SA anhydride (0.19 mmol) in 60 mL toluene solution for 24 h. The colloidal solution was centrifuged and washed with toluene several times and dried under vacuum over night. Next, the obtained material was treated under aqueous condition to allow hydrolysis reaction of reactive anhydride group to carboxylic units. After 3 h, the solution was centrifuged and washed with distillated water several times. Finally, the obtained material was treated with 15 mL aqueous solution containing $Ru(bpy)_3Cl_2$ (0.87 μmol) at room temperature. After 24 h, the solution was centrifuged and washed with distillated water several times, affording a $Ru(bpy)_3^{2+}/Ag@SiO_2$ (Ru: 0.05 wt%).

3.2.4 Synthesis of $Ru(bpy)_3^{2+}/SiO_2$

The method to prepare the silica nanoparticles is based on the modified Stöber synthesis. In one-pot process, a 50 mL of ethanol solution containing tetraethyl orthosilicate (1.2 ml), 5 mL of ammonia (20%), and 8 mL of distillated water was stirred at room temperature. After 1 h, the solution was centrifuged, washed with ethanol, and dried under vacuum. The modification with TESP-SA anhydride and the attachment of $Ru(bpy)_3Cl_2$ was performed by the same method for the synthesis of $Ru(bpy)_3^{2+}/Ag@SiO_2$.

3.2.5 Synthesis of $Ru(bpy)_3^{2+}/Ag$

At first, colloidal Ag NPs stabilized with 3-mercaptpropionic acid (3-MPA; HSC_2H_2COOH) was prepared as follows**.** $AgNO_3$ (10 mmol), 14 N aq. ammonium (26.0 ml), and 3-MPA (1 mmol) were dissolved in distillated water (15 ml) (solution A). Separately, $NaBH_4$ (2 mmol), and 14 N aq. ammonium (2.0 ml) were dissolved in distillated water (15 ml) (solution B). The above solution A and B were slowly added to 300 mL of distillated water over 30 min at room temperature. After 30 min, the mixture was centrifuged, washed with distillated water, and stored in distillated water. The attachment of $Ru(bpy)_3Cl_2$ was performed by the same method for the synthesis of $Ru(bpy)_3^{2+}/Ag@SiO_2$.

3.2.6 Synthesis of $Ru(bpy)_3^{2+}/Au@SiO_2$

A colloidal dispersion of Au NPs was prepared by a modified synthetic procedure involving seed formation and seed growth using an aqueous solution of $HAuCl_4$ and sodium citrate [21]. The as-prepared Au NPs solution was modified with aminopropyl trimethoxysilane and encapsulated by thin silica layer using sodium silicate. Finally, the modification with TESP-SA anhydride and the attachment of $Ru(bpy)_3Cl_2$ was performed by the same method for the synthesis of

$Ru(bpy)_3^{2+}/Ag@SiO_2$.

3.2.7 Characterization

Powder X-ray diffraction patterns were recorded using a Rigaku RINT2500 diffractometer with Cu Kα radiation (λ = 1.5406 Å). Reflectance spectra were collected using a Shimadzu UV-2450 spectrophotometer. The elemental composition was determined by inductively coupled plasma (ICP) analysis using a Nippon Jarrell-Ash ICAP-575 Mark II. Photoluminescence measurements were carried out on a fluorolog-3 spectrofluorometer (Horiba) at 293 K. TEM micrographs were obtained with a Hitachi Hf-2000 FE-TEM equipped with a Kevex energy-dispersive X-ray detector operated at 200 kV. Ag K-edge and Ru K-edge XAFS spectra were recorded using a fluorescence-yield collection technique at the beam line 01B1 station with an attached Si (311) monochromator at SPring-8, JASRI, Harima, Japan (prop. No. 2009B1127). The EXAFS data were normalized by fitting the background absorption coefficient, around the energy region higher than the edge of about 35-50 eV, with the smoothed absorption of an isolated atom. The EXAFS data were examined using the Rigaku EXAFS analysis program. Fourier transformation (FT) of k^3-weighted normalized EXAFS data was performed over the $3.5 \text{ Å} < k/\text{Å}^{-1} < 11 \text{ Å}$ range to obtain the radial structure function.

3.2.8 Liquid-phase Photooxidation

The photocatalyst (20 mg), α-methyl styrene (10.0 mmol), and acetonitrile (15 ml) were added to a quartz reaction vessel (30 mL) which was then sealed with a rubber septum. The resulting mixture was sonicated and bubbled with molecular oxygen for 30 min in dark conditions. Subsequently the sample was irradiated from a sideways direction using a Xe lamp (500 W; SAN-EI ERECTRIC CO., LTD. XEF-501S) through a glass filter (λ > 430 nm) for 24 h with magnetic stirring at ambient pressure and temperature. After the reaction, the resulting solution was centrifuged and the supernatant was analyzed by an internal standard technique using a Shimadzu GC-14B with a flame ionization detector equipped with TC-1 columns. The turnover number (TON) was determined by the following equation: TON = (acetophenone [mol])/(Ru atoms on catalyst [mol]).

3.3 Results and Discussion

3.3.1 Characterization of Ru(bpy)$_3^{2+}$/Ag@SiO$_2$, Ru(bpy)$_3^{2+}$/SiO$_2$, Ru(bpy)$_3^{2+}$/Ag and Ru(bpy)$_3^{2+}$/Au@SiO$_2$

A colloidal dispersion of Ag NPs was prepared using AgNO$_3$ in the presence of sodium citrate. To make the silver vitreophilic, a bifunctional ligand, aminopropyl trimethoxysilane, was bound to the surface of the Ag NPs. Further protection with a passive thin SiO$_2$ layer was performed using sodium silicate, giving Ag@SiO$_2$. Next, the Ag@SiO$_2$ was modified with TESP-SA anhydride as a organic functional molecule, which bears a reactive anhydride group and subsequently forms two

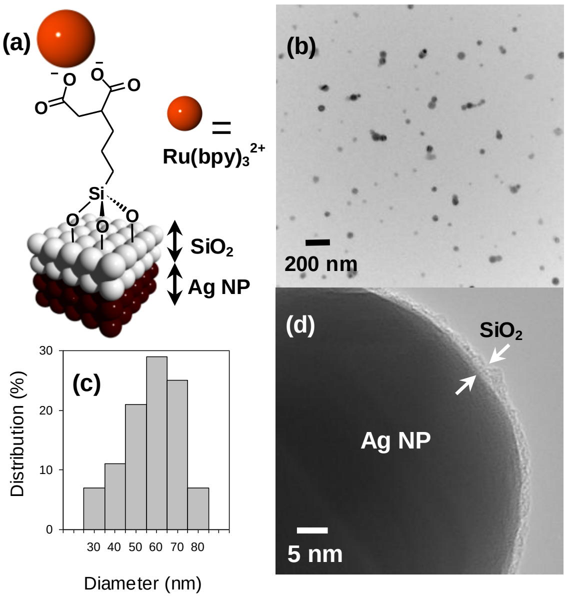

Figure 1. (a) Illustration of surface structure, (b) TEM-image, (c) size-distribution diagrams, and (d) HR-TEM image of Ru(bpy)$_3^{2+}$/Ag@SiO$_2$.

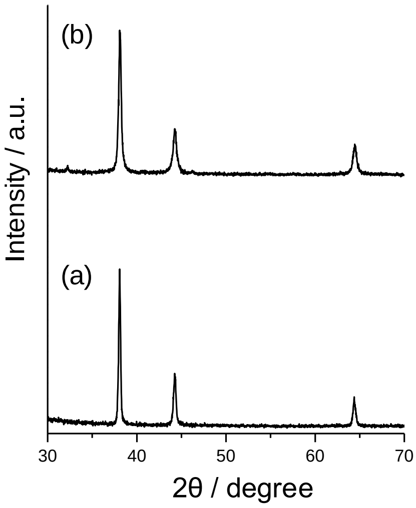

Figure 2. XRD patterns of (a) Ru(bpy)$_3^{2+}$/Ag@SiO$_2$ and (b) Ru(bpy)$_3^{2+}$/Ag.

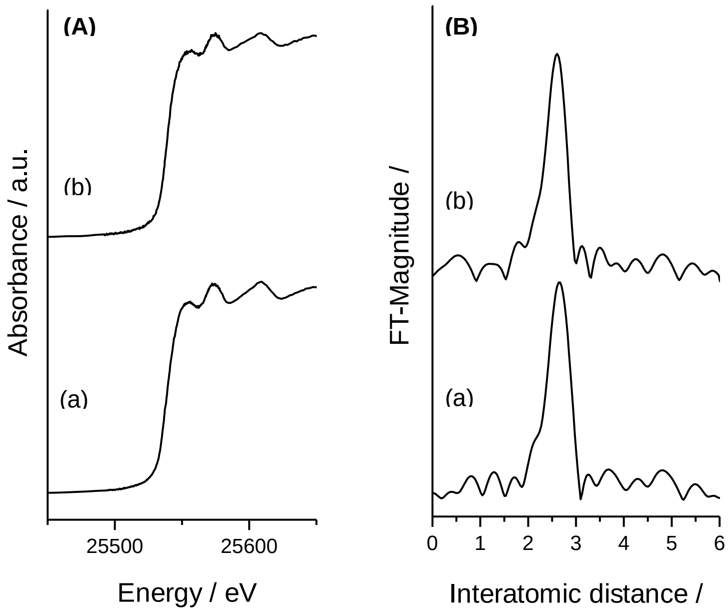

Figure 3. (A) Ag K-edge XANES spectra and (**B**) FT-EXAFS spectra for (a) Ru(bpy)$_3^{2+}$/Ag@SiO$_2$ and (b) Ru(bpy)$_3^{2+}$/Ag.

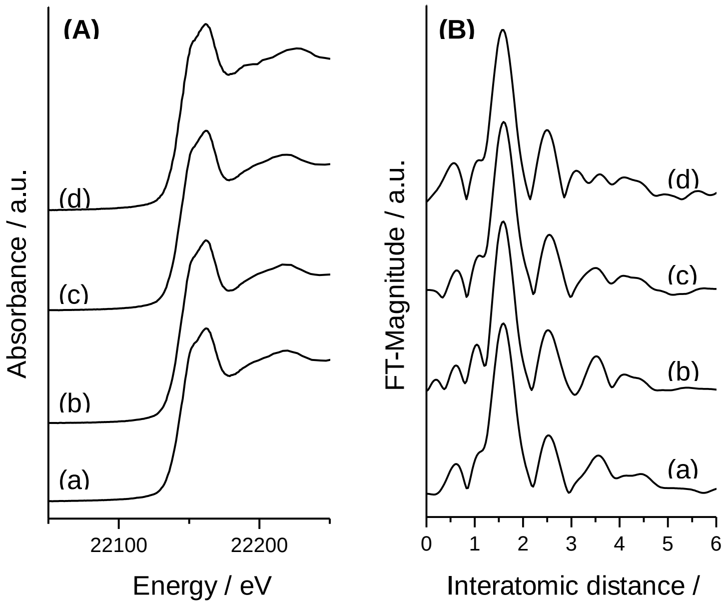

Figure 4. (A) Ru K-edge XANES spectra and (**B**) FT-EXAFS spectra for (a) Ru(bpy)$_3^{2+}$, (b) Ru(bpy)$_3^{2+}$/Ag@SiO$_2$, (c) Ru(bpy)$_3^{2+}$/Ag, and (d) Ru(bpy)$_3^{2+}$/SiO$_2$.

carboxylic units after hydrolysis. Finally, Ru(bpy)$_3^{2+}$ can be successfully attached *via* electrostatic interaction with the two -COO$^-$ groups, affording Ru(bpy)$_3^{2+}$/Ag@SiO$_2$ (Ru: 0.05 wt%) (**Fig. 1a**). In XRD patterns, formation of the Ag metal as a single phase was confirmed by the peaks of 38°, 44°, and 64° originating from (111), (200) and (220), respectively (**Fig. 2**). Ag K-edge EXAFS spectra show that Ag metals keep the as synthesized oxidation state and the distance of interatomic (**Fig. 3**).

TEM images of the NPs showed a spherical form with an average particle size of 58 nm (**Fig. 1b, c**). The thickness of the SiO_2 layer was determined to be about 2-3 nm based on HR-TEM images (**Fig. 1d**). The Ru K-edge XANES spectrum was quite similar to that observed for the free $Ru(bpy)_3^{2+}$. FT-EXAFS showed a strong peak at around 1.5 Å attributable to a Ru-N bond and a small second shell at ~2.5 Å assigned to neighboring carbon atoms, together confirming a bidentate binding structure in the Ru(II) oxidation state (**Fig. 4**).

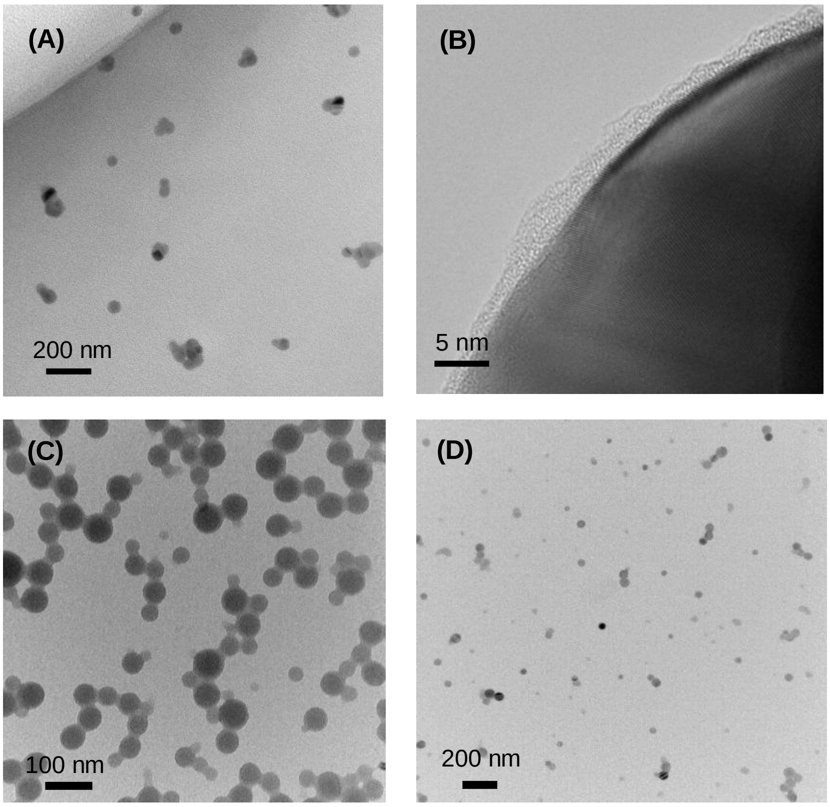

Figure 5. (**A**) TEM image and **(B)** HR-TEM image, of $Ru(bpy)_3^{2+}/Au@SiO_2$. TEM images of **(C)** $Ru(bpy)_3^{2+}/SiO_2$ and **(D)** $Ru(bpy)_3^{2+}/Ag$.

In comparison, $Ru(bpy)_3^{2+}/Au@SiO_2$ was obtained by the same method with colloidal Au NPs. The average diameter and the thickness of the SiO_2 layer were determined to be 61 nm and 3 nm by TEM analysis, respectively (**Fig. 5A, B**). In order to elucidate the great benefit of the metal core in enhancing photoinduced oxidation ability by LSPR, colloidal SiO_2 NPs without metal (average diameter: 55 nm) were prepared by the Stöber method [22], followed by the same surface modification process with TESP-SA anhydride (**Fig. 5C**). Colloidal Ag NPs without the thin SiO_2 layer (average diameter: 51 nm) were also synthesized in the presence of 3-MPA as a stabilizing ligand (**Fig. 5D**) [23]. $Ru(bpy)_3^{2+}$ can be easily attached to these reference materials to the same degree of loading to give $Ru(bpy)_3^{2+}/SiO_2$ and $Ru(bpy)_3^{2+}/Ag$, respectively. XAFS analysis revealed that $Ru(bpy)_3^{2+}$ kept its original structure in the case of the $Ru(bpy)_3^{2+}/Ag@SiO_2$ as shown in **Fig. 4**.

As shown in **Fig 6A**, UV-vis spectra of $Ru(bpy)_3^{2+}/Ag@SiO_2$ and $Ru(bpy)_3^{2+}/Ag$ samples exhibit a MLCT band at 450 nm and a π-π* transition for the bpy ligand at around ~290 nm as well as a peak due to the surface plasmon absorption of Ag NPs centered around 400 nm. In the case of the $Ru(bpy)_3^{2+}/Au@SiO_2$, an additional surface plasmon absorption of Au NPs are observed at around ~550 nm. As expected, the phosphorescence emission intensity of the $Ru(bpy)_3^{2+}$ dye associated with $Ag@SiO_2$ is enhanced under degassing conditions at room temperature [24], which is twice as large as that of the sample without Ag NPs due to optical electric-field (**Fig. 6B**). The Ag core NPs is more advantageous than Au core NPs in the enhancement of the phosphorescence emission intensity, which implies that the approximate wavelength of MLCT and plasmon absorption is advantage. The Ag NPs without a SiO_2 layer exhibits marked quenching of the excited $Ru(bpy)_3^{2+}$ dye, and therefore it suggests importance to control distance between NPs and dye [25, 26]. Then an exploration of optimum distance is tried with thin film in which a control of spacer is easy. Layer-by-Layer assembly is based on the sequential adsorption of polycations and polyanions onto a solid substrate and enables to control 2.1 nanometer intervals [27]. In this case, when the distance between NPs and dye was about 7 nm, the enhanced magnetic field by LSPR was the most effective.

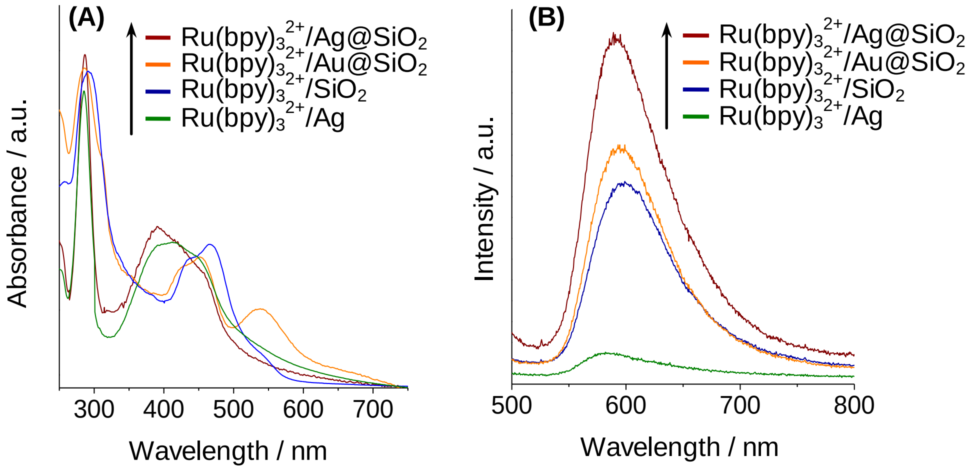

Figure 6. (A) UV-vis spectra and (B) photoluminescence spectra (λ_{ex} = 450 nm) at room temperature.

3.3.2 Liquid-phase Photooxidation of $Ru(bpy)_3^{2+}/Ag@SiO_2$, $Ru(bpy)_3^{2+}/SiO_2$, $Ru(bpy)_3^{2+}/Ag$ and $Ru(bpy)_3^{2+}/Au@SiO_2$

The $Ru(bpy)_3^{2+}/Ag@SiO_2$ system was found to be an effective photocatalyst for the selective oxidation of styrene derivatives to oxygenated products under visible-light irradiation ($\lambda > 400$ nm) in the presence of O_2 at room temperature (**Fig. 7**) [28, 29]. No reaction was observed either under dark conditions in the presence of O_2 or under visible-light irradiation without O_2. Furthermore, photooxidation did not occur in the presence of $Ag@SiO_2$ without anchoring of the $Ru(bpy)_3^{2+}$ dye under identical conditions. The material balance between the substrates and products after the reaction was in reasonable agreement, which indicated that undesirable mineralization was negligible. The TON based on Ru content approached up to 860 in the oxidation of α-methyl styrene using $Ru(bpy)_3^{2+}/Ag@SiO_2$, which is larger than that of the $Ru(bpy)_3^{2+}/SiO_2$ system by a factor of ca. 2. More significantly, the catalyst could be completely recovered without the leaching of active components. In the oxidation of α-methyl styrene, the recovered $Ru(bpy)_3^{2+}/Ag@SiO_2$ retained 90 % of its original photocatalytic activity, suggesting that this photooxidation proceeded on the $Ru(bpy)_3^{2+}$ attached to the $Ag@SiO_2$ surface without detached Ru species. $Ru(bpy)_3^{2+}/ Au@SiO_2$

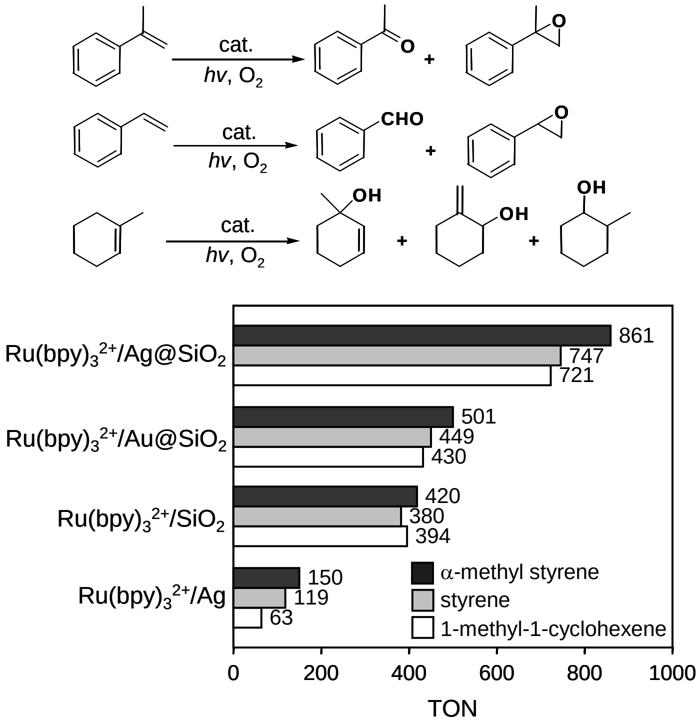

Figure 7. TON for the photocatalytic oxidation of styrene derivatives and 1-methyl-1-cyclohexene using O_2.

showed a slight enhancement of photocatalytic activity, but the Ag core NPs is also proven to be more advantageous than Au core NPs. Again, the use of the Ag NPs without the SiO_2 layer deactivated the photoinduced oxidation ability to a significant extent. Similar phenomena were observed in the oxidation of 1-methyl-1-cyclohexene [28, 29].

This tendency is consistent with increased phosphorescence emission from the lowest ^{3}MLCT state. The efficient quenching of the emission upon addition of O_2 indicates that the $Ru(bpy)_3^{2+}$ dye efficiently interacts with O_2 in the ^{3}MLCT state. The Stern-Volmer equation, ($I_0/I = 1+k_{sv}[Q]$), can be used to represent quenching of the emission by O_2, where I_0 and I represent the intensities of emission in both the absence and presence of O_2, respectively. k_{sv} and [Q] are the quenching rate constant and the concentration of O_2, respectively. As expected, $Ru(bpy)_3^{2+}/Ag@SiO_2$ gave a k_{sv} value of 4.8, which is much larger than the value of 1.3 observed for $Ru(bpy)_3^{2+}/SiO_2$. This result clearly indicates the smooth interaction of the ^{3}MLCT state with O_2 in the presence of Ag NPs, and corresponds well to the observed increase in phosphorescence emission intensity as well as the photoinduced oxidation ability. Conclusively, the present study has unambiguously demonstrated that interaction with the LSPR of Ag NPs can enhance the photocatalytic activity of a dye complex anchored to the surface. The importance of the sufficiently thin SiO_2 layer is also confirmed. It is known that the electromagnetic field enhanced near the metal NPs by the LSPR exponentially decays with getting away from metal surface [30]. However some investigations proved that the specific distance between metal and dye play a crucial role for attaining maximum effect of LSPR [31, 32]. Therefore the SiO_2 layer, not only offers chemical inertness, transparency, and versatility for the conjugation of dye molecules, but also provides a spacer to limit quenching *via* energy transfer with the core Ag NPs, thus optimizing the LSPR effect. We also point out the importance of the use of Ag core. Some reports have proved that Ag NPs gave much higher LSPR enhancement effect than Au NPs [33-35]. One possible explanation is that the surface plasmon from Au NPs does not couple to the excitation wavelength of Ru complex dye, while the plasmon resonance frequency generated on Ag NPs may closely matched excitation frequency of the dye to offer reasonable enhancement.

3.4 Conclusion

In summary, we have proposed a new class of nano-sized photocatalysts composed of core-shell Ag@SiO_2 NPs with an anchored $Ru(bpy)_3^{2+}$ dye. The enhanced electromagnetic field in the vicinity of the Ag NPs due to the LSPR significantly enhances absorption of the dye, which ultimately results in the enhancement of emission intensity and catalytic activity for the photooxidation reaction using O_2. This work provides a novel pathway to the design of new photocatalysts enabling selective organic transformation even under limited light exposure.

3.5 References

[1] E. Pelizzetti, C. Minero, *Electrochim. Acta*, **1993**, 38, 47.

[2] J. -M. Herrmann, *Catal. Today*, **1999**, 53, 115.

[3] J. Zhao, C. Chen, W. Ma, *Top. Catal.*, **2005**, 35, 269.

[4] *Homogeneous Photocatalysis*; M. Chanon, Ed.; Vol. 2, Wiley Series in Photoscience and Photoengineering, 1997.

[5] A. Maldotti, A. Molinari, R. Amadelli, *Chem. Rev.*, **2002**, 102, 3811.

[6] D. Hall, *Anal. Biochem*., **2001**, 288, 109.

[7] J. R. Lakowitcz, *Anal. Biochem*., **2001**, 298, 1.

[8] A. J. Haes, R. P. Van Duyne, *J. Am. Chem. Soc.*, **2002**, 124, 10596.

[9] J. R. Lakowitcz, *Plasmonics*, **2006**, 1, 5.

[10] K. G. Thomas, P. V. Kamat, *Acc. Chem. Res*., **2003**, 36, 888.

[11] L. Lu, A. Kobayashi, K. Tawa, Y. Ozaki, *Chem. Mater*., **2006**, 18, 4894.

[12] Y. Horiuchi, M. Shimada, T. Kamegawa, K. Mori, H. Yamashita, *J. Mater. Chem.*, **2009**, 19, 6745.

[13] M. Ihara, K. Tanaka, K. Sakaki, I. Honma, K. Yamada, *J. Phys. Chem. B*, **1997**, 101, 5153.

[14] N. Fukuda, M. Mitsuishi, A. Aoki, T. Miyashita, *J. Phys. Chem. B*, **2002**, 106, 7048.

[15] T. Hirakawa, P. V. Kamat, *J. Am. Chem. Soc.*, **2005**, 127, 3928.

[16] H. Li, Z. Bian, J. Zhu, Y. Huo, H. Li, Y. Lu, *J. Am. Chem. Soc.*, **2007**, 129, 4538.

[17] K. Awazu, M. Fujimaki, C. Rockstuhl, J. Tominaga, H. Murakami, Y. Ohki, N. Yoshida, T. Watanabe, *J. Am. Chem. Soc.*, **2008**, 130, 1676.

[18] G. D. Hager, G. A. Crosby, *J. Am. Chem. Soc.*, **1975**, 97, 7031.

[19] A. Juris, V. Balzani, F. Barigelletti, S. Campagna, P. Belser, A. V. Zelewsky, *Coord. Chem. Rev.*, **1988**, 84, 85.

[20] K. Mori, M. Kawashima, K. Kagohara, H. Yamashita, *J. Phys. Chem. C*, **2008**, 112, 19449.

[21] K. R. Brown, D. G. Walter, M. J. Natan, *Chem. Mater*., **2000**, 12, 306.

[22] W. Stöber, A. Fink, *J. Colloid Interface Sci*., **1968**, 26, 62.

[23] K. Mori, A. Kumami, M. Tomonari, H. Yamashita, *J. Phys. Chem. C*, **2009**, 113, 16850.

[24] H. Tanaka, Mitsuishi, T. Miyashita, *Chem. Lett*., **2005**, 34, 1246.

[25] T. Huang, R. W. Murray, *Langmuir*, **2002**, 18, 7077.

[26] M. Jebb, P. K. Sudeep, P. Pramod, K. G. Thomas, P. V. Kamat, *J. Phys. Chem. B*, **2007**, 111, 6839.

[27] K. Ray, R. Badugu, J. R. Lakowicz, *Chem. Mater.*, **2007**, 19, 5902.

[28] T. Mori, M. Takamoto, Y. Tate, J. Shinkuma, T. Wada, Y. Inoue, *Tetrahedron Lett*., **2001**, 56, 9151.

[29] T. L. Pettit, M. A. Fox, *J. Phys. Chem*., **1986**, 90, 1353.

[30] Kerker, M. *J. Colloid Interface Sci*., **1985**, 105, 297.

[31] N. K. Chaudhari, M. Kim, H. K. Kim, S.-H. Choi, K. R. Yoon, K. -S. Lee, J. -S. Yu, *J. Nanosci. Nanotech.*, **2008**, 8, 4747.

[32] S. D. Standridge, G. C. Schatz, J. T. Hupp, *J. Am. Chem. Soc.*, **2009**, 131, 8407.

[33] T. D. Neal, K. Okamoto, A. Scherer, *Opt. Exp*., **2005**, 13, 5522.

[34] K. R. Catchpole, A. Polman, *Appl. Phys, Lett*., **2008**, 93, 191113.

[35] K. Kim, H. Ryoo, K. S. Shin. *Langmuir*, **2010**, 26, 10827.

Chapter IV

Synthesis and Appplication to Visible-light-driven Suzuki-Miyaura Coupling Reaction by Ru-Pd Binuclear Complex

4.1 Introduction

The search for efficient solar energy conversion has attracted considerable attention owing to increasing energy and environmental concerns [1]. Photocatalysis enabling selective molecular transformations under visible sunlight irradiation is a permanent challenge as a potential alternative to conventional thermal catalysis. Photochemical excitation can be performed under mild conditions and circumvents the use of toxic reagents, which minimizes undesirable side reactions. However, current application has predominantly focused on the photo reduction of H^+ and CO_2 or oxidation reactions [2-7]; practical examples of positive photocatalysis being applied to the synthesis of specialty organic chemicals via carbon-carbon bond-formations are limited [8-10].

Palladium-mediated cross-coupling reactions between aryl halides and nucleophiles, exemplified by Suzuki-Miyaura coupling reaction, have received wide interest due to its enormous synthetic potential to form new carbon-carbon bonds [11]. New classes of Pd complexes having Pd-carbon σ bonds, e.g. palladacycle complexes [12], PCP pincer-type complexes [13], and N-heterocyclic carbenes (NHCs) [14], have led to significant breakthroughs in this area. The first step of the catalytic cycle is an addition of the aryl halide to the $Pd(0)L_n$ (L = ligand) to afford a σ-arylpalladium(II) complex, *trans*-$ArPd(II)XL_n$, which undergoes the reaction with base followed by transmetalation with organoborane, and the final product is generated by reductive elimination [15]. In most cases, the oxidative addition is the rate determining step of the catalytic cycle, thus the primary importance to improve the catalytic activities and lower the reaction temperatures lies in the designing electron-rich Pd(0) complexes based on electron-donating and sterically hindered special ligands [13, 16].

In this Chapter, we proposed a new photo-assisted Suzuki-Miyauira coupling reaction by bimetallic $[(bpy)_2Ru(bpm)PdCl_2](PF_6)_2$ (abbreviated as Ru-Pd complex, bpy: bipyridine, bpm: bipyrimidine) for the first time (**Scheme 1**). It is well known that the $Ru(bpy)_3^{2+}$ and its derivatives absorb visible light as photosensitizer and lead to an excited singlet metal-to-ligand charge transfer (^{1}MLCT), which is then transferred with unit efficiency to a triplet MLCT (^{3}MLCT) by intersystem crossing [17]. The excited ^{3}MLCT exhibits a phosphorescence emission [18, 19], while electron transfer reactions to the adjacent accepters occur [8]. We envisioned and herein verified that the excited Ru(II)-polypyridyl moiety could boost the formation of active electron rich Pd(0) and facilitates the rate-limiting oxidative addition step, which ultimately enhances the photocatalytic activity in Suzuki-Miyaura coupling reaction.

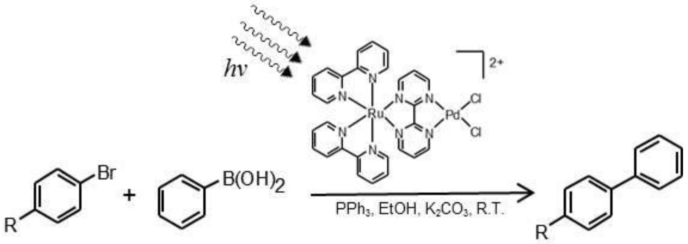

Scheme 1. Photo-assisted Suzuki-Miyaura coupling reaction mediated by Ru-Pd complex.

4.2 Experimental

4.2.1 Materials

$Ru(bpy)_2Cl_2\cdot 2H_2O$, 2,2'-bipyrimidine (bpm), $Pd(CH_3CN)_2Cl_2$ and $Pd(bpy)Cl_2$ were purchased from Sigma-Aldrich Co. Inc. Solvents and all commercially available organic compounds for catalytic reactions were purified using standard procedures.

4.2.2 Synthesis of $[(bpy)_2Ru(bpm)PdCl_2](PF_6)_2$

In a typical preparation, $Ru(bpy)_2Cl_2\cdot 2H_2O$ (Aldrich, 2.0 mmol) was suspended in 60 ml of degassed ethanol-water and refluxed under nitrogen for 3 h. 2,2'-Bipyrimidine (bpm: Aldrich, 4.0 mmol) was added and further refluxed for 3 h. Afterwards, the complex was precipitated by the addition of a saturated aqueous solution of KPF_6 and collected by vacuum filtration. This material was dissolved in 30 ml of acetone, filtered, and reprecipitated by the addition of 200 ml of anhydrous ether. A mixture of $[(bpy)_2Ru(bpm)](PF_6)_2$ (0.4 mmol) and $Pd(CH_3CN)_2Cl_2$ (0.44 mmol) was refluxed in acetone (50 ml) for 2 h, giving $[(bpy)_2Ru(bpm)PdCl_2](PF_6)_2$.

4.2.3 Characterization

^{1}H spectra were recorded on a NMR spectrometer (240 MHz) in CH_3CN-d_3 solution. $[(bpy)_2Ru(bpm)](PF_6)_2$: ^{1}H NMR (300 MHz, CD_3CN, 298 K, relative to Me_4Si): δ 7.40-7.50 ddd, 4H, bpy), 7.60 (t, 2H, bpm), 7.70 (m, 2H, bpy), 7.85 (t, 2H, bpy), 8.05 (d, 2H, bpm), 8.10 (m, 4H, bpy), 8.50 (dd, 2H, bpy), 9.10 (dd, 2H, bpm).

$[(bpy)_2Ru(bpm)PdCl_2](PF_6)_2$: ^1H NMR (300 MHz, CD_3CN, 298 K, relative to Me_4Si): δ 7.40 (m, 4H, bpy), 7.50 (t, 2H, bpm), 7.70 (m, 2H, bpy), 7.90 (d, 2H, bpy), 8.05 (d, 2H, bpm), 8.10 (m, 4H, bpy), 8.50 (d, 4H, bpy), 9.20 (d, 2H, bpm).

Photoluminescence measurements were carried out on a flurolog-3 spectrofluorometer (Horiba). UV-vis diffuse reflectance spectra of samples were collected using a Shimadzu UV-2450 spectrophotometer. The work was supported by the Grant-in-Aid for Scientific Research from the Ministry of Education, Culture, Sports, Science and Technology of Japan (252892890) and JSPS Asian CORE Program. A part of this work was also performed under a management of 'Elements Strategy Initiative for Catalysts & Batteries (ESICB)' supported by MEXT.

4.2.4 Suzuki-Miyaura Coupling Reaction

A typical example of this reaction is as follows. Into a Pyrex reaction vessel (30 cm^3) were placed bromobenzene (5×10^{-2} mmol), phenylboronic acid (5×10^{-2} mmol), catalyst (5×10^{-4} mmol), PPh_3 (1×10^{-3} mmol) and K_2CO_3 (5×10^{-2} mmol), EtOH (10 mL). The reaction mixture was pursed with Ar for 20 min under dark conditions, and then irradiated using a Xe lamp (500 W; SAN-EI ERECTRIC CO., ltd. XEF-501S) through a glass filter ($\lambda \geq 420$ nm) for 6 h with magnetic stirring at ambient pressure and temperature. Analytical GC was performed using a Shimadzu GC-14B with a flame ionization detector equipped with TC-1 columns.

4.3 Results and Discussion

4.3.1 Characterization of $[(bpy)_2Ru(bpm)PdCl_2](PF_6)_2$

$[(bpy)_2Ru(bpm)](PF_6)_2$ was prepared according to a literature procedure [20]. A mixture of $[(bpy)_2Ru(bpm)](PF_6)_2$ and $Pd(CH_3CN)_2Cl_2$ was reflux in acetone solution for 2h, giving a $[(bpy)_2Ru(bpm)PdCl_2](PF_6)_2$, which was characterized by NMR spectroscopy [21]. The UV-vis spectra of the complexes are illustrated in **Fig. 1**. A mononuclear Ru complex without Pd center exhibits intense UV absorption (λ_{max} =250-300 nm) attributed to a ligand centered $\pi \rightarrow \pi^*$ transition and a visible absorption (λ_{max} =400-500 nm) due to a MLCT. The low energy absorption bands in the visible region were slightly broader than that of the $Ru(bpy)_3^{2+}$ complex because of the overlapping with the MLCT transition of d(Ru) → π*(bpy) and d(Ru) → π* (bpm) [22]. A dinuclear Ru-Pd complex also shows the similar absorption spectrum owing the incorporation of Ru(II)-polypyridyl moiety, and a low energy absorption band due to MLCT is slightly shifted to longer wavelength.

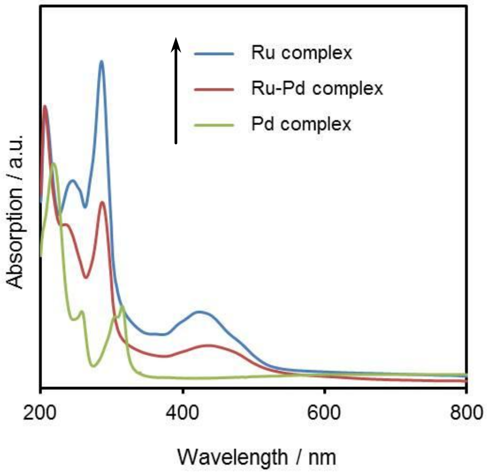

Figure 1. UV-vis spectra of $[(bpy)_2Ru(bpm)](PF_6)_2$, $[(bpy)_2Ru(bpm)PdCl_2](PF_6)_2$ and $(bpy)PdCl_2$ complexes in EtOH solution.

The emission spectra were measured in degassed ethanol solution at room temperature (λ_{ex} =420 nm). As shown in **Fig. 2**, the emission of the mononuclear Ru complex can be observed at 656 nm, which is ascribed to the lowest lying ^{3}MLCT [(dπ(Ru) → π* (bpy)] or [(dπ(Ru) → π* (bpm)] owing to the dominant LUMO character. It is known that its intensity is slightly lower than that of the $Ru(bpy)_3^{2+}$ complex because of the presence of a quenching pathway by the lone-pair electrons of the bpm ligand [23]. The emission of the Ru(II)-polypyridyl moiety substantially quenched upon introduction of the Pd center, implying that an intramolecular electron transfer process is enhanced. The red shift of the maximum wavelength is attributed to the lowering of the π*-energy level of bpm, which resulted in decrease [(dπ(Ru) → π*(bpy)] ^{3}MLCT emission energy [21]. A mixture of the mononuclear Ru complex and the $(bpy)PdCl_2$ complex exhibited an essentially same intensity as that of only mononuclear Ru complex, suggesting that covalent linkage of the two metal units is essential for attaining effective electron transfer from Ru to Pd moiety, presumably because of the short life time $[Ru(bpy)_2(bpm)]^{2+}$ (90 ns) [24].

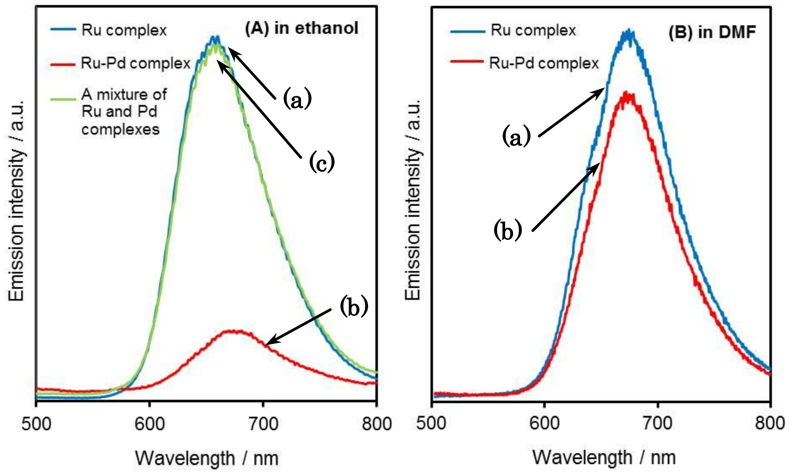

Figure 2. Emission spectra of (a) $[(bpy)_2Ru(bpm)](PF_6)_2$, (b) $[(bpy)_2Ru(bpm)PdCl_2](PF_6)_2$ and (c) a physical mixture of $[(bpy)_2Ru(bpm)](PF_6)_2$ and $(bpy)PdCl_2$ in EtOH solution (**A**) and in DMF solution (**B**) (λ_{ex} =420 nm).

4.3.2 Suzuki-Miyaura Coupling Reaction of $[(bpy)_2Ru(bpm)PdCl_2](PF_6)_2$

As shown in **Table 1**, Suzuki-Miyaura coupling reaction of bromobenzene (**1**) and phenylboronic acid (**2**) were carried out in the presence of PPh_3 (2.0 mol%) and K_2CO_3 (100 mol%) in ethanol solvent at room temperature. The comparison of cross-coupling activity was valued with turnover number (TON). As expected, the visible light irradiation (λ > 420 nm) significantly enhanced the catalytic activity compared to that under dark conditions by a factor of 2 using Ru-Pd complex (1.0 mol%), giving the corresponding coupling product. No significant reaction was observed either in the presence of the mononuclear Ru complex or in the blank experiment under visible light irradiation. The enhancement of photocatalytic activity cannot be observed using a mixture of mononuclear Ru complex and $(bpy)PdCl_2$ complex, and be also performed using a $(bpy)PdCl_2$ expectantly. This result is well collaborated with the results of phosphorescence measurement. By action spectrum, it is also confirmed that only absorbed photon assists this reaction expectantly. Similar enhancement was also observed in the reaction of iodobenzene and chlorobenzene as an aryl halide even though chlorobenzene is poor at reactivity in cross coupling. The catalytic activity in the absence of PPh_3 was extremely low whose TON corresponds to ca.1, indicating that PPh_3 acts as a reductant of Pd(II) and stabilizer of in situ generated Pd(0) [25]. Electronic variation of the *p*-substituted aryl bromides (R = Cl, OCH_3, CH_3) did not significantly affect the reaction rates and the corresponding coupling products were obtained.

Table 1. Suzuki-Miyaura coupling reactions of bromobenzenes under several sets of conditions.[a]

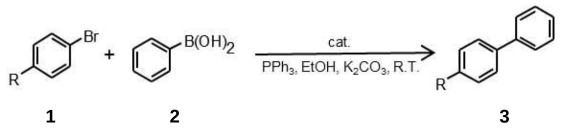

entry	R=	catalyst	light	TON
1	H	$[(bpy)_2Ru(bpm)PdCl_2](PF_6)_2$	vis[b]	10.0
2	H	$[(bpy)_2Ru(bpm)PdCl_2](PF_6)_2$	dark	6.0
3	H	$[(bpy)_2Ru(bpm)](PF_6)_2$ and $(bpy)PdCl_2$ (1:1 physical mixture)	vis	6.2
4	H	$[(bpy)_2Ru(bpm)](PF_6)_2$ and $(bpy)PdCl_2$ (1:1 physical mixture)	dark	5.2
5	H	$(bpy)PdCl_2$	vis	6.0
6	H	$(bpy)PdCl_2$	dark	6.0
7	Cl	$[(bpy)_2Ru(bpm)PdCl_2](PF_6)_2$	vis	12.1
8	Cl	$[(bpy)_2Ru(bpm)PdCl_2](PF_6)_2$	dark	8.1
9	CH_3	$[(bpy)_2Ru(bpm)PdCl_2](PF_6)_2$	vis	10.0
10	CH_3	$[(bpy)_2Ru(bpm)PdCl_2](PF_6)_2$	dark	4.2

[a] Reaction conditions: bromobenzene (5×10^{-2} mmol), phenylboronic acid (5×10^{-2} mmol), catalyst (5×10^{-4} mmol), PPh_3 (1×10^{-3} mmol) and K_2CO_3 (5×10^{-2} mmol), EtOH (10 mL), Ar atmosphere, 6 h. [b] Irradiation from the side using a 500 W Xe lamp through the glass filter ($\lambda > 420$ nm).

With respect to the bases, K_2CO_3 gave the best result, while the reaction using NEt_3 and Cs_2CO_3 were slightly retarded the photocatalytic reaction. This result is in contrast to that with the visible-light promoted Sonogashira coupling reaction using $PdCl_2(CH_3CN)_2$, $P(t\text{-}Bu)_3$ and $Ru(bpy)_3^{2+}$, in which NEt_3 acts as a favorable base to afford the coupling products [13]. Among the solvents examined, ethanol was excellent solvent, while acetonitrile, DMF and THF gave poor results. This behavior may be explained by the suppression of electron transfer from Ru to Pd moiety in such polar aprotic solvents with high coordination ability; the decrease of emission intensity of the dinuclear Ru-Pd complex relative to mononuclear Ru complex in DMF is not remarkable compared with that in ethanol (**Fig. 2B**). Thus the use of ethanol solvent is more advantageous in enhancing the photocatalytic activity. The detail study to understand this phenomenon further is under investigation.

The present dinuclear Ru-Pd complex allows the oxidative addition of alkyl halide and its product has been previously established by MS and NMR spectroscopy [22]. The dinuclear complex maintains the original structure after coupling reactions by confirming UV-vis spectra. In the Ru-Pd complex system, the competitive Suzuki-Miyaura coupling reactions in an equimolar mixture of *p*-substituted bromobenzenes using **2** under visible-light irradiation gave a Hammett ρ value of 0.37, which is substantially smaller than 0.69 obtained under the conventional dark conditions. This low ρ value indicates the acceleration of the oxidative addition, which is considered the rate-determining step in the Suzuki-Miyaura coupling reaction, by the formation of active electron rich Pd(0) species via electron transfer from excited Ru species to Pd(0). The XAFS measurement suggests that the Pd species keeps its original monomeric structure even after the reaction without the formation of Pd agglomeration (**Fig. 3**). Moreover, Pd K-edge XANES spectrum after the reaction showed a slight shift of edge position toward lower energy compared to that before reaction, indicating that the Pd species change to lower oxidation state after the reaction.

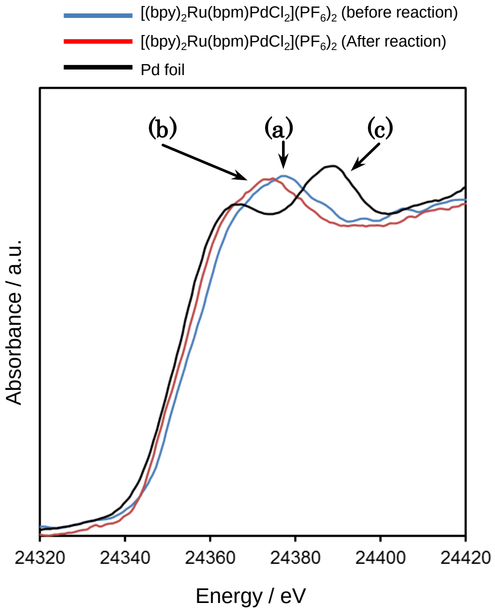

Figure 3. Pd K-edge XANES spectra of $[(bpy)_2Ru(bpm)PdCl_2](PF_6)_2$ complexes before and after the catalytic reaction and Pd foil.

4.4 Conclusion

In conclusion, we demonstrated the harvesting light energy for attaining organic transformation by the bimetallic molecule complex consists of Ru(II)-polypyridyl derivatives as a visible light absorption unit and catalytically active Pd site enabling Suzuki-Miyaura coupling reactions. Catalytic activity under visible-light irradiation was enhanced compared to that under conventional thermal reactions. Our strategy would be a potential tool for the direct utilization of sunlight doe attaining industrially crucial catalytic reactions.

4.5 References

[1] N. S. Lewis, D. G. Nocera, *Proc. Natl. Acad. Sci. USA*, **2006**, 103, 15729.

[2] M. Gratzel, *Nature*, **2001**, 414, 338.

[3] A. Kudo, Y. Miseki, *Chem. Soc. Rev.*, **2009**, 38, 253.

[4] P. D. Tran, V. Artero, M. Fontecave, *Energy Environ. Sci.*, **2010**, 3, 727.

[5] H. Ozawa, K. Sakai, *Chem. Commun.*, **2011**, 47, 2227.

[6] C. D. Windle, R. N. Perutz, *Coord. Chem. Rev.*, **2012**, 256, 2562.

[7] A. Maldotti, A. Molinari, R. Amadelli, *Chem. Rev.*, **2002**, 102, 3811.

[8] A. Inagaki, M. Akita, *Coord. Chem. Rev.*, **2010**, 254, 1220.

[9] M. Osawa, H. Nagai, M. Akita, *Dalton Trans.*, **2007**, 827.

[10] F. Wang, C. Li, H. Chen, R. Jiang, L.-D. Sun, Q. Li, J. Wang, J. C. Yu, C.-H. Yan, *J. Am. Chem. Soc.*, **2013**, 135, 5588.

[11] A. Suzuki, *Angew. Chem., Int. Ed.*, **2011**, 50, 6722.

[12] W. A. Herrmann, K. Öfele, D. v. Preysing, S. K. Schneider, *J. Organomet. Chem.*, **2003**, 687, 229.

[13] D. Benito-Garagorri, K. Kirchner, *Acc. Chem. Res.*, **2008**, 41, 201.

[14] E. Peris, R. H. Crabtree, *Coord. Chem. Rev.*, **2004**, 248, 2239.

[15] N. Miyaura, A. Suzuki, *Chem. Rev.*, **1995**, 95, 2457.

[16] R. Martin, S. L. Buchwald, *Acc. Chem. Res.*, **2008**, 41, 1461.

[17] A. Juris, V. Balzani, F. Barigelletti, S. Campagna, P. Belser, A. von Zelewsky, *Coord. Chem. Rev.*, **1988**, 84, 85.

[18] K. Mori, M. Kawashima, K. Kagohara, H. Yamashita, *J. Phys. Chem. C*, **2008**, 112, 19449.

[19] K. Mori, M. Kawashima, M. Che, H. Yamashita, *Angew. Chem., Int. Ed.*, **2010**, 49, 8598.

[20] Z. Ji, S. D. Huang, A. R. Guadalupe, *Inorg. Chim. Acta*, **2000**, 305, 127.

[21] V. W.-W. Yam, V. W.-M. Lee, K.-K. Cheung, *Organometallics*, **1997**, 16, 2833.

[22] E. Ioachim, E. A. Medlycott, G. S. Hanan, F. Loiseau, V. Ricevuto, S. Campagna, *Inorg. Chem. Commun.*, **2005**, 8, 559.

[23] A. Inagaki, S. Yatsuda, S. Edure, A. Suzuki, T. Takahashi, M. Akita, *Inorg. Chem.*, **2007**, 46, 2432.

[24] K. Murata, M. Ito, A. Inagaki, M. Akita, *Chem. Lett.*, **2010**, *39*, 915.

[25] F. Ozawa, A. Kubo, T. Hayashi, *Chem. Lett.*, **1992**, *21*, 2177.

Chapter V

Catalytic Properties of Iridium and Rhodium Complexes Intercalated into Layered Zirconium Phosphate for H_2 Production under Visible Light

5.1 Introduction

The development of functional inorganic-organic supramolecular materials, the immobilization of suitable guest complexes on solid surfaces has been extensively investigated [1, 2]. Both steric and electrostatic constraints can change the structure and reactivity of the guest complexes, which frequently lead to unexpected physicochemical charactersitics in comparison with their properties in solution [3-10]. Among various inorganic host materials, zirconium phosphate ($Zr(HPO_4)_2{\cdot}H_2O$, α-ZrP) has attracted increasing attention because of its ability to serve as ion-exchanger, solid-state ion conductors, and catalysts [11-13]. α-ZrP has a layered structure, in which zirconium atoms lie nearly in a plane and are bridged by phosphate groups. Three phosphate oxygen atoms are bonded to each zirconium atom and the fourth is bonded to an exchangeable hydrogen atom. The distance of between the layers in α-ZrP is 7.6 Å. The intercalation of large molecules within the interlayer of ZrP can be accomplished by the use of presswelled ZrP phase with enlarged interlayer distances, which have been utilized as a host for luminescent complexes, such as $[Ru(bpy)_3]^{2+}$ [14], $[Pt(tpy)Cl]^+$ [8, 15], and $Re(phen)(CO)_3Cl$ [16]. Although their unique physicochemical properties within the macroheterogeneous environments of ZrP have been reported, the efficient application to the photocatalytic reactions has scarcely been investigated.

In the past decade, the development of a H_2 production system driven by visible light irradiation in an aqueous medium has been desirable in the effort towards environmentally friendly artificial photosynthetic methods [17-19]. A diverse array of heterogeneous systems based on semiconducting metal oxides, exemplified by TiO_2, have been thoroughly investigated for water splitting into H_2 and O_2 since the late 1970s [20], and significant successes have been attained [21-24]. On the other hand, molecular-based photosystem in homogeneous solutions have also been considerately studied for photo-induced H_2 production [25-28]. The molecular-based photocatalytic systems commonly involve the multiple components including a photosensitizer (PS) responsible for the absorption of visible-light, an electron relay (ER) to quench the excited photosensitizer via an electron transfer, a water reduction catalyst (WRC) to produce H_2 and sacrificial reagents (SR) to serve as an electron source. The overall reaction is considered as a visible light-driven proton reduction process by SR to molecular hydrogen via electron relay.

Traditionally, $[Ru(bpy)_3]^{2+}$ (bpy = 2,2'-bipyridine) has been utilized as a PS and methyl viologen (MV^{2+}) has been frequently employed as an ER [29]. In order to remove noxious and expensive MV^{2+} from the reaction mixture, constant efforts have also been devoted to develop organized multinuclear systems comprised a $[Ru(bpy)_3]^{2+}$-derived PS component and a Pt(II)-based H_2-evolving component [28, 30]. Recently, cyclometalated Ir(III) complexes have come under investigation as superior alternatives to Ru sensitizers [31-33]. These exhibit longer excited-state lifetimes compared to the Ru analogues and are capable of direct electron transfer to the reducing species, such as Pt colloids, $[Co(bpy)_3]^{2+}$, and $[Rh(bpy)_3]^{3+}$, with better quantum yields. Unfortunately, such complexes are faced with a number of disadvantages such as thermal instability and difficulties in catalyst separation and recovery.

In this Chapter, we present a new photocatalyst synthesized by intercalation of bis-(2-phenylpyridine)-(2,2'-bipyridine)iridium (III) ($[Ir(ppy)_2(bpy)]PF_6$) complex and tris-2,2'-bipyridyl rhodium(III) ($[Rh(bpy)_3](PF_6)_3$) into ZrP layered material with enlarged interlayer distances by a simple ion-exchange procedure (**Fig. 1**). Ir(III) complexes have attracted recent attention with regard to their application in electrophosphorescent organic light-emitting diodes (OLEDs) [34]. It can be envisioned that the use of such Ir(III) complexes would be promising photosensitizer that effectively promote the electron transfer from ^{3}MLCT state to proton reduction catalysts owing to their extraordinary high luminescence quantum yield (~1) originated from their high ligand field splitting. $[Rh(bpy)_3]^{3+}$ is an ideal candidate for the proton reduction catalyst because it is known to form hydrides and accumulate two electrons at a suitable potential for the H_2 production [35]. It is proven that the intercalation of both Ir and Rh complexes enable H_2 production in aqueous media without an electron mediator by visible-light photosensitization. The relationship between the luminescence characteristics and photocatalytic activities was examined to define the importance of the Ir-Rh combination within the macroheterogeneous environments of ZrP.

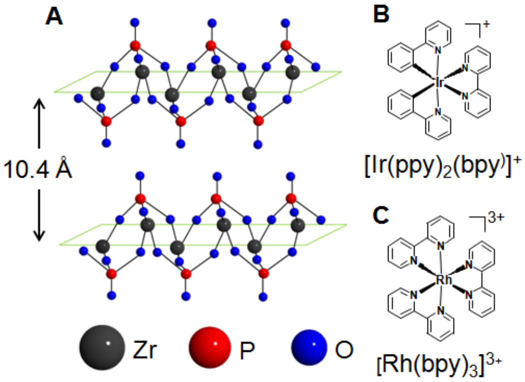

Figure 1. Schematic structure of (**A**) ZrP ($Zr(HPO_4)_2{\cdot}H_2O$) with an enlarged interlayer distance, (**B**) $[Ir(ppy)_2(bpy)]^+$ and (**C**) $[Rh(bpy)_3]^{3+}$.

5.2 Experimental

5.2.1 Materials

$IrCl_3{\cdot}3H_2O$ and $RhCl_3{\cdot}2H_2O$ were purchased from Sigma-Aldrich Co. Inc. 2-Phenylpyridine and 2,2'-bipyridine were obtained from Tokyo Chemical Ind. Co. Ltd. Ammonium hexafluorophosphate was supplied from Wako Pure Chemical Ind., Ltd. $ZrOCl_2{\cdot}8H_2O$ and H_3PO_3 were purchased from Nakalai tesque. Solvents and all commercially available organic compounds for catalytic reactions were purified using standard procedures.

5.2.2 Synthesis of ZrP

0.05 M of $ZrOCl_2{\cdot}8H_2O$ aqueous solution (200 mL) was mixed with 6 M H_3PO_3 aqueous solution at constant stirring at 368 K. after 24 h, the solid was isolated by centrifugation and washed with water with several times, yielding a white crystalline [36].

5.2.3 Synthesis of $[Ir(ppy)_2(bpy)]^+$ and $[Rh(bpy)_3]^{3+}$-intercalated ZrP

$[Ir(ppy)_2(bpy)]PF_6$ [37] and $[Rh(bpy)_3](PF_6)_3$ [38] were synthesized according to the literature procedure. A 50 mL of acetonitrile solution of $[Ir(ppy)_2(bpy)]PF_6$ (43.0 mg), and $[Rh(bpy)_3](PF_6)_3$ (54.6 mg) was added to 150 mL of aqueous suspension containing the ZrP (1.0 g), and the resultant mixture was stirred at 343 K for 96 h. The mixture was filtered and the solid obtained was washed repeatedly with distilled water/acetonitrile and dried overnight, giving a Ir-Rh/ZrP (Ir : Rh = 1 : 1). Other samples with different metal loadings were also prepared by varying the initial concentration.

The metal loadings were determined by inductively coupled plasma (ICP) analysis.

5.2.4 Characterization

Powder X-ray diffraction patterns were recorded using a Rigaku Ultima IV diffractometer with Cu Kα radiation (λ = 1.5406 Å). BET surface area measurements were performed using a BEL-SORP max (Bel Japan, Inc.) instrument at 77 K. The sample was degassed in vacuum at 353 K for 24 h prior to data collection. UV-vis diffuse reflectance spectra of powdered samples were collected using a Shimadzu UV-2450 spectrophotometer. The reference was $BaSO_4$, and the absorption spectra were obtained using the Kubelka-Munk function. Inductively coupled plasma optical emission spectrometry (ICP-OES) measurements were performed using a Nippon Jarrell-Ash ICAP-575 Mark II instrument. Photoluminescence measurements were carried out on a fluorolog-3 spectrofluorometer (Horiba). Ir L_{III}-edge and Rh K-edge XAFS spectra were recorded using a fluorescence-yield collection technique at the beam line 01B1 station with an attached Si (311) monochromator at SPring-8, JASRI, Harima, Japan (prop. No. 2012A1061 and 2012B1058). The EXAFS data were normalized by fitting the background absorption coefficient, around the energy region higher than that of the edge of about 35-50 eV, with smooth absorption of an isolated atom. The EXAFS data were examined using the Rigaku EXAFS analysis program. Fourier transformation (FT) of k^3-weighted normalized EXAFS data was performed over the $3.5\ Å < k/Å^{-1} < 11\ Å$ range to obtain the radial structure function.

5.2.5 Photocatalytic H_2 Production

The powdered Ir-Rh/ZrP catalyst (50 mg), 10 ml of 90% H_2O-acetonitrile solution, and triethylamine (TEA, 0.6 mL) were introduced into a reaction vessel (30 mL) which was then sealed with a rubber septum. The resulting mixture was bubbled with Ar for 15 min in dark conditions. Subsequently, the sample was irradiated from the side using a Xe lamp (500 W; SAN-EI ERECTRIC CO., Ltd. XEF-501S) through the glass filter (λ > 420 nm) with magnetic stirring at ambient pressure and temperature. The reaction progress was monitored using a Shimadzu GC-14B instrument equipped with MS5A columns.

5.3 Results and Discussion

5.3.1 Characterization of [Ir(ppy)$_2$(bpy)]$^+$ and [Rh(bpy)$_3$]$^{3+}$-intercalated ZrP

Samples of Ir and Rh complexes-intercalated ZrP (Ir-Rh/ZrP) were obtained by stirring a suspension of ZrP in an H_2O : acetonitrile = 3 : 1 solution containing both Ir and Rh complexes for 4 days under reflux conditions. As a result, Ir-Rh/ZrP samples with different molar ratios (Ir : Rh = 1 : 0, 1.5 : 0.15, 1.2 : 0.3, 1.2 : 0.6, 1 : 1, 0.6 : 1.2, 0 : 1, molar ratio 1 corresponds to 0.05 mmol/g) were obtained. The Ir and Rh contents were measured by ICP analysis.

Fig. 2 shows the XRD patterns of the original ZrP and Ir-Rh/ZrP samples. We employed a hydrated form of ZrP with six water molecules per formula unit, which possess an interlayer distance of 10.3 Å. This phase was first observed by Clearfield et al. [39], and characterized by Alberti et al. [40] and Kijima developed a synthetic procedure [36]. The diffraction patterns were measured in the wet sample to avoid dehydration of the materials. As confirmed in the XRD pattern, the interlayer space of our synthesized ZrP sample was determined to be 10.3 Å according to the first order diffraction peak due to (002) plane. The diffraction patterns of the Ir-Rh/ZrP samples show the appearance of a small peak at around 2θ = 5.7 corresponding to new phase with an expanded interlayer distance of ca. 15.5 Å, which is apparent evidence for the intercalation of metal complexes

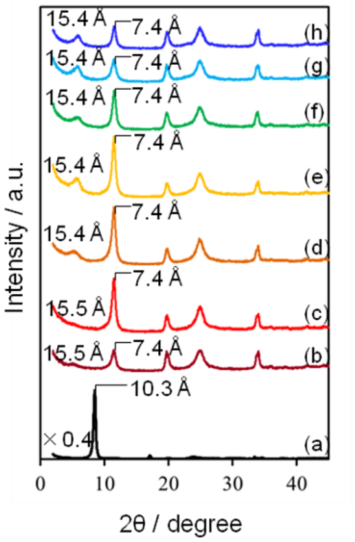

Figure 2. XRD patterns of (a) α-ZrP (b) Ir/ZrP (Ir : Rh = 1 : 0), (c) Ir-Rh/ZrP (Ir : Rh = 1.5 : 0.15), (d) Ir-Rh/ZrP (Ir : Rh = 1.2 : 0.3), (e) Ir-Rh/ZrP (Ir : Rh = 1.2 : 0.6), (f) Ir-Rh/ZrP (Ir : Rh = 1 : 1), (g) Ir-Rh/ZrP (Ir : Rh = 0.6 : 1.2), and (h) Rh/ZrP (Ir : Rh = 0 : 1).

within the interlayer ZrP. An additional peak can be observed at around $2\theta = 11.5^\circ$, which corresponds to dehydrated α-ZrP phase with an interlayer distance of 7.4 Å. These results suggest that the intercalation of metal complex leads to a layer separation into the expanded interlayer containing metal complexes and shrunk interlayer without any intercalated guest molecules.

N_2 adsorption/desorption isotherms of the original ZrP and Ir-Rh/ZrP (Ir : Rh = 1 : 1) samples are type III without a significant hysteresis loop (**Fig. 3**). The Brunauer-Emmett-Teller (BET) surface area (S_{BET}) and pore volume (V_p) calculated from N_2 adsorption-desorption were 41 $m^2 \cdot g^{-1}$ and 0.19 $cm^3 \cdot g^{-1}$ and 42 $m^2 \cdot g^{-1}$ and 0.22 $cm^3 \cdot g^{-1}$ for the original ZrP and Ir-Rh/ZrP, respectively. These results suggest that the ZrP keeps its original surface area even after the intercalation of metal complexes, which probably because the appearance of new phase with an expanded interlayer distance of ca. 15.5 Å.

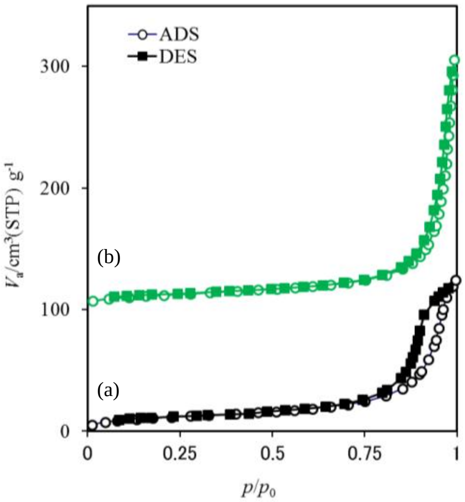

Figure 3. N_2 adsorption-desorption isotherm of (a) ZrP and (b) Ir-Rh/ZrP (Ir : Rh = 1 : 1).

As shown in **Fig. 4A**, the UV-vis spectrum of the $[Ir(ppy)_2(bpy)]^+$ in acetonitrile solution exhibits intense absorption bands in the high energy region ($\lambda < 300$ nm) assigned to the spin-allowed singlet ligand-centered transition for ppy and bpy ligands (^{1}LC, π-π*), and moderate low-energy bands ranging from 350 to 400 nm ascribed to the spin-allowed singlet MLCT transition, and weaker absorption tails ranging to 500 nm are attributed to a mixture of spin-forbidden ^{3}LC and ^{3}MLCT transitions [41]. The spectrum of the $[Rh(bpy)_3]^{3+}$ in acetonitrile solution exhibits absorption

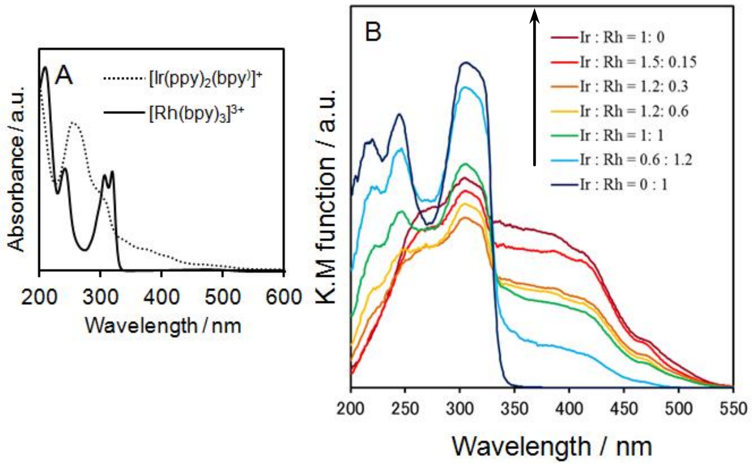

Figure 4. UV-vis spectra of (A) $[Ir(ppy)_2(bpy)]^+$ and $[Rh(bpy)_3]^{3+}$ solutions in acetonitrile (B) ZrP and Ir-Rh/ZrP samples with different Ir/Rh molar ratios.

assigned to ^{1}LC transition for bpy ligands at around 300 nm, while no absorption is observed in the visible region. The spectrum of Ir-Rh/ZrP contains both absorptions due to free Ir and Rh complexes, suggesting that both complexes can easily diffuse into interlayer space (**Fig. 4B**). Apparently, the absorption intensity in the visible region ($\lambda > 400$ nm) increased with increasing the amount of Ir complexes.

Fig. 5A shows normalized X-ray absorption near-edge structure (XANES) spectra at the Ir L_{III}-edge of the $[Ir(ppy)_2(bpy)]^+$ complex and Ir-Rh/ZrP (Ir : Rh = 1 : 1 and 1 : 0). The white line at around 11222 eV assigned to the allowed 2p → nd transition is intensified with an increase in the *d*-band vacancies as a result of oxidation [7, 42]. Thus, the white line absorption peaks of oxidized Ir species are more intense than those of reduced species. The intensity of the intercalated Ir complex is almost in agreement with the free complex. In the Fourier transforms (FT) of the Ir L_{III}-edge X-ray absorption fine structure (EXAFS) spectra (**Fig. 5B**), a strong peak is observed at around 1.5 Å attributable to Ir-N and/or Ir-C bond in addition to a small second shell at ca. 2.4 Å, which is assigned to neighboring carbon atoms. This verifies a tridentate binding structure for Ir(III) center in octahedral coordination.

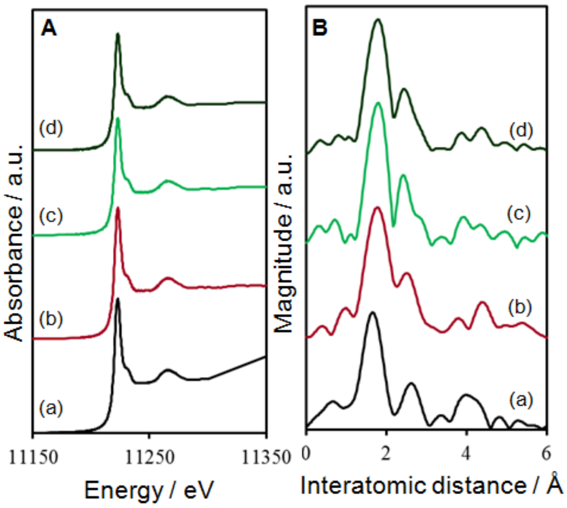

Figure 5. (**A**) Ir L_{III}-edge XANES spectra and (**B**) FT-EXAFS spectra of (a) $[Ir(ppy)_2(bpy)]^+$, (b) Ir/ZrP (Ir : Rh = 1 : 0), (c) Ir-Rh/ZrP (Ir : Rh = 1 : 1), and (d) recovered Ir-Rh/α-ZrP (Ir : Rh = 1 : 1).

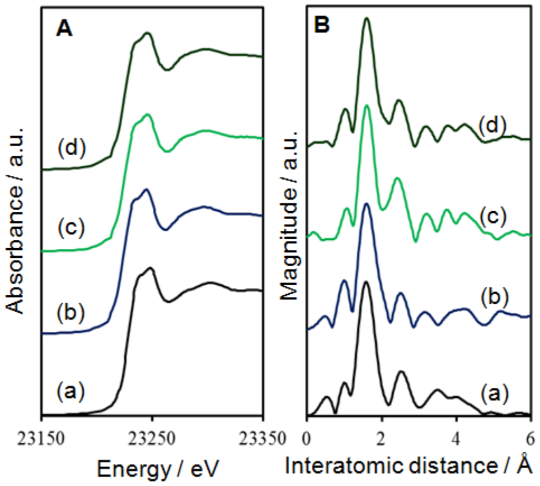

Figure 6. (**A**) Rh K-edge XANES spectra and (**B**) FT-EXAFS spectra of (a) $[Rh(bpy)_3]^{3+}$, (b) Rh/ZrP (Ir : Rh = 0 : 1), (c) Ir-Rh/ZrP (Ir : Rh = 1 : 1), and (d) recovered Ir-Rh/α-ZrP (Ir : Rh = 1 : 1).

Fig. 6 shows XANES and FT-EXAFS spectra at the Rh K-edge of the $[Rh(bpy)_3]^{3+}$ complex and Ir-Rh/ZrP (Ir : Rh = 1 : 1 and 0 : 1) samples. The Rh K-edge XANES spectra were quite similar to that observed for the free $[Rh(bpy)_3]^{3+}$. FT-EXAFS showed a strong peak at around 1.5 Å attributable to a Ru-N bond and a small second shell at ~2.5 Å assigned to neighboring carbon atoms, together confirming a bidentate binding structure in the Rh(II) oxidation state. All XAFS data reveal that the intercalated metal complexes within macroheterogeneous environments keep their original structures despite of the presence of neighboring complexes.

The emission spectra are dependent on the ligand field strength, the redox properties of the metal and ligands, and the inherent properties of the ligands [43]. Therefore, a small change in the surroundings of the Ir complex significantly influences the orbital nature of the excited state. **Fig. 7A** shows the photoluminescence spectra of the $[Ir(ppy)_2(bpy)]^+$ complex in acetonitrile solution upon excitation at 370 nm. The $[Ir(ppy)_2(bpy)]^+$ complex exhibits emission at around 585 nm at room temperature, which is mainly attributable to the ^{3}MLCT transition [44]. At 77 K, the luminescence was maximized near 570 nm, which is mainly attributed to the ^{3}LC level in a higher triplet state rather than ^{3}MLCT. This significant blue shift can be simply explained by the efficient quenching of the thermally activated deactivation processes at 77 K, so that luminescence from ^{3}LC levels can parenthetically occur [44, 45]. The asymmetry of the emission bands at 77 K reveals the skewing of the emission maximum toward shorter wavelength. This behavior is originated from the poorly resolved vibronic structure and is similar to that of Pt(II) polypyridyl complexes [46].

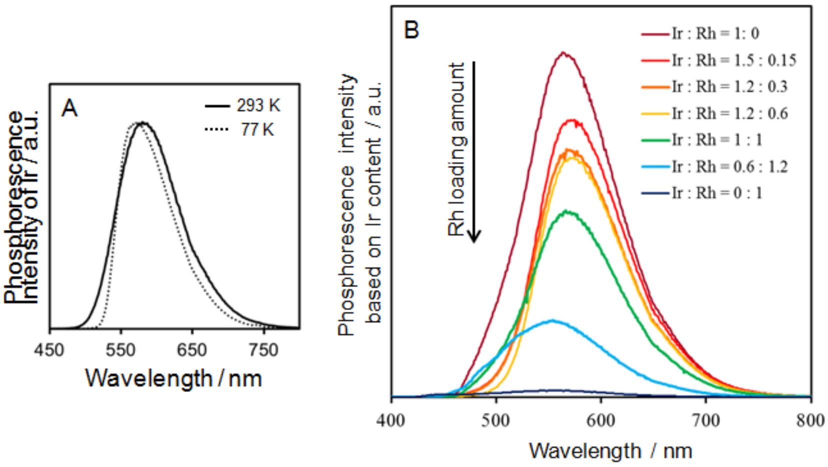

Figure 7. Photoluminescence spectra of (A) $[Ir(ppy)_2(bpy)]^+$ in acetonitrile solution at room temperature and 77K (λ_{ex} = 370 nm), and (B) Ir-Rh/ZrP with different Ir/Rh molar ratios at room temperature (λ_{ex} = 370 nm).

The tendency is different for ZrP, where phosphorescence emission of the powdered sample is blue shifted relative to that of the free complex in acetonitrile at room temperature and maximized near 560-565 nm (**Fig. 7B**). Moreover, the shift toward shorter wavelength was negligible (~ 2 nm) upon changing from room temperature to 77 K (data not shown). No significant emission due to the $[Rh(bpy)_3]^{3+}$ was observed in this wavelength region. It is likely that the vibrational relaxation of the triplet MLCT excited states in the Ir-Rh/ZrP is probably inhibited by the unique surroundings within interlayer spaces. Thus phosphorescence emission from higher ^{3}LC state mainly occur receiving substantial contribution from close lying ^{3}MLCT levels, and resulted in a blue shift of the emission spectra. This is so-called “rigidchromism” that was originally termed by Wringhton and Morse [47]. Analogous phenomena have also been observed for the $[Ir(ppy)_2(bpy)]^+$ complex intercalated in the layered silicate materials [48]. It is notable that the peak intensity is maximum with Ir/ZrP without Rh complex and increase of the Rh loading resulted in a substantial decrease in emission intensity. This result indicated that both Ir and Rh complexes within the interlayer spaces exist in a short separation that enables cooperative action with adjacent complexes, and the excited state of Ir complex may undergo the efficient oxidative quenching by the Rh complex following the eq. 1 [32].

$$[Ir(ppy)_2(bpy)]^{+*} + [Rh(bpy)_3]^{3+} \rightarrow [Ir(ppy)_2(bpy)]^{2+} + [Rh(bpy)_3]^{2+} \quad (1)$$

5.3.2 Photocatalytic H_2 Production of $[Ir(ppy)_2(bpy)]^+$ and $[Rh(bpy)_3]^{3+}$-intercalated ZrP

The potential photocatalytic activity of the Ir-Rh/ZrP for H_2 production was evaluated by visible-light irradiation ($\lambda > 420$ nm) in 90% H_2O-acetonitrile solution. **Fig. 8** shows the time course of the H_2 production using various sacrificial reagents. TEA was found to be the most effective one among those investigated. The use of MeOH, EtOH, HCOOH, and CH_3COOH instead of TEA resulted in no activity. The present Ir-Rh system has an even greater influence on photocatalytic activities than the conventional Ru-based system because Ir-Rh system contain a reductive quenching step of excited-state photosensitizer Ir complex by the sacrificial reagent, as will be mentioned later. No reaction is observed under either dark condition in the presence of the photocatalyst or without TEA under light irradiation. Moreover, H_2 production does not occur to any significant extent in the presence of ZrP without metal complexes under identical reaction conditions. The catalytic activity of Ir-Rh/ZrP was higher than that of the homogeneous counterparts by a factor of 5 under such aqueous conditions. In our preliminary experiment, the XAFS spectrum of the recovered Ir-Rh/ZrP after the photocatalytic reaction is identical to that of the fresh catalyst, indicating no changes in the electronic configuration and local structures **(Fig. 5d, 6d)**.

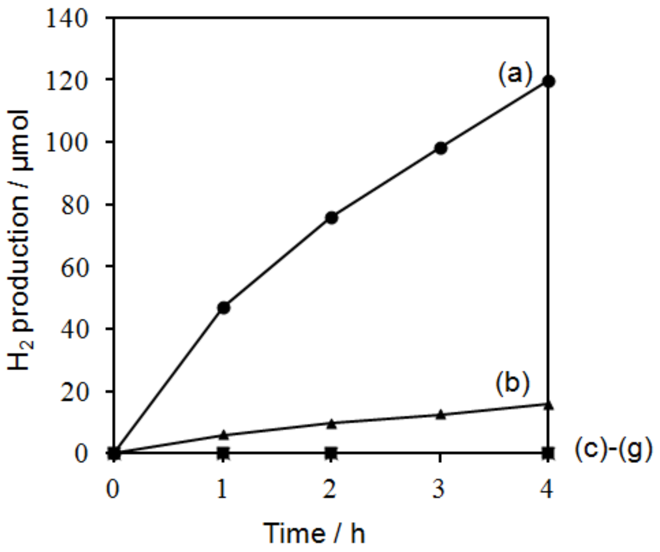

Figure 8. Photocatalytic H_2 production in 90% H_2O-acetonitrile with 0.6 M electron donors ; (a) TEA, (b) TEOA, (c) EDTA, (d) MeOH, (e) EtOH, (f) HCOOH, and (g) CH_3COOH using Ir-Rh/ZrP (Ir : Rh = 1 : 1).

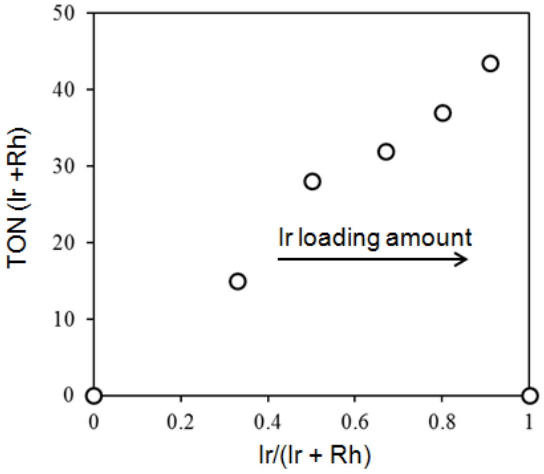

Figure 9. Effect of Ir and Rh molar ratio in the Ir-Rh/ZrP for photocatalytic H_2 production (λ_{ex} > 420 nm).

The influence of molar ratio of photosensitizer Ir complex and proton reduction catalyst Rh complex within the ZrP was also explored, as shown in **Fig. 9**. Both Ir and Rh complexes were indispensable to achieve efficient H_2 production; no reaction occurred in the absence of either Ir or Rh complex. Maximal turnover number (TON) was obtained at Ir/(Ir +Rh) = 0.91 corresponding to Ir : Rh = 10 : 1, in which TON based on Rh was 478. In simple terms, this reaction is facilitated by the direct electron transfter from photosensitizer Ir complex to proton reduction catalyst Rh complex without an electron mediator. It has been reported that the sensitizer to catalyst optimal ratio was found to be 3 : 1 in homogeneous solution, indicating that the electron transfer efficiency in solution is different from that in interlayer space of ZrP.

Vide supra, the classical molecule-based photocatalytic H_2 production system consists of multi-components including PS ($Ru(bpy)_3^{2+}$), ER (methylviologen) and WRC (colloidal Pt) and SR (EDTA). The electron relay step is generally important to complete a photocatalytic cycle; an efficient ER oxidatively quenches the excited PS, thereby allowing charge separation at the expense of simplicity. It is noteworthy that the present photocatalyst capable of visible-light photosensitization associated with the ^{3}LC and ^{3}MLCT excited states of Ir complex and hydrogenic activation of Rh complex to produce H_2 without an electron relay. Firstly, an excited state of the $[Ir(ppy)_2(bpy)]^{+*}$ is reductively quenched by TEA (SR) to produce an $[Ir(ppy)_2(bpy)]^0$ (eq.2). Secondly, the activated reduced Ir^0 species directly deliver reducing equivalents to Rh WRC (eq.3), and finally produce H_2 via a reductive elimination from Rh dihydride species in a homolytic unimolecular pathway (eq.4).

$$[Ir(ppy)_2(bpy)]^{+*} + TEA \quad \rightarrow \quad [Ir(ppy)_2(bpy)]^0 + TEA^+ \qquad (2)$$

$$2[Ir(ppy)_2(bpy)]^0 + [Rh(bpy)_x]^{n+} \rightarrow 2[Ir(ppy)_2(bpy)]^+ + [Rh(bpy)_x]^{(n-2)+} \qquad (3)$$

$$[Rh(bpy)_x]^{(n-2)+} + 2H^+ \quad \rightarrow \quad [Rh(bpy)_x]^{n+} + H_2 \qquad (4)$$

5.4 Conclusion

Intercalation of photosensitizer iridium(III) and proton reduction catalyst rhodium(III) complexes within an interlayer space of expanded ZrP affords a new type of photocatalyst with photoluminescence properties as well as photocatalytic activities. Photoluminescence emission due to the Ir complex of the Ir-Rh/ZrP was blue shifted relative to that of the free complex in acetonitrile at room temperature because of the rigidchromism effect. The excited state of Ir complex within the macroheterogeneous environments undergoes the oxidative quenching by the neighboring Rh complex, thus the peak intensity decreased with increasing the Rh loading. The Ir-Rh/ZrP catalyst exhibits both visible-light sensitization and water splitting in aqueous solution in the absence of mediator.

5.5 References

[1] W. J. Roth, J. Cejka, *Catal. Sci. Technol.*, **2011**, 1, 43.

[2] Y. Tao, H. Kanoh, L. Abrams, K. Kaneko, *Chem. Rev.*, **2006**, 106, 896.

[3] K. Mori, M. Kawashima, K. Kagohara, H. Yamashita, *J. Phys. Chem. C*, **2008**, 112, 19449.

[4] K. Mori, K. Kagohara, H. Yamashita, *J. Phys. Chem. C*, **2008**, 112, 2593.

[5] K. Mori, M. Kawashima, M. Che, H. Yamashita, *Angew. Chem. Inter. Ed.*, **2010**, 49, 8598.

[6] K. Mori, K. Watanabe, M. Kawashima, M. Che, H. Yamashita, *J. Phys. Chem. C*, **2010**, 115, 1044.

[7] K. Mori, M. Tottori, K. Watanabe, M. Che, H. Yamashita, *J. Phys. Chem. C*, **2011**, 115, 21358.

[8] K. Mori, S. Ogawa, M. Martis, H. Yamashita, *J. Phys. Chem. C*, **2012**, 116, 18873.

[9] K. Mori, K. Watanabe, K. Fuku, H. Yamashita, *Chem. Eur. J.*, **2012**, 18, 415.

[10] K. Mori, K. Watanabe, Y. Terai, Y. Fujiwara, H. Yamashita, *Chem. Eur. J.*, **2012**, 18, 11371.

[11] G. Alberti, *Acc. Chem. Res.*, **1978**, 11, 163.

[12] A. Clearfield, *in Prog. Inorg. Chem., John Wiley & Sons, Inc.*, **2007**, pp. 371.

[13] A. Clearfield, *Chem. Rev.*, **1988**, 88, 125.

[14] A. A. Martí, J. L. Colón, *Inorg. Chem.*, **2003**, 42, 2830.

[15] E. J. Rivera, C. Figueroa, J. L. Colón, L. Grove, W. B. Connick, *Inorg. Chem.*, **2007**, 46, 8569.

[16] A. A. Marti, N. Rivera, K. Soto, L. Maldonado, J. L. Colon, *Dalton Trans.*, **2007**, 1713.

[17] M. Graetzel, *Acc. Chem. Res.*, **1981**, 14, 376.

[18] N. S. Lewis, D. G. Nocera, *Proc. Natl. Acad. of Sci.*, **2006**, 103, 15729.

[19] A. J. Esswein, D. G. Nocera, *Chem. Rev.*, **2007**, 107, 4022.

[20] A. Fujishima, K. Honda, *Nature*, **1972**, 238, 37.

[21] M. Gratzel, *Nature*, **2001**, 414, 338.

[22] H. Arakawa, K. Sayama, *Catal. Surv. Jap.*, **2000**, 4, 75.

[23] K. Maeda, K. Domen, *J. Phys. Chem. C*, **2007**, 111, 7851.

[24] A. Kudo, Y. Miseki, *Chem. Soc. Rev.*, **2009**, 38, 253.

[25] L. L. Tinker, N. D. McDaniel, S. Bernhard, *J. Mater. Chem.*, **2009**, 19, 3328.

[26] M. Wang, Y. Na, M. Gorlov, L. Sun, *Dalton Trans.*, **2009**, 33, 6458.

[27] P. D. Tran, V. Artero, M. Fontecave, *Energy Environ. Sci.*, **2010**, 3, 727.

[28] H. Ozawa, K. Sakai, *Chem. Commun.*, **2011**, 47, 2227.

[29] A. Moradpour, E. Amouyal, P. Keller, H. Kagan, *Nouv. J. Chim.*, **1978**, 2, 547.

[30] H. Ozawa, M.-a. Haga, K. Sakai, *J. Am. Chem. Soc.*, **2006**, 128, 4926.

[31] L. L. Tinker, N. D. McDaniel, P. N. Curtin, C. K. Smith, M. J. Ireland, S. Bernhard, *Chem. Eur. J.*, **2007**, 13, 8726.

[32] E. D. Cline, S. E. Adamson, S. Bernhard, *Inorg. Chem.*, **2008**, 47, 10378.

[33] Y.-J. Yuan, J.-Y. Zhang, Z.-T. Yu, J.-Y. Feng, W.-J. Luo, J.-H. Ye, Z.-G. Zou, *Inorg. Chem.*, **2012**, 51, 4123.

[34] C. Ulbricht, B. Beyer, C. Friebe, A. Winter, U. S. Schubert, *Adv. Mater.*, **2009**, 21, 4418.

[35] N. Sutin, C. Creutz, E. Fujita, *Comments Inorg. Chem.*, **1997**, 19, 67.

[36] T. Kijima, *Bull. Chem. Soc. Jap.*, **1982**, 55, 3031.

[37] M. S. Lowry, J. I. Goldsmith, J. D. Slinker, R. Rohl, R. A. Pascal, G. G. Malliaras, S. Bernhard, *Chem. Mater.*, **2005**, 17, 5712.

[38] J. E. Hillis, M. K. DeArmond, *J. Luminescence*, **1971**, 4, 273.

[39] A. Clearfield, W. L. Duax, A. S. Medina, G. D. Smith, J. R. Thomas, *J. Phys. Chem.*, **1969**, 73, 3424.

[40] G. Alberti, U. Costantino, J. S. Gill, J. Inorg. *Nucl. Chem.*, **1976**, 38, 1733.

[41] M. G. Colombo, A. Hauser, H. U. Guedel, *Inorg. Chem.*, **1993**, 32, 3088.

[42] P. I. Ravikovitch, A. V. Neimark, *Langmuir*, **2000**, 16, 2419.

[43] S. I. Gorelsky, E. S. Dodsworth, A. B. P. Lever, A. A. Vlcek, *Coord. Chem. Rev.*, **1998**, 174, 469.

[44] S.-H. Wu, J.-W. Ling, S.-H. Lai, M.-J. Huang, C. H. Cheng, I. C. Chen, *J. Phys. Chem. A*,

2010, 114, 10339.

[45] Y. Ohsawa, S. Sprouse, K. A. King, M. K. DeArmond, K. W. Hanck, R. J. Watts, *J. Phys. Chem.*, **1987**, 91, 1047.

[46] K. Wang, M.-a. Haga, H. Monjushiro, M. Akiba, Y. Sasaki, *Inorg. Chem.*, **2000**, 39, 4022.

[47] M. Wrighton, D. L. Morse, *J. Am. Chem. Soc.*, **1974**, 96, 998.

[48] D. Mochizuki, M. Sugiyama, M. M. Maitani, Y. Wada, *Eur. J. Inorg. Chem.*, **2013**, 13, 2324.

Chapter VI

Visible-Light-Induced Hydrogen Evolution with Iridium and Rhodium Complexes Immobilized Layered $K_4Nb_6O_{17}$ as an Electron Mediator Free Heterogeneous Photocatalyst

6.1 Introduction

Much effort has gone into production of H_2 by visible light irradiation of aqueous media in order to achieve environmentally artificial photosynthesis [1-3]. Since the late 1970s, a variety of heterogeneous systems based on semiconducting metal oxides such as TiO_2 have been explored for splitting water into H_2 and O_2 [4], and successful applications including visible-light photocatalysts have been reported [5-8]. Metal complex photosystems in homogeneous solutions have also been actively explored for visible-light-driven H_2 production [9-12]. Photocatalytic systems based on metal complexes generally involve multiple components, including a photosensitizer (PS), which is responsible for visible light absorption, an electron relay (ER), which quenches the excited photosensitizer (PS*) through an electron transfer, a water reduction catalyst (WRC) to generate H_2, and sacrificial reagents (SR) to provide the electrons for replenishing the lowest singly occupied molecular orbital of the PS^+. The visible-light-induced proton reduction process producing molecular hydrogen via electron relay is depicted in **Scheme 1**.

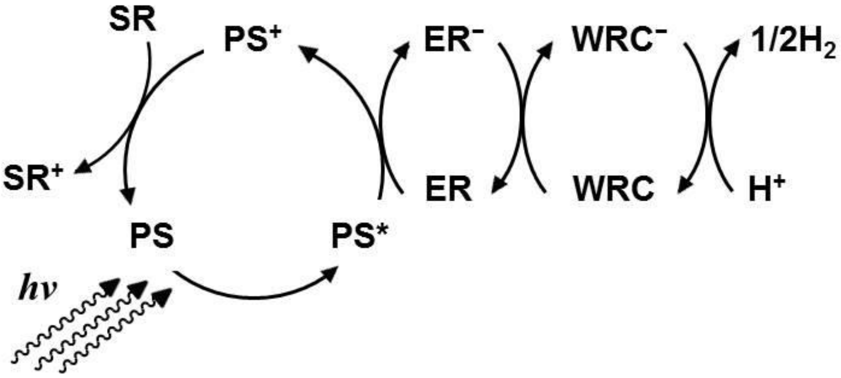

Scheme 1. Photochemical H_2 evolution by classical three-component system.

$[Ru(bpy)_3]^{2+}$ (bpy = 2,2'-bipyridine) has been commonly employed as a PS, and methyl viologen (MV^{2+}) has been frequently used as an ER [13]. For removing the toxic and expensive MV^{2+} from the system, efforts have been devoted to construct organized multinuclear systems using a $[Ru(bpy)_3]^{2+}$-derived PS component and a Pt(II)-based H_2-evolving component [12-14]. More recently, cyclometalated Ir(III) complexes have been used as the PS [15-17]. These complexes have longer excited-state lifetimes compared with analogous Ru complexes, and they can directly transfer electrons to the reducing species such as Pt colloids, $[Co(bpy)_3]^{2+}$, and $[Rh(bpy)_3]^{3+}$ with better quantum yields without an electron relay. However, utilization of these metal complexes on an industrial scale has practical complications because large amounts of organic solvents are required. Moreover for H_2 production in homogeneous media, it is difficult to recover the expensive transition metals and ligands after separating the products.

Nanostructural porous inorganic materials such as two-dimensional clays, zeolites, and mesoporous materials have practical potential for use in heterogeneous catalysis, adsorption, and ion exchange [18, 19]. In order to construct functional supramolecular materials, integration of metal complexes with these rigid structured host materials have also been intensively investigated [20-26]. These inorganic-organic materials often exhibit unanticipated physicochemical properties because of steric and electrostatic constraints within the confined interlayer spaces. However, $K_4Nb_6O_{17}$ is promising as it possesses a unique layered structure with two different alternately stacked interlayers I and II [27]. The charge of the anionic sheet formed by octahedral NbO_6 units via bridging oxygen atoms is balanced by K^+ between the layers (**Fig. 1A**). $K_4Nb_6O_{17}$ as support also has a photoactive nature. Thus, it can be expected that intercalation of metal complexes in $K_4Nb_6O_{17}$ may have novel photofunctions because of electronic and energetic host-guest interactions. To date, synthesis of hybrid materials of layered $K_4Nb_6O_{17}$ with MV^{2+} [28], porphyrin [29], and $[Ru(bpy)_3]Cl_2$ [30] have been successful, and these materials show interesting photochemical properties.

In this Chapter, we present a new photocatalyst created by a simple ion exchange with bis-(2-

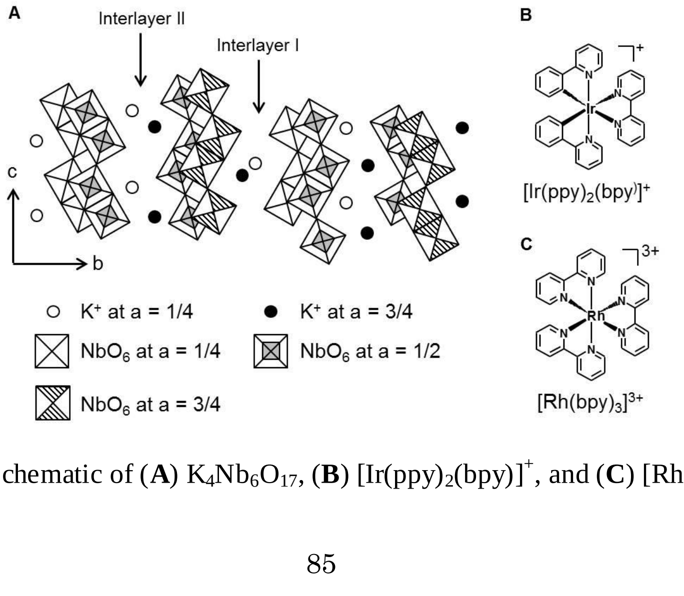

Figure 1. Schematic of (**A**) $K_4Nb_6O_{17}$, (**B**) $[Ir(ppy)_2(bpy)]^+$, and (**C**) $[Rh(bpy)_3]^{3+}$.

phenylpyridine)-(2,2’-bipyridine)iridium(III) ($[Ir(ppy)_2(bpy)]^+$) and tris(2,2’-bipyridyl)rhodium(III) ($[Rh(bpy)_3]^{3+}$) to $K_4Nb_6O_{17}$ possessing strongly acidity (**Fig. 1B, C**). Ir(III) complexes have been extensively studied for application in electrophosphorescent organic light-emitting diodes [31]; therefore, we postulate that Ir(III) complexes might be a PS that could successfully promote electron transfer from the triplet metal-to-ligand charge transfer (^{3}MLCT) state to the WRCs. Electron transfer between Ir and Rh occur with a probability represented wave function even if the distance of both complexes is separated. These complexes have high luminescence quantum yields (~1) originating from their high ligand field splitting. $[Rh(bpy)_3]^{3+}$ is an ideal catalyst for proton reduction because it keeps two electrons at a suitable potential for H_2 production and is known to form hydrides [32]. The combination of Ir and Rh complexes in aqueous media could enable visible-light-driven H_2 production without an electron relay. We also attempted intercalation into an exfoliated $K_4Nb_6O_{17}$ nanosheet in an effort to achieve enhanced photocatalytic activity.

6.2 Experimental

6.2.1 Materials

$IrCl_3 \cdot 3H_2O$ and $RhCl_3 \cdot 2H_2O$ were purchased from Sigma-Aldrich Co. Inc. 2-Phenylpyridine and 2,2’-bipyridine were obtained from Tokyo Chemical Ind. Co. Ltd. Ammonium hexafluorophosphate, K_2CO_3 and Nb_2O_5 were supplied from Wako Pure Chemical Ind., Ltd. Solvents and all commercially available organic compounds for catalytic reactions were purified using standard procedures.

6.2.2 Synthesis of $[Ir(ppy)_2(bpy)]PF_6$

A mixture of 2-phenylpyridine (5.3 mmol) and $IrCl_3 \cdot 3H_2O$ (2.1 mmol) in a methoxyethanol : water (3 : 1) solution was stirred under reflux conditions (393 K) with constant stirring for 15 h under Ar atmosphere. The resulting precipitate was collected by suction filtration, washed with water and diethyl ether, and dried to yield the product, $[(C\^{}N)_2Ir\text{-}\mu\text{-}Cl]_2$. The obtained dichloro-bridged dimer (0.9 mmol) was reacted with 2,2’-bipyridine (1.9 mmol) in ethylene glycol (50 mL) under reflux (423 K) with constant stirring for 15 h. Upon cooling to room temperature, the mixture was transferred to a separatory funnel with water and washed with diethyl ether. The aqueous layer was heated using a heat gun to remove residual organic solvents. The vessel was then placed on ice, and 10 mL of aqueous ammonium hexafluorophosphate solution (5.0 g in 20 mL of deionized water) was slowly added to the reaction mixture, yielding a yellow precipitate [33].

6.2.3 Synthesis of $[Rh(bpy)_3](PF_6)_3$

$RhCl_3 \cdot 2H_2O$ (2.0 mmol) and 2,2'-bipyridine (7.0 mmol) were added to EtOH (20 mL) and H_2O (20 mL), and the mixture was heated at 353 K with stirring. After 15 min, 2.0 mL of 1 M hydrazine in EtOH/H_2O was added and heating was continued for an additional 1 h. Following counterion metathesis with NH_4PF_6 (1.0 g in H_2O), the reaction mixture was concentrated to 10 mL by evaporation. The solids were isolated by filtration, washed with water and diethyl ether, and dried overnight, yielding white crystals [34].

6.2.4 Synthesis of $K_4Nb_6O_{17}$

$K_4Nb_6O_{17}$ was prepared by calcination of a stoichiometric mixture of K_2CO_3 (0.5 g) and Nb_2O_5 (1.5 g) crushed by a ball mill (600 rpm for 10 min). The mixture was calcinated at 1323 K in air for 2 h [35].

6.2.5 Synthesis of $K_4Nb_6O_{17}$ Nanosheet

$K_4Nb_6O_{17}$ (3.0 g) was added to 250 ml of 2 M nitric acid, and the resultant mixture was stirred at room temperature for 48 h. The mixture was filtered and washed repeatedly with distilled water and dried. This whole process was repeated two times to exchange protons sufficiently. The sample was then dispersed in distilled water with pH (9.5-10) adjusted by $(C_4H_9)_4NH_4(OH)$. The resultant mixture was stirred at room temperature for 24 h and centrifuged. 0.5 M nitric acid was added to agglutinate the colloidal solution into a nanosheet by strongly stirring, yielding a white precipitate. After centrifugation, the obtained solids were washed with nitric acid and distilled water and dried overnight, giving $K_4Nb_6O_{17}$ nanosheets [36].

6.2.6 Synthesis of $[Ir(ppy)_2(bpy)]^+$ and $[Rh(bpy)_3]^{3+}$-intercalated $K_4Nb_6O_{17}$

10 ml of an acetonitrile solution of $[Ir(ppy)_2(bpy)]PF_6$ (21.5 mg), and $[Rh(bpy)_3](PF_6)_3$ (27.3 mg) was added to 90 ml of an aqueous suspension containing $K_4Nb_6O_{17}$ (0.5 g), and the resultant mixture was stirred at 343 K for 4 days. The mixture was filtered, and the obtained solid was washed

repeatedly with distilled water and dried overnight, giving Ir-Rh/$K_4Nb_6O_{17}$ (Ir : Rh = 1 : 1) [37]. Other samples with different metal loadings were prepared by varying the initial concentrations of the Ir and Rh complexes. The metal loadings were determined by inductively coupled plasma (ICP) analysis.

6.2.7 Characterization

S_{BET} measurements were performed using a BELSORP-max (Bel Japan, Inc.) instrument at 77 K. The sample was degassed in vacuum at 353 K for 24 h prior to data collection. UV-Vis diffuse reflectance spectra of powdered samples were collected using a Shimadzu UV-2450 spectrophotometer. The reference was $BaSO_4$, and the absorption spectra were obtained using the Kubelka-Munk function. Inductively coupled plasma optical emission spectrometry (ICP-OES) measurements were performed using a Nippon Jarrell-Ash ICAP-575 Mark II spectrophotometer. Photoluminescence measurements were performed on a FluoroLog 3 spectrofluorometer (Horiba). Ir L_{III}-edge and Rh K-edge XAFS spectra were recorded using a fluorescence-yield collection technique at the beam line 01B1 station with an attached Si (311) monochromator at SPring-8, JASRI, Harima, Japan (prop. No. 2012A1061 and 2012B1058). The EXAFS data were normalized by fitting the background absorption coefficient, around the energy region higher than that of the edge of approximately 35-50 eV, with smooth absorption of an isolated atom. The EXAFS data were examined using the Rigaku EXAFS analysis program. FT of k^3-weighted normalized EXAFS data was performed over the $3.5\ \text{Å} < k/\text{Å}^{-1} < 11\ \text{Å}$ range to obtain the radial structure function.

6.2.8 Photocatalytic H_2 Production

Powdered Ir-Rh/$K_4Nb_6O_{17}$ catalyst (50 mg), 10 ml of 90% H_2O-acetonitrile solution, and triethylamine (TEA, 0.6 mL) were introduced into a reaction vessel (30 ml), which was then sealed with a rubber septum. The resulting mixture was bubbled with Ar for 20 min in the dark. Subsequently, the sample was irradiated from the side using a Xe lamp (500 W; San-Ei Electric Co. Ltd. XEF-501S) through a glass filter ($\lambda \geq 420$ nm) with magnetic stirring at ambient pressure and temperature. The reaction progress was monitored using a Shimadzu GC-14B gas chromatograph equipped with a MS 5A column.

6.3 Results and Discussion

6.3.1 Characterization of $[Ir(ppy)_2(bpy)]^+$ and $[Rh(bpy)_3]^{3+}$-intercalated $K_4Nb_6O_{17}$

$[Ir(ppy)_2(bpy)]^+$ and $[Rh(bpy)_3]^{3+}$-intercalated $K_4Nb_6O_{17}$ was obtained by stirring a suspension of $K_4Nb_6O_{17}$ in 9 : 1 H_2O : acetonitrile solution containing both the Ir and Rh complexes for 4 days at 343 K. As a result, several samples with different molar ratios (Ir + Rh = 1.5 wt%, Ir : Rh = 1 : 0, 10 : 1, 4 : 1, 2 : 1, 1 : 1, 1 : 2, and 0 : 1) were obtained. The Ir and Rh contents were measured by ICP analysis.

Fig. 2 shows the X-ray diffraction (XRD) patterns of $K_4Nb_6O_{17}$ and the Ir-Rh/$K_4Nb_6O_{17}$ samples. The main peaks originated from (020) at 4.6º and (040) at 9.4º, and the interlayer space was calculated to be ca. 9.5 Å. Although $[Ir(ppy)_2(bpy)]^+$ and $[Rh(bpy)_3]^{3+}$ were intercalated within the interlayer space, no appreciable changes in the interlayer distance and crystal structure were observed. The Brunauer-Emmett-Teller surface area (S_{BET}) and pore volume (V_p) calculated from N_2 adsorption-desorption were, 0.62 $m^2 \cdot g^{-1}$ and 0.006 $cm^3 \cdot g^{-1}$ for pure $K_4Nb_6O_{17}$, and 2.85 $m^2 \cdot g^{-1}$ and 0.028 $cm^3 \cdot g^{-1}$ for the Ir-Rh/ $K_4Nb_6O_{17}$, respectively. The slight increase in S_{BET} could be explained by exfoliation of the layer during the intercalation procedure.

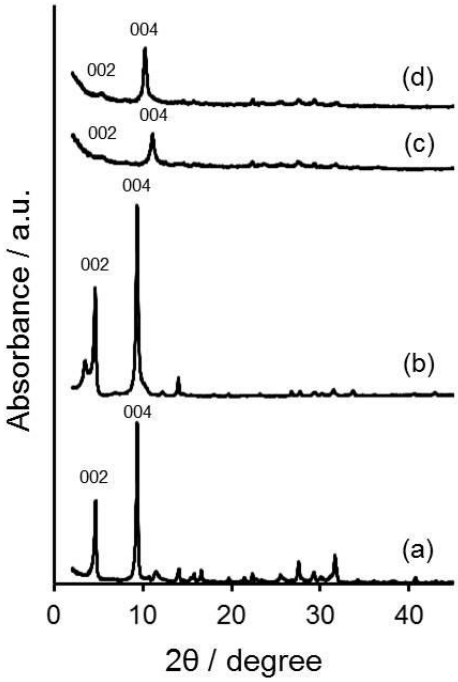

Figure 2. X-ray diffraction (XRD) patterns of (a) $K_4Nb_6O_{17}$ (b) Ir-Rh/$K_4Nb_6O_{17}$ (Ir : Rh = 1 : 1), (c) $K_4Nb_6O_{17}$ nanosheet, and (d) Ir-Rh/$K_4Nb_6O_{17}$ nanosheet (Ir : Rh = 1 : 1).

X-ray absorption measurements were conducted to elucidate the electronic structure and chemical environment of the exchanged metal complexes. **Fig. 3A** shows normalized X-ray absorption near edge structure (XANES) spectra at the Ir L_{III}-edge of $[Ir(ppy)_2(bpy)]^+$, Ir-Rh/$K_4Nb_6O_{17}$ (Ir : Rh = 1 : 1, Ir + Rh = 1.5 wt%). The white line at approximately 11,223 eV assigned to the allowed 2p → nd transition is intensified by an increase in the *d*-band vacancies as a result of oxidation [23, 38]. Thus, the white line absorption peaks of oxidized Ir species are more intense than those of reduced species. The intensity of the intercalated Ir complex was almost the same as for the free complex. In the fourier transforms (FT) of the Ir L_{III}-edge extended X-ray absorption fine structure (EXAFS) spectra (**Fig. 3B**), a strong peak was observed at 1.66 Å, which was attributed to the Ir-N and Ir-C bond, in addition to a small second shell at ca. 2.61 Å, which was assigned to neighboring carbon atoms. This verified a tridentate binding structure for an Ir(III) center in octahedral coordination. The Ir-N and Ir-C bonds and small second shells were almost same even after the immobilization on the layered $K_4Nb_6O_{17}$. We postulate that these distances were not influenced by steric constraints within the restrictive interlayer spaces as compared with the free complex.

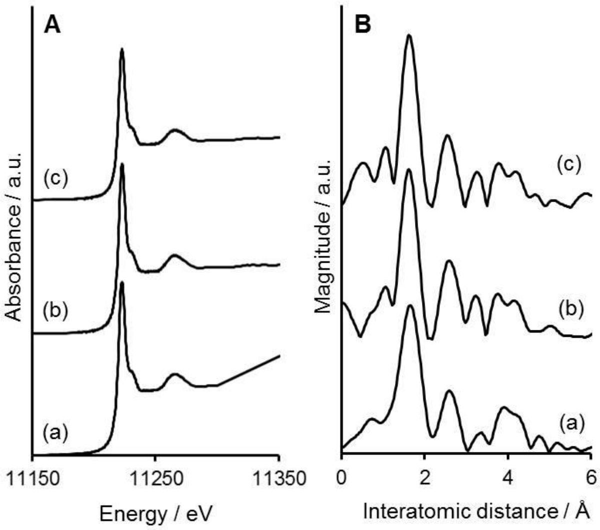

Figure 3. (**A**) Ir L_{III}-edge X-ray absorption near edge structure (XANES) spectra and (**B**) fourier transform X-ray extended absorption fine structure (FT-EXAFS) spectra of (a) $[Ir(ppy)_2(bpy)]^+$, (b) Ir-Rh/$K_4Nb_6O_{17}$ (Ir : Rh = 1 : 1), and (c) recovered Ir-Rh/$K_4Nb_6O_{17}$ (Ir : Rh = 1 : 1).

Fig. 4 shows XANES and FT-EXAFS spectra at the Rh K-edge of $[Rh(bpy)_3]^{3+}$ and Ir-Rh/$K_4Nb_6O_{17}$ (Ir : Rh = 1 : 1). The shape of the XANES spectrum of the intercalated Rh complex was almost the same as that of the free complex. For all the materials, the FT-EXAFS spectra showed a strong peak at approximately 1.60 Å, which was attributed to a Rh-N bond, and a small second shell at ~2.48 Å, which was assigned to neighboring carbon atoms, which together confirmed a bidentate binding structure in the Rh(II) oxidation state. In comparison with the $[Rh(bpy)_3]^{3+}$, the first peak of Ir-Rh/$K_4Nb_6O_{17}$ was slightly shifted toward smaller interatomic distances. Altogether, the EXAFS data reveal that the exchanged metal complexes within the layered $K_4Nb_6O_{17}$ did not cause any significant shrinking or distortion.

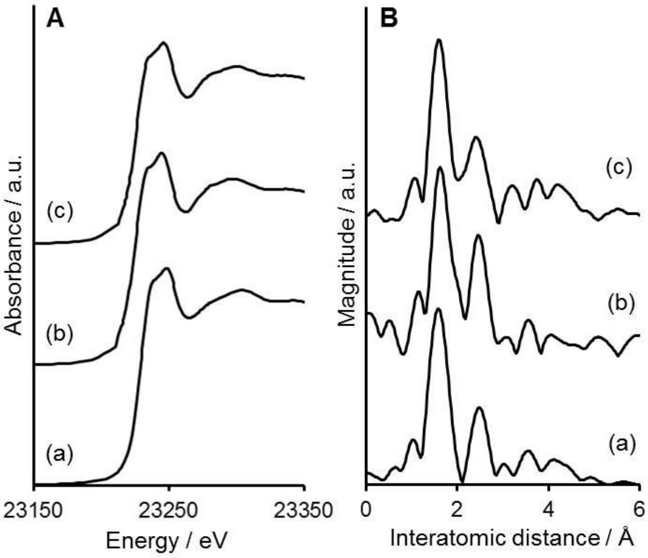

Figure 4. (**A**) Rh K-edge X-ray absorption near edge structure (XANES) spectra and (**B**) fourier transform extended X-ray absorption fine structure (FT-EXAFS) spectra of (a) $[Rh(bpy)_3]_3^+$, (b) Ir-Rh/$K_4Nb_6O_{17}$ (Ir : Rh = 1 : 1), and (c) recovered Ir-Rh/$K_4Nb_6O_{17}$ (Ir : Rh = 1 : 1).

As shown in the inset of **Fig. 5**, the UV-vis spectrum of $[Ir(ppy)_2(bpy)]^+$ in acetonitrile solution exhibits intense absorption band in the high-energy region ($\lambda < 300$ nm), which is ascribed to the spin-allowed singlet ligand-centered transition for ppy and bpy ligands (^{1}LC, π-π*); moderate low-energy band spreading from 350 to 400 nm which is ascribed to the spin-allowed singlet MLCT transition; weaker absorption tail ranging to 500 nm which is attributed to a mixture of spin-forbidden ^{3}LC and ^{3}MLCT transitions [39]. The spectrum of $[Rh(bpy)_3]^{3+}$ in acetonitrile exhibited absorption ascribed to ^{1}LC transition for bpy ligands at approximately 300 nm, while no absorption was observed in the visible region. The spectrum of Ir-Rh/$K_4Nb_6O_{17}$ (Ir : Rh = 1 : 1) exhibited absorption ascribed to free Ir and Rh complexes, suggesting that both complexes can easily diffuse within the layered $K_4Nb_6O_{17}$. The absorption intensity in the visible region ($\lambda > 400$ nm) increased with Ir complex concentration (data not shown).

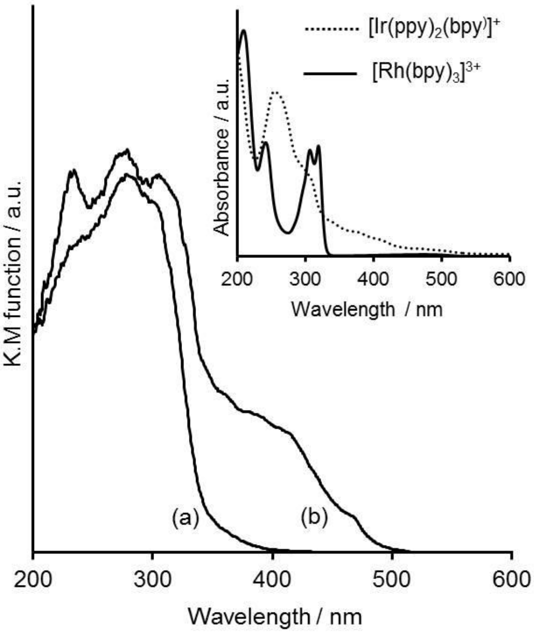

Figure 5. UV-vis spectra of (a) $K_4Nb_6O_{17}$ and (b) Ir-Rh/$K_4Nb_6O_{17}$ (Ir : Rh = 1 : 1). Inset shows the UV-vis spectra of $[Ir(ppy)_2(bpy)]^+$ and $[Rh(bpy)_3]^{3+}$ in acetonitrile.

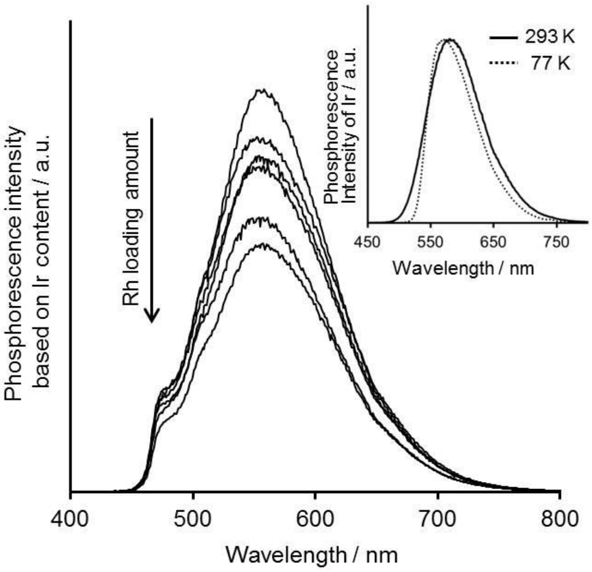

Figure 6. Photoluminescence spectra of Ir-Rh/$K_4Nb_6O_{17}$ with different Ir/Rh molar ratios at room temperature (λ_{ex} = 370 nm). Inset shows the photoluminescence spectra of $[Ir(ppy)_2(bpy)]^+$ in acetonitrile at room temperature and 77 K (λ_{ex} = 370 nm).

Emission spectra depend on ligand field strength, redox properties of the metal and ligands, and the intrinsic properties of the ligands [40]. Therefore, a slight change in the environment of the Ir complex significantly influences the orbital energy of the excited state. The inset of **Fig. 6** shows the photoluminescence spectra of $[Ir(ppy)_2(bpy)]^+$ in acetonitrile at room temperature (solid line) and 77 K (dotted line) with 370 nm excitation. $[Ir(ppy)_2(bpy)]^+$ exhibits phosphorescence emission at approximately 585 nm at room temperature, which is mainly attributable to the ^{3}MLCT transition. The maximum luminescence shifted to 570 nm at 77 K, which is principally assigned to the ^{3}LC level in a higher triplet state rather than ^{3}MLCT [41]. This significant blue shift can be explained by the efficient quenching of thermally activated deactivation processes at 77 K, therefore luminescence from ^{3}LC levels can easily occur [42]. This behavior originates from a poorly resolved vibronic structure, and it is analogous to the behavior of Pt(II) polypyridyl complexes [37].

The tendency is different for Ir-Rh/$K_4Nb_6O_{17}$, where phosphorescence emission at 550 nm showed a blue shift compared with the free complex for acetonitrile solutions at room temperature (**Fig. 6**). No significant emission due to $[Rh(bpy)_3]^{3+}$ was observed in this range. It is likely that the vibrational relaxation of the triplet MLCT excited states within the Ir-Rh/$K_4Nb_6O_{17}$ was inhibited by the limited space within the layers. Thus, phosphorescence emission from higher ^{3}LC states mainly occur to receive substantial contribution from close lying ^{3}MLCT levels, resulting in a blue shift of the emission spectra. This can be explained by "rigidochromism," a term coined by Wrighton and Morse to explain the shifts in luminescence with confinement in rigid media as compared with fluid ones [43]. Similar phenomena have been reported for $[Ir(ppy)_2(bpy)]^+$ intercalated in layered silicate materials [44]. The luminescence intensity of Ir/$K_4Nb_6O_{17}$ was weaker than that of ZrP immobilized same Ir contents, therefore suggesting host-guest interaction to electron transfer from Ir to $K_4Nb_6O_{17}$. Moreover it is notable that the peak intensity is greatest for Ir/$K_4Nb_6O_{17}$ with no Rh complex and decreases significantly with increase in Rh loading. This suggests that the Ir and Rh complexes lie close together within the layered matrix. This is advantageous for effective electron transfer in $K_4Nb_6O_{17}$ thanks to cooperative action with proximal complexes and through layered niobate. Therefore the excited state of Ir complex can be oxidatively quenched by the Rh complex according to eq. 1 [16].

$$[Ir(ppy)_2(bpy)]^0 + [Rh(bpy)_3]^{3+} \rightarrow [Ir(ppy)_2(bpy)]^+ + [Rh(bpy)_3]^{2+} \quad (1)$$

6.3.2 Photocatalytic H_2 Production of $[Ir(ppy)_2(bpy)]^+$ and $[Rh(bpy)_3]^{3+}$-intercalated $K_4Nb_6O_{17}$

The photocatalytic activity of Ir-Rh/$K_4Nb_6O_{17}$ for H_2 production was evaluated by visible light irradiation ($\lambda \geq 420$ nm) in a 90% H_2O-acetonitrile solution containing various SRs. **Fig. 7** shows the timeline of H_2 production for the different SRs. No reaction was observed under dark conditions in the presence of the photocatalyst or without a SR with irradiation. Moreover, there was no significant H_2 production for $K_4Nb_6O_{17}$ without metal complexes under the identical reaction conditions. It confirmed that this heterogeneous catalyst generated more hydrogen than homogeneous one due to condensation effect induced frequent electron transfer. The type of SR significantly affected photocatalytic activity depending on the dielectric constant and viscosity of the reaction medium. Among the investigated SRs, TEA was found to be the most effective. The use of TEOA and EDTA instead of TEA resulted in slight activity, and the use of MeOH, EtOH, HCOOH, and CH_3COOH resulted in no activity. These results suggest that H_2 production with TEA was more effective because of high electron donation and the large gap of the oxidation potential toward Ir complex. The kind of SRs has an even greater influence in the present Ir-Rh system than in the

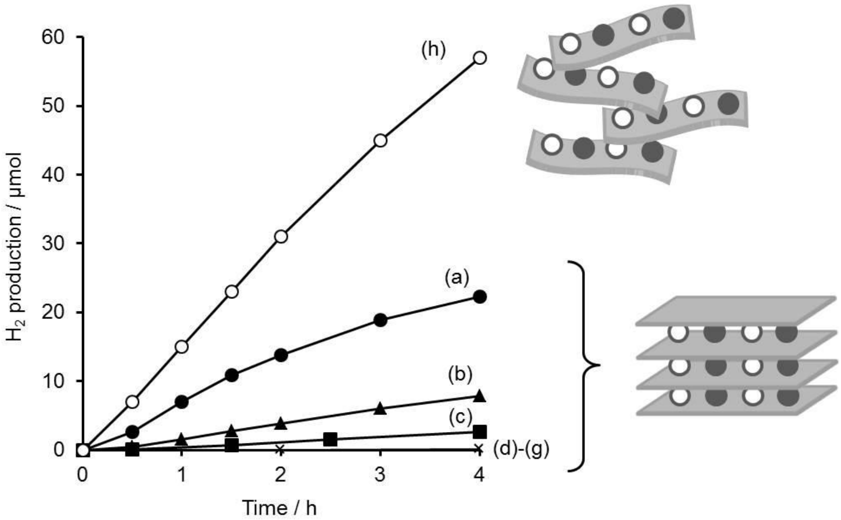

Figure 7. Photocatalytic H_2 production in 10% MeCN-H_2O solution with various 0.6 M electron donors: (a) TEA, (b) TEOA, (c) EDTA, (d) MeOH, (e) EtOH, (f) HCOOH, (g) CH_3COOH using Ir-Rh/$K_4Nb_6O_{17}$ (Ir : Rh = 1 : 1), and (h) TEA using Ir-Rh/$K_4Nb_6O_{17}$ nanosheet (Ir : Rh = 1 : 1) under visible light irradiation ($\lambda \geq$ 420nm).

traditional Ru-based system because the Ir-Rh system contains a reductive quenching step of the excited-state Ir complex PS by the SR, as will be discussed later. A contrary study reports that the quenching constant of $[Ir(ppy)_2(bpy)]^+$ for TEA ($k_q = 1.2 \times 10^8$ $M^{-1}s^{-1}$) is larger than for TEOA ($k_q = 5.4 \times 10^6$ $M^{-1}s^{-1}$) using laser flush photolysis [16].

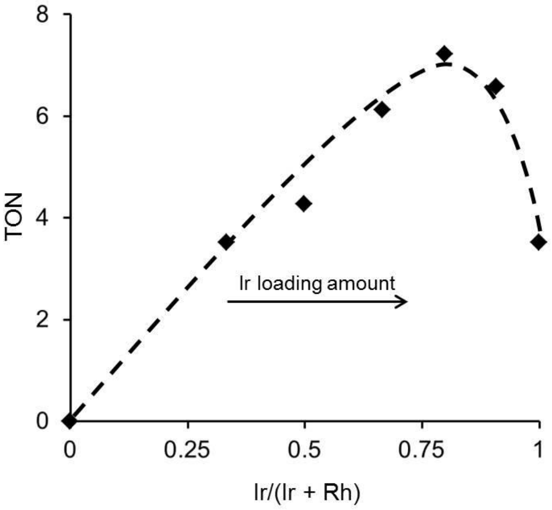

Figure 8. Effect of Ir and Rh molar ratio in Ir-Rh/$K_4Nb_6O_{17}$ on photocatalytic H_2 production ($\lambda_{ex} > 420$ nm).

The influence of molar ratio of PS Ir complex to proton reduction catalyst Rh complex was also explored with different metal loading ratios (Ir : Rh = 1 : 0, 10 : 1, 4 : 1, 2 : 1, 1 : 1, 1 : 2, and 0 : 1) (**Fig. 8)**. It was possible to control the intercalated metal loading ratio within $K_4Nb_6O_{17}$ by changing the initial concentration ratio of metal complexes in the slurry. Almost no reaction occurred in the presence of only Rh complex, while H_2 formation proceeded in the presence of only Ir complex. This suggests that an exited electron transfers from the Ir complex to $K_4Nb_6O_{17}$ and proton reduction is generated on the $K_4Nb_6O_{17}$. Increase in Ir loading ratio resulted in higher turnover number (TON) for H_2 formation. Maximal TON was obtained at Ir/(Ir+Rh) = 0.80, which corresponds to Ir : Rh = 4 : 1. Thus, there was a direct electron transfer from the PS Ir complex to the proton reduction catalyst Rh complex without an electron mediator. These results indicate that the electron transfer step is crucial for efficient photocatalysis.

There is some controversy as to whether H_2 production occurs on colloids dissociated from the complex or on the molecular complex itself [45, 46]. In our preliminary experiment, the X-ray absorption fine structure (XAFS) spectrum of the Ir-Rh/$K_4Nb_6O_{17}$ recovered after the photocatalytic reaction was identical to that of the fresh catalyst **(Fig. 3, 4)**, indicating no changes in the electronic configuration and local structures. Moreover, the recovered Ir-Rh/$K_4Nb_6O_{17}$ retained its original photocatalytic activity in a reuse test, as shown in **Fig. 9**. This suggests that molecular species stayed intact; this is strong evidence that molecular species rather than colloidal ones are responsible for catalysis.

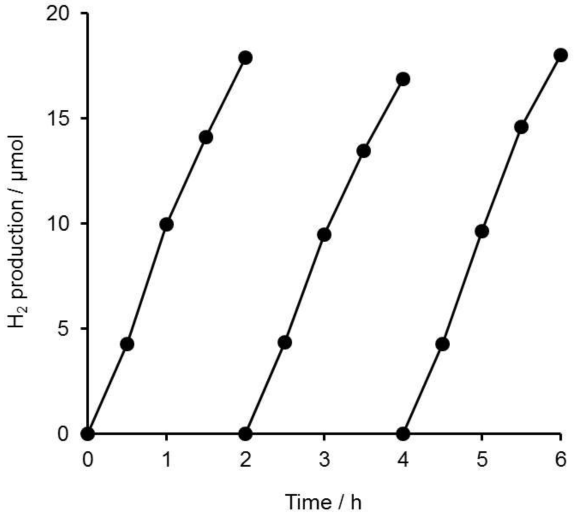

Figure 9. Reuse experiment using Ir-Rh/$K_4Nb_6O_{17}$ (Ir : Rh = 1 : 1) for photocatalytic H_2 production under visible light irradiation ($\lambda \geq 420$nm).

In order to achieve enhanced photocatalytic activity, an exfoliated $K_4Nb_6O_{17}$ nanosheet was also prepared from as-synthesized $K_4Nb_6O_{17}$ by exfoliation with tetrabutylammonium hydroxide [36]. The textural properties of the $K_4Nb_6O_{17}$ nanosheet are summarized in **Table 1**. S_{BET} for the $K_4Nb_6O_{17}$ nanosheet and the Ir-Rh/$K_4Nb_6O_{17}$ nanosheet were 2.85 and 37.8 m^2g^{-1}, respectively, which were 10-100 times larger than that of the original $K_4Nb_6O_{17}$ because of the exfoliation of the nanosheet aggregate. The layered structure of $K_4Nb_6O_{17}$ is believed to be preserved during exfoliation, as manifested by the (020) and (040) basal reflections. The interlayer spacing (040) of the exfoliated $K_4Nb_6O_{17}$ with and without metal complexes are approximately 8.6 and 8.0 Å respectively. As expected, H_2 production activity on the exfoliated $K_4Nb_6O_{17}$ nanosheet is enhanced 2.5 times because of increased surface area. The diffusion of protons within the interlayer of $K_4Nb_6O_{17}$ may also affect photoreduction rates, and the metal complexes exposed on the surface of the exfoliated $K_4Nb_6O_{17}$ nanosheet may enhance the diffusion of protons and provide easy access to the $[Rh(bpy)_3]^{3+}$ proton reduction complex.

Table 1. Textural properties of $K_4Nb_6O_{17}$ and metal loaded samples.

sample	S_{BET} /$m^2 \cdot g^{-1}$	V_p /$cm^3\ g^{-1}$
$K_4Nb_6O_{17}$	0.62	0.006
Ir-Rh/$K_4Nb_6O_{17}$	2.85	0.028
$K_4Nb_6O_{17}$ nanosheet	61.3	0.21
Ir-Rh/$K_4Nb_6O_{17}$ nanosheet	37.8	0.16

As mentioned earlier, the classical molecule-based photocatalytic H_2 production system consists of multicomponents, including PS ($Ru(bpy)_3^{2+}$), ER (MV^{2+}), WRC (colloidal Pt), and a SR, in which an ER oxidatively quenches PS* allowing electron transfer to a WRC. It is remarkable that the photocatalyst in this study enabled visible light photosensitization of the Ir complex and reduction of H^+ by the Rh complex to produce H_2 without any ER, as can be described by the following eqs [16].

$$[Ir(ppy)_2(bpy)]^+ + h\nu \rightarrow [Ir(ppy)_2(bpy)]^{+*} \quad (2)$$

$$[Ir(ppy)_2(bpy)]^{+*} + TEA \rightarrow [Ir(ppy)_2(bpy)]^0 + TEA^+ \quad (3)$$

$$2[Ir(ppy)_2(bpy)]^0 + [Rh(bpy)_3]^{3+} \rightarrow 2[Ir(ppy)_2(bpy)]^+ + [Rh(bpy)_3]^+ \quad (4)$$

$$[Rh(bpy)_3]^+ + 2H^+ \rightarrow [Rh(bpy)_3]^{3+} + H_2 \quad (5)$$

Initially, the excited state of the $[Ir(ppy)_2(bpy)]^{+*}$ (eq. 2) is reductively quenched by TEA (SR) to produce $[Ir(ppy)_2(bpy)]^0$ in eq. 3. Subsequently, the activated reduced Ir^0 species directly delivers reducing equivalents to the Rh WRC according to eq. 4, which finally produces H_2 through reductive elimination from the Rh dihydride species in a homolytic unimolecular pathway (eq. 5). Although the oxidation state of the active WRC is ambiguous, $[Rh(bpy)_2]^+$ generated by two consecutive reductions by the activated reduced Ir species and the labilization of the bpy ligand is postulated as one of the possible active species [47]. It is important to note that the first reductive quenching step is different from $[Ru(bpy)_3]^{2+}$ system, which undergoes oxidative quenching by the ER to generate $[Ru(bpy)_3]^{3+}$. In the present photocatalytic system, maximal TON was obtained in the presence of Ir : Rh = 4 : 1 in spite of stoichiometry fomula was 2 : 1. It is presumed that half of exited

$[Ir(ppy)_2(bpy)]^0$ species are consumed as phosphorescence or electron injection to $K_4Nb_6O_{17}$. A necessary of Ir PS excess amount suggests the aforementioned mechanism of two consecutive reductions of high oxidative Rh species by reduced Ir species.

6.4 Conclusion

In summary, the intercalation of PS iridium(III) and proton reduction catalyst rhodium(III) complexes within layered $K_4Nb_6O_{17}$ was a successful new type of photocatalyst with unique photoluminescence and photocatalytic activities. Photoluminescence emission deriving from the Ir complex of the Ir-Rh/$K_4Nb_6O_{17}$ was significantly blue shifted compared with that of the free complex in acetonitrile at room temperature owing to the rigidchromism effect. The excited state of the Ir complex within the layered $K_4Nb_6O_{17}$ underwent efficient oxidative quenching by the Rh complex in close proximity; therefore, the emission intensity decreased with increasing Rh loading. The Ir-Rh/$K_4Nb_6O_{17}$ catalyst was a recyclable heterogeneous photocatalyst for H_2 evolution in aqueous solution, where direct electron transfer from Ir to Rh occurred without electron mediator. The use of exfoliated $K_4Nb_6O_{17}$ nanosheets exhibited enhanced photocatalytic activities presumably because of the increased accessibility for protons.

6.5 References

[1] M. Graetzel, *Acc. Chem. Res.*, **1981**, 14, 376.

[2] N. S. Lewis, D. G. Nocera, *Proc. Natl. Acad. of Sci.*, **2006**, 103, 15729.

[3] A. J. Esswein, D. G. Nocera, *Chem. Rev.*, **2007**, 107, 4022.

[4] A. Fujishima, K. Honda, *Nature*, **1972**, 238, 37.

[5] M. Gratzel, *Nature*, **2001**, 414, 338.

[6] H. Arakawa, K. Sayama, *Catal. Surv. Jap.*, **2000**, 4, 75.

[7] K. Maeda, K. Domen, *J. Phys. Chem. C*, **2007**, 111, 7851.

[8] A. Kudo, Y. Miseki, *Chem. Soc. Rev.*, **2009**, 38, 253.

[9] L. L. Tinker, N. D. McDaniel, S. Bernhard, *J. Mater. Chem.*, **2009**, 19, 3328.

[10] M. Wang, Y. Na, M. Gorlov, L. Sun, *Dalton Trans.*, **2009**, 6458.

[11] P. D. Tran, V. Artero, M. Fontecave, *Energy Environ. Sci.*, **2010**, 3, 727.

[12] H. Ozawa, K. Sakai, *Chem. Commun.*, **2011**, 47, 2227.

[13] A. Moradpour, E. Amouyal, P. Keller, H. Kagan, *Nouv. J. Chim.*, **1978**, 2, 547.

[14] H. Ozawa, M.-a. Haga, K. Sakai, *J. Am. Chem. Soc.*, **2006**, 128, 4926.

[15] L. L. Tinker, N. D. McDaniel, P. N. Curtin, C. K. Smith, M. J. Ireland, S. Bernhard, *Chem. Eur. J.*, **2007**, 13, 8726.

[16] E. D. Cline, S. E. Adamson, S. Bernhard, *Inorg. Chem.*, **2008**, 47, 10378.

[17] Y.-J. Yuan, J.-Y. Zhang, Z.-T. Yu, J.-Y. Feng, W.-J. Luo, J.-H. Ye, Z.-G. Zou, *Inorg. Chem.*, **2012**, 51, 4123.

[18] W. J. Roth, J. Cejka, *Catal. Sci. Technol.*, **2011**, 1, 43.

[19] Y. Tao, H. Kanoh, L. Abrams, K. Kaneko, *Chem. Rev.*, **2006**, 106, 896.

[20] K. Mori, K. Kagohara, H. Yamashita, *J. Phys. Chem. C*, **2008**, 112, 2593.

[21] K. Mori, M. Kawashima, K. Kagohara, H. Yamashita, *J. Phys. Chem. C*, **2008**, 112, 19449.

[22] K. Mori, M. Kawashima, M. Che, H. Yamashita, *Angew. Chem. Inter. Ed.*, **2010**, 49, 8598.

[23] K. Mori, M. Tottori, K. Watanabe, M. Che, H. Yamashita, *J. Phys. Chem. C*, **2011**, 115, 21358.

[24] K. Mori, K. Watanabe, K. Fuku, H. Yamashita, *Chem. Eur. J.*, **2012**, 18, 415.

[25] K. Mori, K. Watanabe, Y. Terai, Y. Fujiwara, H. Yamashita, *Chem. Eur. J.*, **2012**, 18, 11371.

[26] K. Mori, S. Ogawa, M. Martis, H. Yamashita, *J. Phys. Chem. C*, **2012**, 116, 18873.

[27] M. Gasperin, M.-T. le Bihan, *J. Solid State Chem.*, **1980**, 33, 83.

[28] T. Nakato, H. Edakubo, T. Shimomura, *Micropor. Mesopor. Mater.*, **2009**, 123, 280.

[29] J. Ma, J. Wu, J. Zheng, L. Liu, D. Zhang, X. Xu, X. Yang, Z. Tong, *Micropor. Mesopor. Mater.*, **2012**, 151, 325.

[30] T. Nakato, K. Kusunoki, K. Yoshizawa, K. Kuroda, M. Kaneko, *J. Phys. Chem.*, **1995**, 99, 17896.

[31] C. Ulbricht, B. Beyer, C. Friebe, A. Winter, U. S. Schubert, *Adv. Mater.*, **2009**, 21, 4418.

[32] N. Sutin, C. Creutz, E. Fujita, *Comments Inorg. Chem.*, **1997**, 19, 67.

[33] M. S. Lowry, J. I. Goldsmith, J. D. Slinker, R. Rohl, R. A. Pascal, G. G. Malliaras, S. Bernhard, *Chem. Mater.*, **2005**, 17, 5712.

[34] J. E. Hillis, M. K. DeArmond, *J. Luminescence*, **1971**, 4, 273.

[35] K. Nassau, J. W. Shiever, J. L. Bernstein, *J. Electrochem. Soc.*, **1969**, 116, 348.

[36] A. Takagaki, M. Sugisawa, D. Lu, J. N. Kondo, M. Hara, K. Domen, S. Hayashi, *J. Am. Chem. Soc.*, **2003**, 125, 5479.

[37] K. Wang, M.-a. Haga, H. Monjushiro, M. Akiba, Y. Sasaki, *Inorg. Chem.*, **2000**, 39, 4022.

[38] P. I. Ravikovitch, A. V. Neimark, *Langmuir*, **2000**, 16, 2419.

[39] M. G. Colombo, A. Hauser, H. U. Guedel, *Inorg. Chem.*, **1993**, 32, 3088.

[40] S. I. Gorelsky, E. S. Dodsworth, A. B. P. Lever, A. A. Vlcek, *Coord. Chem. Rev.*, **1998**, 174, 469.

[41] S.-H. Wu, J.-W. Ling, S.-H. Lai, M.-J. Huang, C. H. Cheng, I. C. Chen, *J. Phys. Chem. A*, **2010**, 114, 10339.

[42] Y. Ohsawa, S. Sprouse, K. A. King, M. K. DeArmond, K. W. Hanck, R. J. Watts, *J. Phys. Chem.*, **1987**, 91, 1047.

[43] M. Wrighton, D. L. Morse, *J. Am. Chem. Soc.*, **1974**, 96, 998.

[44] D. Mochizuki, M. Sugiyama, M. M. Maitani, Y. Wada, *Eur. J. Inorg. Chem.*, **2013**, 2324.

[45] P. Lei, M. Hedlund, R. Lomoth, H. Rensmo, O. Johansson, L. Hammarström, *J. Am. Chem. Soc.*, **2007**, 130, 26.

[46] K. Yamauchi, S. Masaoka, K. Sakai, *J. Am. Chem. Soc.*, **2009**, 131, 8404.

[47] M. Kirch, J.-M. Lehn, J.-P. Sauvage, *Helv. Chim. Acta*, **1979**, 62, 1345.

Chapter VII

General Conclusion

This thesis deals with the designs of visible light driven metal complex photocatalysts supported on high regularity metal oxides and their applications to chemical reactions such as selective oxidation, hydrogen production and C-C cross coupling. These achievements contribute to the advancement of photo-chemistry with metal complexes, the improvement of organic synthesis process and the solution of energy problems depending on fossil fuel.

In the experiments described in Chapter II, photocatalysts containing $Ru(bpy)_3^{2+}$ complexes encapsulated zeolite Y cages were investigated from various extra framework alkali metal cations (Li^+, Na^+, K^+, Rb^+, and Cs^+). $Ru(bpy)_3^{2+}$ complexes in zeolite Y supercages have been introduced via a “ship-in-a-bottle” method in **Fig. 1a**. The effects of the alkali metal cations on the spectroscopic properties and photoinduced oxidation abilities of $Ru(bpy)_3^{2+}$ complexes in host-guest interaction were investigated. Changing to lighter alkali metal cations from Cs^+ to Li^+ leads to the enhancement of the photocatalytic activity for oxidation of styrene derivatives using molecular oxygen with the assist of increasing phosphorescence emission (**Fig. 1b**). It suggests that the presence of lighter alkali metal cations improves the excited ^{3}MLCT state, lifetime and quantum yield of $Ru(bpy)_3^{2+}$ complexes within the restricted pore spaces. These results are interpreted in the proportional relation between phosphorescence emission and photo-assisted catalytic activity.

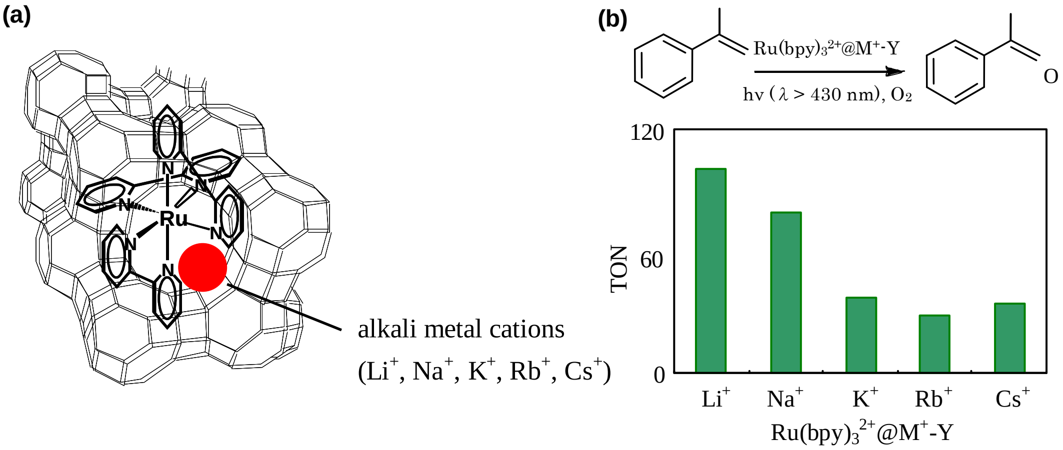

Figure 1. (a) Illustration and (b) photoinduced oxidation of α-methyl styrene about $Ru(bpy)_3$ complex encapsulated within alkali metal cations exchanged zeolite Y.

In Chapter III, a new type of nano-sized photocatalyst assisted electromagnetic field of LSPR with chromophore $Ru(bpy)_3^{2+}$ complex was proposed. This plasmonic photocatalyst is composed of size controlled silver or gold nanoparticle as core, silica coat by sol-gel method at shell, and $Ru(bpy)_3^{2+}$ modified on surface of silica layer as shown **Fig. 2a, b**. The reinforcement electric field enhanced on the vicinity of the Ag NPs due to the LSPR significantly improves the efficiencies of absorbance and luminescence of the dye, which ultimately results in the increase of energy and/or electron transfer to molecular oxygen and catalytic activity for the photooxidation of styrene derivatives in **Fig. 2c**. The silica layer plays the important roles in a protection of metal NPs, a spacer to keep the distance between NPs and catalyst, and insulation of dielectric metal sphere. This technique provides a possibility to the creation of novel catalysts enabling selective organic reactions even under limited light source.

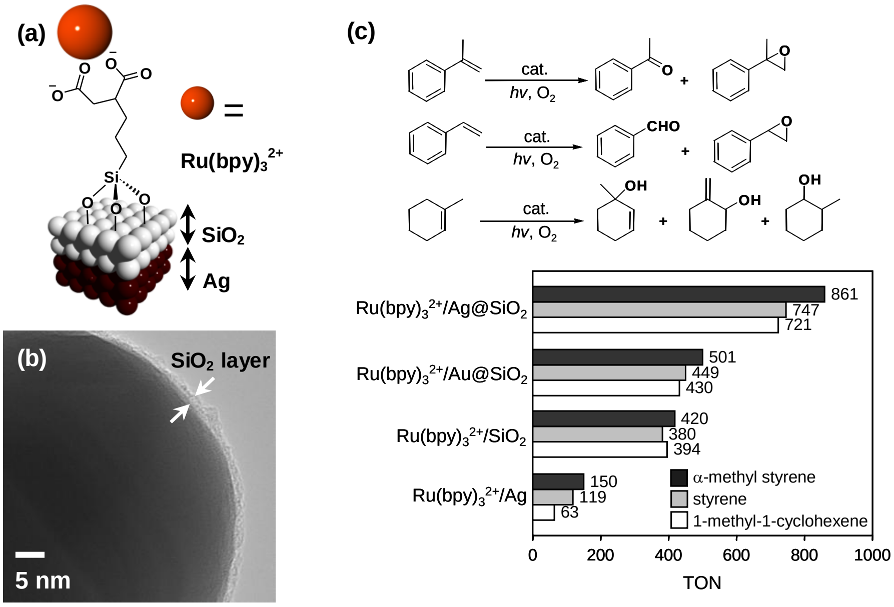

Figure 2. (a) Illustration of surface structure, (b) HR-TEM image and (c) photocatalytic oxidations of $Ru(bpy)_3^{2+}$ anchored on silica coating Ag nanoparticle.

In Chapter IV, photo-assisted Suzuki-Miyauira coupling reaction has been realized by molecule Pd(II) complex containing Ru(II)-polypyridyl derivative as a visible light photosensitizing unit as shown **Fig. 3a**. It is expected that an electron transfer from excited Ru species to Pd(0) may facilitate the formation of active electron rich Pd(0) and oxidative addition step with aryl halides. Catalytic activity induced visible-light was enhanced compared to coupling reactions under no light or physical mixture of each mononuclear complex, which originates quenching phosphorescence emission from Ru to Pd formed binuclear complex in **Fig. 3b**. In this Chapter, we realized for the first time the application to Suzuki-Miyaura coupling reaction utilizing bimetallic complex combined photosensitized and catalytic site under ambient condition.

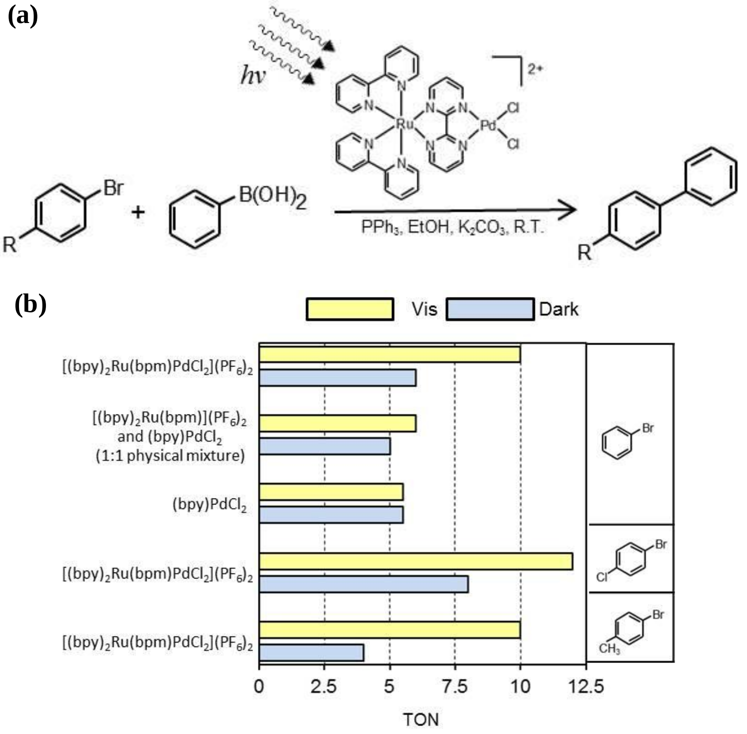

Figure 3. (a) Experiment condition and (b) results in the comparable conditions, with photocatalytic Suzuki-Miyaura coupling reaction by [(bpy)$_2$Ru(bpm)PdCl$_2$](PF$_6$)$_2$.

In Chapter V, the hybrid of photosensitizer [Ir(ppy)$_2$(bpy)]$^+$ and proton reduction catalyst [Rh(bpy)$_3$]$^{3+}$ complexes within an interlayer space of expanded ZrP was proposed a new concept of photocatalyst with photoluminescence properties as well as photocatalytic activities in **Fig. 4a-c**. Photoluminescence emission due to the Ir complex of the Ir-Rh/ZrP was blue shifted relative to that of the free complex in homogeneous by the rigidchromism effect. The lowest ^{3}MLCT of Ir complex within the microenvironments undergoes the oxidative quenching by the neighboring Rh complex, thus the phosphorescence intensity decreased with increasing the Rh loading. The Ir-Rh/ZrP photocatalyst exhibits both visible light sensitization and H$_2$ evolution in aqueous solution without electron mediator in **Fig. 4d**.

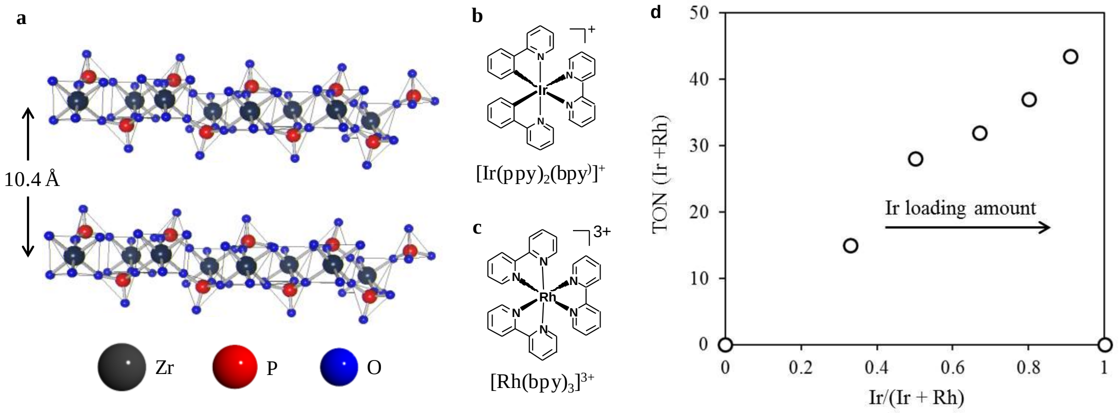

Figure 4. Schematic structure of (a) ZrP with an enlarged interlayer distance, (b) $[Ir(ppy)_2(bpy)]^+$ and (c) $[Rh(bpy)_3]^{3+}$. (d) Effect of Ir and Rh molar ratio in the Ir-Rh/ZrP for photocatalytic H_2 production (λ_{ex} > 420 nm).

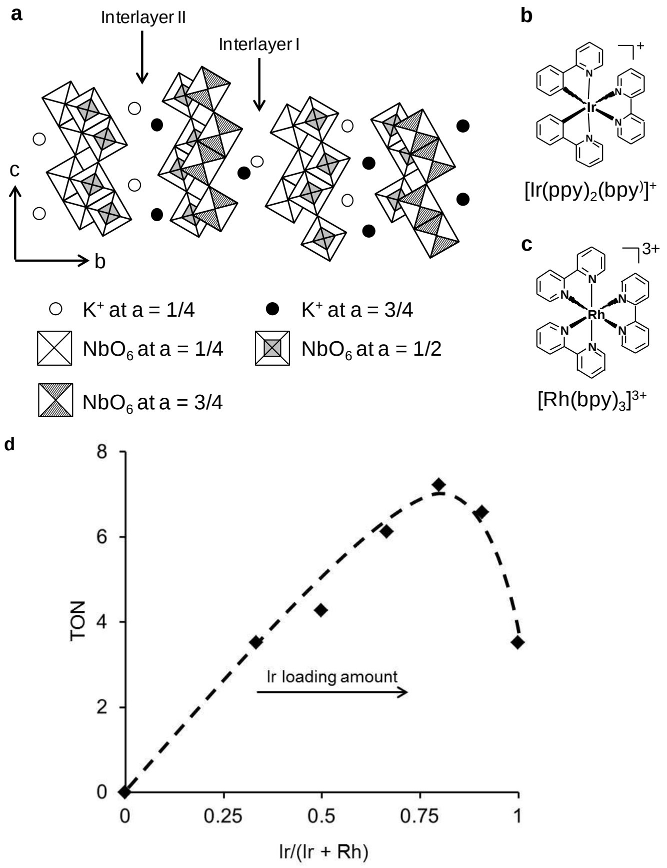

Figure 5. Schematic of (a) $K_4Nb_6O_{17}$, (b) $[Ir(ppy)_2(bpy)]^+$, and (c) $[Rh(bpy)_3]^{3+}$. (d) Effect of Ir and Rh molar ratio with Ir-Rh/$K_4Nb_6O_{17}$ in photocatalytic H_2 production (λ_{ex} > 420 nm).

In acknowledge mentioned in Chapter VI, the change of supports to $K_4Nb_6O_{17}$ was tried with the same concept to Chapter V except the point of keeping electron conductivity. The insertion of

$[Ir(ppy)_2(bpy)]^+$ and $[Rh(bpy)_3]^{3+}$ complexes into layered niobate $K_4Nb_6O_{17}$ was succeeded in the design of heterogeneous photocatalyst without an electron relay as seen **Fig. 5**. Effective direct electron transfer from Ir to Rh complex in restricted space results in a dramatically increase of hydrogen generation from the gradual quenching by the increasing Rh ratio to Ir in close proximity, and maximum activity was exhibited when the ratio of Ir : Rh is 4 : 1 as seen **Fig. 5d**. The Ir-Rh/$K_4Nb_6O_{17}$ catalyst was enabled to generate more volume H_2 in comparison to homogeneous and repeatedly evolve H_2 in aqueous solution under visible light irradiation. Support materials of these hydrogen production catalysts hold the promise of improvement to high activity with the assistance of electron conductivity.

The photo-responsive complexes ($[Ru(bpy)_3]^{2+}$, $[(bpy)_2Ru(bpm)PdCl_2]^{2+}$ and $[Ir(ppy)_2(bpy)]^+$) and proton reduction complex ($[Rh(bpy)_3]^{3+}$) were searched to unique performances such as light absorbance, photoluminescence emission, X-ray properties, and photocatalytic activity at immobilization on various nanostructured materials. The differences of heterogeneous properties for these complex photocatalysts were disappeared relative to free complex performances in homogeneous. The structures of complexes were affected by the restricted interspaces of zeolite Y, ZrP and $K_4Nb_6O_{17}$. The phosphorescence emission and electron and/or energy transfer were controlled by the effect of the heavy atom, electromagnetic field, polarity, and electron conductivity around environment. Then electron and/or energy transfer from the exited state of the dye to molecular catalyst is also facilitated with increasing the quantum yield of luminescence. We firstly found out that the catalytic activities are improved in response to its photoluminescence intensities. The author believes that the viewpoints of the relation of luminescence emission and catalytic activity contribute to develop photocatalytic techniques applied metal complexes responded to visible light.

List of Publications

[1] K. Mori, M. Kawashima, K. Kagohara, and H. Yamashita
"Influence of Exchanged Alkali Metal Cations within Zeolite Y cages on Spectroscopic and Photooxidation Properties of the Incorporated Tris(2,2'-bipyridine)ruthenium(II) Complexes"
Journal of Physical Chemistry C, **112** (2008) 19449-19455.

[2] K. Mori, M. Kawashima, M. Che, and H. Yamashita
"Enhancement of the Photoinduced Oxidation Activity of a Ruthenium(II) Complex Anchored on Silica-Coated Silver Nanoparticles by Localized Surface Plasmon Resonance"
Angewandte Chemie International Edition, **49** (2010) 8598-8601.

[3] K. Mori, M. Kawashima, and H. Yamashita
"Visible-light-Enhanced Suzuki-Miyaura Coupling Reaction by Cooperative Photocatalysis with Ru-Pd Bimetallic Complex"
Chemical Communications, in press.

[4] K. Mori, J. Aoyama, M. Kawashima, and H. Yamashita
"Visible-light Driven H_2 Production Utilizing Iridium and Rhodium Complexes Intercalated into Zirconium Phosphate Layered Matrix"
Dalton Transactions, **43** (2014) 10541-10547.

[5] M. Kawashima, K. Mori, J. Aoyama, and H. Yamashita
"Synthesis and Characterization of Ir and Rh Complexes-supported on Layered $K_4Nb_6O_{17}$ as a Heterogeneous Photocatalyst for Visible-Light-Induced Hydrogen Evolution"
Bulletin of the Chemical Society of Japan, in press.

<Related work>

[6] K. Mori, K. Watanabe, M. Kawashima, M. Che, and H. Yamashita
“Anchoring of Pt(II) Pyridyl Complex to Mesoporous Silica Materials: Enhanced Photoluminescence Emission at Room Temperature and Photooxidation Activity using Molecular Oxygen”
Journal of Physical Chemistry C, **115** (2010) 1044-1050.

Acknowledgement

The author, Masayoshi Kawashima, expresses his deepest graduate to his supervisor, Professor Hiromi Yamashita (Division of Materials and Manufacturing Science, Graduate School of Engineering, Osaka University) for his constructive guidance and encouragement throughout the present work. Sincere thanks are extended to Professor Toshihiro Tanaka (Division of Materials and Manufacturing Science, Graduate School of Engineering, Osaka University), Professor Yasufumi Fujiwara (Division of Materials and Manufacturing Science, Graduate School of Engineering, Osaka University) and Associate Professor Kohsuke Mori (Division of Materials and Manufacturing Science, Graduate School of Engineering, Osaka University) who examiner of the dissertation, for their helpful and useful suggestion.

The author deeply thanks Associate Professor Takashi Kamegawa (Department of Applied Chemistry, Graduate School of Engineering, Osaka Prefecture University), Assistant Professor Yasutaka Kuwahara (Division of Materials and Manufacturing Science, Graduate School of Engineering, Osaka University), and Technical Officer Tetsutaro Ohmichi for numerous discussion and encouragement.

The author would say gratefully to Mr. Eiji Taguchi (Research Center for Ultra-High Voltage Electron Microscopy, Osaka University) for TEM observation.

Thanks must be made to Dr. Sayoko Shironita, Dr. Yu Horiuchi, Dr. Shusuke Okada, Dr. Kojirou Fuku, Mr. Kento Kagohara, Mr. Kentaro Watanabe, Mr. Junya Aoyama, Mr. Yoshihiko Kubota, Mr. Hiroki Kakudo, Mr. haruhisa Ura, Mr. Tomoya Takasaki, Mr. Akihiro Hanafusa, and Ms. Ai Nozaki for their collaboration and lively discussion; without their devoted supports, completion of this work would not have been possible. He reaps benefits from all the students and international students studied together with him at this laboratory led by Professor Hiromi Yamashita. The author also wishes to thank his parents Nobutake Kawashima and Toshiko Kawashima, his older sister Yukiyo Fuchibe, his older brother Tomoyasu Fuchibe, his older brother Takahiro Kawashima, and his older sister Yumi Kawashima for their continuous encouragement and committed supports.

This work was financially supported by a Grant-in-Aid for Scientific Research from the Ministry of Education, Culture, Sports, Science, and Technology (MEXT), Japan, and Fujikin Soft Incorporated to tuition for doctor course of Osaka University.

Masayoshi KAWASHIMA

Osaka
June 2014